2016

Understanding Chemical Reactions In Novel Materials: From Metal Organic Frameworks to Oxyallyl Cations

Kiara Taylor-Edinbyrd
Louisiana State University and Agricultural and Mechanical College, msktaylor31@yahoo.com

UNDERSTANDING CHEMICAL REACTIONS IN NOVEL MATERIALS: FROM METAL ORGANIC FRAMEWORKS TO OXYALLYL CATIONS

A Dissertation

Submitted to the Graduate Faculty of the
Louisiana State University and
Agricultural and Mechanical College
in partial fulfillment of the
requirements for the degree of
Doctor of Philosophy

in

The Department of Chemistry

by
Kiara Taylor-Edinbyrd
B.S. Texas Southern University, 2011
December 2016

This dissertation is dedicated to my three loving children, Paris, Christian and Kali, my husband, parents and grandparents for their support and to my late brother, Germain Harris II.

ACKNOWLEDGEMENTS

I would like to acknowledge my advisor, Dr. Revati Kumar, who remained a patient and supportive mentor; my success is due in part to her unrelenting dedication.

ABSTRACT

The work of this dissertation investigates the chemical processes of novel materials through quantum mechanical calculations and molecular dynamics simulations. The first section of this work focuses on probing copper based metal organic frameworks (MOFs) for their ability to catalytically release nitric oxide from s-nitrosothiol (RSNO) precursors in a slow, controlled and sustained manner and compares these findings to a free copper ion/ethanol solution. Through the use of electronic structure calculations and molecular dynamics simulations, studies are carried out to better understand how the barriers of RSNOs approach to the catalytic copper center changes with modifications to the R-group (of the RSNO) and the organic linkers of the MOF.

In addition to the above-mentioned work, electronic structure calculations were employed to investigate the origins of regioselectivity for silylenol ether products generated from disubstituted ketones through a unimolecular nucleophilic substitution (S_{N1}) reaction mechanism. Synthesis of these materials is highly desired as a result of current chemistries lacking sufficient methods to steer the synthesis of natural product inspired molecules without the use of steric and electronic bias.

TABLE OF CONTENTS

CHAPTER 1. INTRODUCTION OF NOVEL MATERIALS

1.1 Supramolecular Chemistry and Porous Materials

Supramolecular chemistry focuses on the association of molecules, rather than atoms, as simple building blocks for larger complex supermolecules through noncovalent interactions as opposed to covalent bonds.[2] Also referred to as "chemistry beyond the molecule" by Nobel laureate Jean-Marie Lehn,[3] supramolecular chemistries are typically known for their ability to self-assemble and are ubiquitous in nature. The nature of these supermolecules relies on complexation through noncovalent interactions including electrostatic, van der Waals, hydrogen bonding, pi-stacking and hydrophobic effects as shown in Figure 1.1. An expansion of the field in the late 1960s by Cram, Lehn and Pederson led to

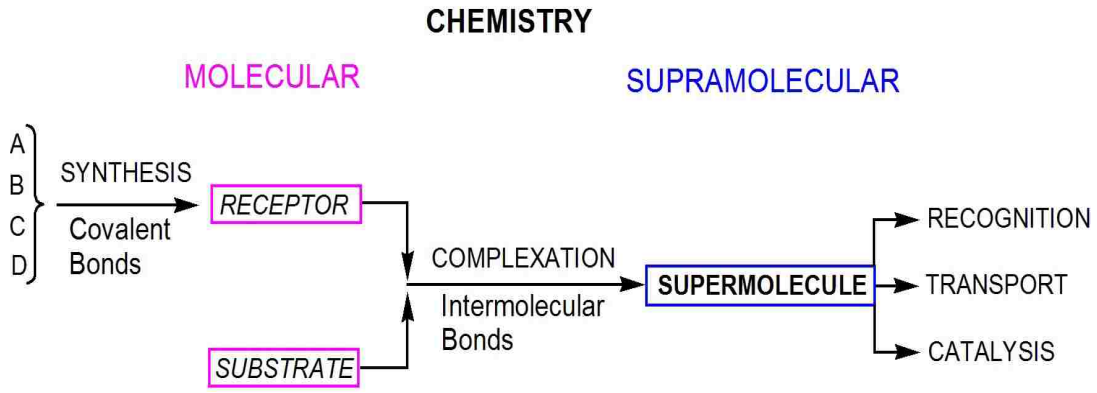

Figure 1.1. Illustrates that the building blocks of molecular and supramolecular chemistries. Covalent bonds between atoms are responsible the formation of molecules as opposed to the presence of intermolecular bonds of molecules for the formation of supramolecular structures. This image was adapted from: Lehn, J.-M. Toward Self-Organization and Complex Matter. *Science* **2002**, *295*, 2400-2403.

the understanding of rudimentary biological processes and explained phenomenon such as protein folding. Moreover, Watson and Cricks discovery of double-helical deoxyribonucleic acid (DNA) can be attributed to advances in supramolecular chemistry, as principles herein allowed them to recognize its structure is composed of two separate molecules.

Supermolecules represent a diverse set of structures including two-stranded molecules like DNA,[4] amphiphilic micelles[5] and infinite three-dimensional porous materials like metal organic frameworks,[1,2] etc. While several templating concepts can be used in the construction of supramolecular complexes, the thermodynamic nature of this class typically displays low energies and little to no activation energy which allows ease in their self-assembly without the need for excessive heating. The ability to predefine synthetic outcomes provides scientist with a great deal of control over the structure and function of nanomaterials.

Crystalline nanomaterials have been extensively studied as they display a wide range of characteristics and are applicable in many fields. One example is that of zeolites, aluminosilicate frameworks containing loosely bound cations and capable of serving as adsorbents as well as catalysts. Although these materials can occur naturally, they are also synthesized industrially and have the ability to accommodate several cations, rendering them somewhat tunable. These semi-tunable materials have proven success in gas storage, separation and recently as pharmacological agents.[6-9] The most notable pharmaceutical applications of zeolites include their inherent ability to sequester drug molecules including anti-

inflammatory drugs like aspirin, ibuprofen, etc. within their porous frameworks. Recent work has shown dehydrated zeolites can be used as blood-clotting agents and are commercially available for use.

A considerable amount of attention has been placed on the utilization of zeolites for natural gas processing. The catalytic conversion of methane to methanol or dimethyl ethers was reported using copper exchanged zeolites at low temperatures.[12-14] This catalytic oxidation of methanol serves as the first such example to directly generate methanol using molecular oxygen and reduces the steps associated with this reaction in addition to lowering cost from traditional methods using hydrogen peroxide catalysts. Additionally, the ever-increasing carbon dioxide emission levels makes zeolites attractive environmentally for the separation of CO_2 from flue and natural gases. This property has been reported in various accounts where CO_2 uptake is compared against nitric oxide, methane and hydrogen.

Although zeolites accomplishments are plentiful, their drawback centers on their composition of aluminum and silicon oxides. Varying the structure of zeolites is only capable through modifications of the Al/Si composition. Since the discovery of zeolites, materials with higher tunability and adsorption capabilities have been sought out. A multitude of porous materials have appeared including covalent organic molecules (COFs), which are extended solid networks composed entirely of light elements (B, C, N, O, Si). Like zeolites, COFs too are capable of serving as catalysts and have been observed to be mildly stable while storing gases such as

hydrogen, methane,[24] and carbon dioxide.[25-30] Despite the success of these materials, a desire for frameworks providing higher surface areas and chemical versatility still exists.

1.2 Applications of Metal Organic Frameworks

Composed of metal nodes interconnected by multi-dentate organic linkers, metal organic frameworks (MOFs) are three-dimensional porous nanomaterials (Figure 1.2). MOFs contain an advantage over other porous materials as a result of their high levels of tunability giving rise to a large number of possible metal node/organic linker combinations. Whilst investigations have mainly centered on

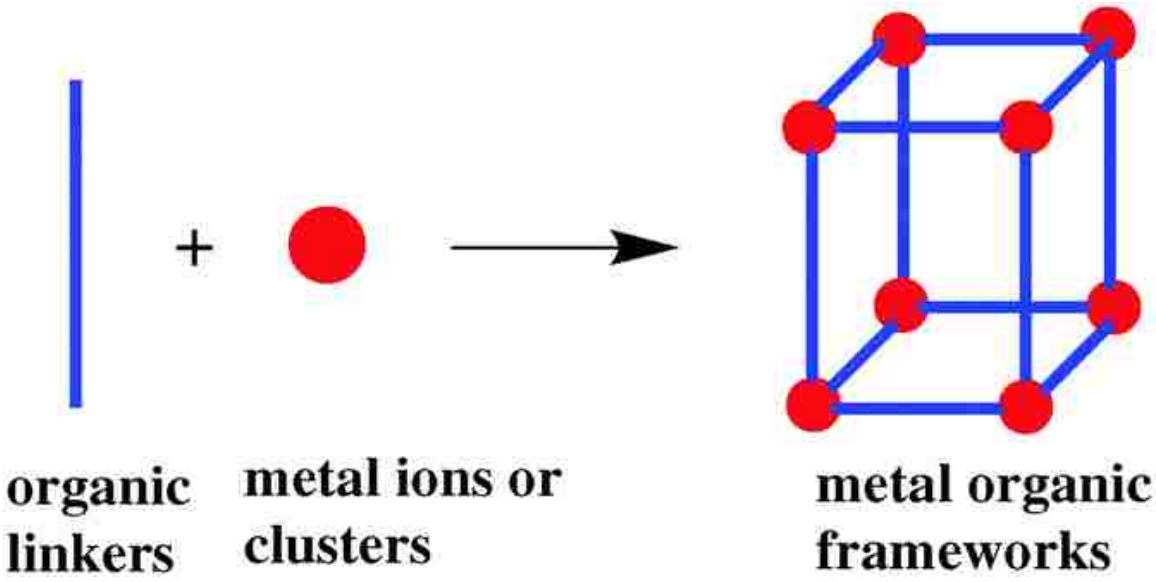

Figure 1.2. Shows the composition of metal organic frameworks (MOF) including multi-dentate organic linkers and metal centers. This image was adapted from: Dhakshinamoorthy, A.; Garcia, H. Metal-organic frameworks as solid catalysts for the synthesis of nitrogen-containing heterocycles. *Chemical Society Reviews* **2014**, *43*, 5750-5765.

their industrial work in catalysis, gas capture/adsorption and separation, these resilient nanomaterials have also shown promise as biosensors,[44-47] drug delivery vehicles and detoxifying agents. Several attractive features of MOFs include their high surface area[49,50] and void space,[38,51] capable of acting as a molecular sieve but flexible enough to be functionalized[53] to a researchers specific need.

As a result of their remarkable traits, MOFs have not only garnered attention academically but rather, these materials are also made industrially by giant corporations, including that of BASF, the worlds leading chemical company While there are a multitude of MOFs available in the literature, emphasis should be placed on the fact that there is a large possibility of metal node/organic linker combinations. Several research groups have set out in an attempt to predict potential contenders to currently available frameworks. Evidence for this is found in the Computation-Ready, Experimental (CoRE) MOF database in which over 4,000 predicted structures are available for researchers to attempt their syntheses.[53] Moreover, computational work is performed on the predicted MOFs contained within this database to demonstrate their potential for methane storage capacities, as this is a highly studied gaseous molecule for industrial work with MOFs.

While this database doesn't guarantee the feasibility for the predicted MOFs synthesis or application, it is an invaluable tool for MOF scientist in search of the predefined structures that should theoretically provide the intended experimental outcome. Several studies have investigated MOF-guest interactions for MOFs containing coordinatively undersaturated sites (CUS) through elimination of solvent

molecules from the framework pores. An example of a MOF containing CUS would be that of the HKUST-1 MOF which allows guest interactions to occur at the axial positions as the equatorial bonds are occupied by the oxygen's belonging to the carboxylate bearing organic linkers.[54,55] Studies performed by Valenzano et al. investigate the adsorption of CO, N_2 and CO_2 onto the coordinatively unsaturated Mg^{2+} center and reveal that these molecules adsorb in a 1:1 complex onto the metal center. While adsorption has been shown to occur at the metal center, it has also been shown that this too can occur at the site of the organic linker through chemical modifications.[57]

The ability to modify the framework post-synthesis with different molecules allows for extremely specific use of otherwise general frameworks. A current challenge for some MOFs is their poor stability in water due to an affinity for water molecules in undersaturated metal centers leading to the displacement of organic linkers. To circumvent issues with hydrothermal stabilities, attempts are underway to post-synthetically modify the structure of HKUST-1 using glycine due to its small size and ability to interact with the undersaturated copper sites as well as CO_2 in uptake studies.[58] Employment of MOFs for these studies proves important not only due to the ability to capture CO_2 but also resulting from high levels of selectivity exhibited from these materials.

The capacity of these materials for the storage of one gas over another reduces the need for further separation. McDonald et al. post-synthetically modified an extended analog of MOF-74, namely 4,4'-dioxido-3,3'-biphenyldicarboxylate

(M=Zn, Mg), with N,N'-dimethylethylenediamine creating the mmen-Mg2(dobpdc) framework.[58] This framework adsorbed CO_2 from air and dry flue gas sources and showed a high level of selectivity of CO_2 over N_2 and O_2 gases. Moreover, the purity of the CO_2 gas adsorbed was reported as 96% from air and 98% for the dry flue gas. This serves as an example of the exceptional results to be obtained from the functionalization of general frameworks.

MOFs provide a substrate with relatively high surface areas that can be advantageous in an array of fields. Researchers at Northwestern University synthesized two MOFs, NU-109 and NU-110, that shattered previous records for surface area and are theorized as nearly approaching the 10,577 m^2/g theoretical upper limits of surface area for solid materials.[59] Further work by this group suggests that the previously accepted Brunauer-Emmett-Teller (BET) surface areas are capable of being surpassed and that these materials display surface areas over 7,000 m^2/g, larger than that of a football field.[60,61] These remarkable characteristics of MOFs are merely the beginning of their extraordinary feats; intriguingly, MOFs also exhibit the ability to breathe or change their volume in response to their environment, all the while remaining intact.

Although MOFs have presented an ever-increasing list of attractive properties quite relevant to gases, they have recently come into light as potential carriers of biomolecules such as proteins,[63] drugs,[64] and DNA[65] due to the enhanced level of control attributed to these frameworks. Further evidence of the versatility of MOFs is apparent in the zirconium based UiO-66-N3 nano-MOF. This MOF is

functionalized through a copper-free click reaction resulting in the first report of a MOF nanoparticle-nucleic acid conjugate with high stability and capable of cellular entry.[66-68] These remarkable materials show vast biological differences from that of their un-functionalized analogs. As a result of the high level of control and chemical stability of MOFs, efforts have focused on their use in conjunction with troublesome molecules including free radicals.

1.3 History of Nitric Oxide

Known for its powerful role in vasodilation, nitric oxide (Figure 1.3) is a gaseous free radical signaling molecule (neurotransmitter) with antianginal, antithrombotic[75-78] and antibacterial properties. Nitric oxide has not always been looked upon as a molecule deserving of such praise. Initially investigated due to its identification as an environmental pollutant, nitric oxide's biological role was unknown. Even more ironic is the fact that the endothelium growth factor (EGF) was coined as an important molecule but at the time its relationship to nitric oxide had yet to be revealed. It wasn't until the 1980's that Ignarro et al. identified nitric oxide as EGF.

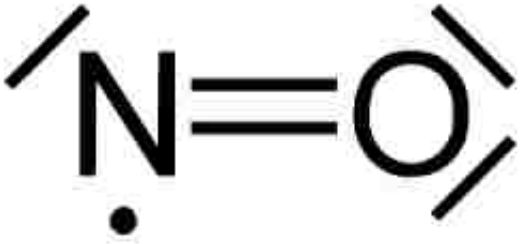

Figure 1.3. shows the biologically active nitric oxide free radical.

This highly reactive, endogenous signaling molecule can be produced in the endothelium as conversion of amino acid L-arginine into nitric oxide occurs through

nitric oxide synthases (NOS).[81] The mechanism of nitrosovasodilation, nitric oxides most known pharmacological properties, stems from a cascade of events including 1) the activation of guanylyl-cyclase, an enzyme located within smooth muscle cells and platelets 2) that elevates levels of guanylyl phosphate (GMPc) ultimately resulting in smooth muscle relaxation.[82] Unfortunately, superoxides have a high affinity towards free radicals thus making nitric oxide susceptible to rapid conversion into peroxynitrite.[83] Despite its short existence, nitric oxide has vast potential in therapeutically affecting surrounding structures.

Consequently, nitric oxide is also used to treat conditions such as erectile dysfunction disorder and diseases such as angina or heart pain by allowing blood to flow more freely. Resulting from its ability to relax smooth muscle cells, nitric oxide inhalation therapy was demonstrated to selectively reverse pulmonary hypertension.[80,84,85] The strong vasodilator effects of nitric oxide have led to its incorporation into pharmaceutical agents including that of the inhaled vasodilator INOmax and sildenafil (Viagra). Furthermore, nitric oxide has the capability of preventing or treating blood clots due to its antithrombotic nature. Benefits of nitric oxide aren't halted at the blood vessels but rather extend to many other organs including that of the liver (ischemic damage).

1.4 Nitric Oxide Donors

There are several methods for the delivery of nitric oxide both efficiently (loading) and effectively (delivery). While increasing the capacity of nitric oxide that

can be delivered is a step toward a feasible solution, it too could be argued that a mechanism capable of protecting nitric oxide from reacting prematurely should be constructed. Several classes of nitric oxide donors exist with some of the common examples being diazeniumdiolates (NONOates) and S-nitrosothiols (RSNOs). Observed in 1960, diethylamine-NONOate was the first reported NONOate and contains a chemical structure composed of a diolate group [$(NO)NO^-$] connected through a nitrogen atom [$R_2N(NO)NO^-$]. An attractive feature of NONOates as nitric oxide donors is the generation of 2 moles of nitric oxide upon the decomposition of this molecule. Induction of nitric oxide release can be controlled through pH and temperature without the presence of a catalyst and occurs on the order of seconds to hours depending on the NONOate used.

Employment of NONOates as nitric oxide storage and delivery vehicles has been reported extensively. The use of thermo-sensitive liposomes to mediate nitric oxide release was explored by Saraiva *et. al* through the use of an encapsulated NONOate namely, spermine (Figure 1.4).[80] Release of nitric oxide from this carrier depends on temperature to produce a pH gradient across a membrane, ultimately releasing nitric oxide.[88] This method has the potential to modulate nitric oxide release through phospholipid composition and the variability of the pH gradient.

Pulmonary vascular resistance studies have frequently turned to nitric oxide therapy for treatment.[89] Consequently, NONOates have been chosen as inhalation prodrugs to treat this disease. Furthermore, the reported use of NONOates depicts their ability to maintain blood pressure during pulmonary resistance treatment. In

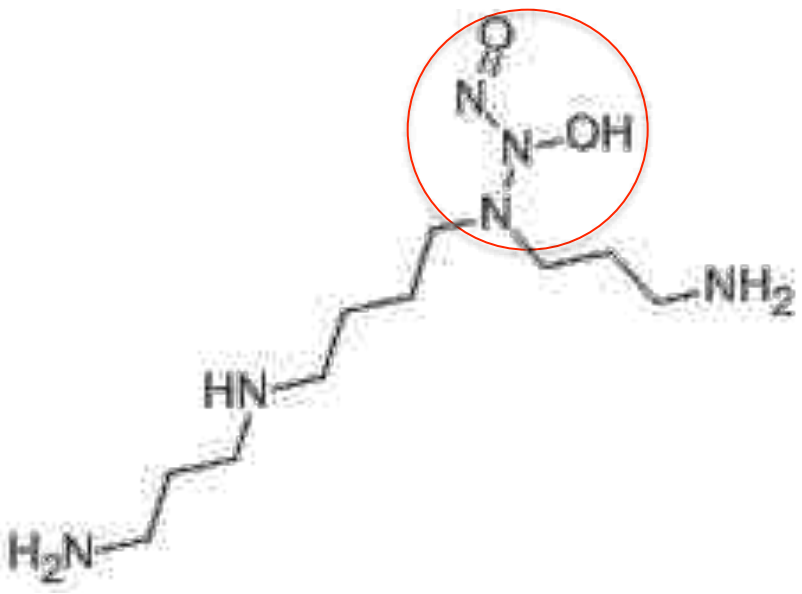

Figure 1.4. The chemical structure of spermine, a NONOate is shown. Circled in red is the characteristic diolate-amine group of NONOates.

addition to the previously mentioned use of NONOates, treatment of thrombosis has been suggested through NONOate usage.[90] The success of NONOates makes these materials idea candidates for pharmaceutical agents but no clinical trials have been reported to date.[91,92]

Another subset of nitric oxide donors is that of S-nitrosothiols (RSNOs), organic compounds containing a nitroso group linked through a sulfur atom (Figures 1.5, 1.6). Known as bio-reservoirs for nitric oxide within the body, RSNOs naturally occur in relatively large concentrations within the body. S- nitrosoglutathione (GSNO) and S-nitrosocysteine (CysNO) are

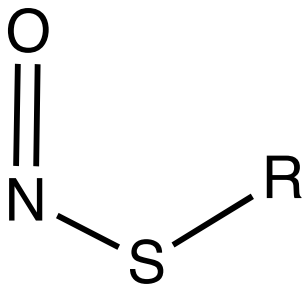

Figure 1.5. The general structure of a s-nitrosothiol where the R-group refers to an organic group.

two RSNOs found in high concentrations within the body and thus commonly studied.[91] GSNO is known for its ability to spontaneously release nitric oxide while inhibiting NF-κB[91] (a transcription protein) and platelet activation.[91] Moreover, GSNOs release of nitric oxide can occur directly or indirectly by the generation of s-nitroso-cysteinyl-glycine (CysNOGly) mediated through enzymatic cleavage by gamma-glutamyltransferase (GGT).[94] CysNO has been implied to be more reactive

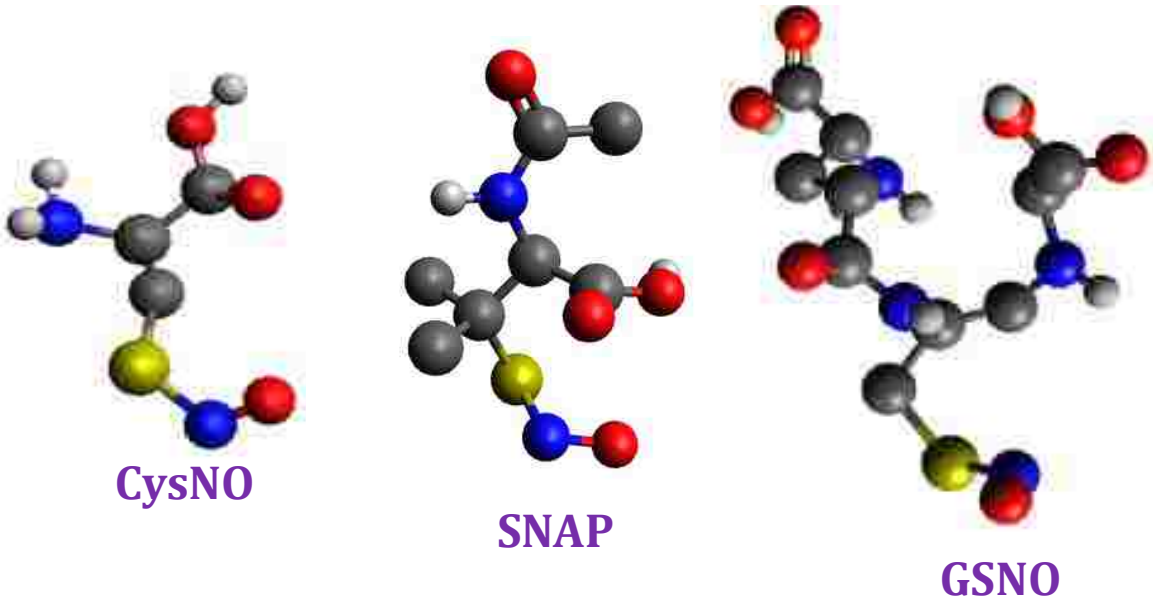

Figure 1.6. Nitrosylated amino acids known as s-nitrosothiols (RSNOs) capable of releasing nitric oxide through cleavage of the S-N bond.

than GSNO suggesting that its release of nitric oxide is more likely.[80]

In addition to these naturally occurring RSNOs, several synthetic RSNOs are commonly investigated for their ability to release nitric oxide through decomposition reactions. Similar in structure to CysNO, S-nitroso-N-acetylpenicillamine (SNAP) is a synthetic RSNO derived from penicillamine; commonly used for its spontaneous release of nitric oxide and inhibition of cysteine

proteases. This RSNO contains the same backbone as CysNO with the addition of an acetyl group to the amino group and two additional methyl groups. As a result of the potential decomposition of GSNO, it is imperative to probe systems with several RSNOs, as a mixture of multiple RSNOs is likely present in vivo.

RSNOs are intriguing nitric oxide donors as they are naturally found within the body at high concentrations and capable of nitric oxide release through photolysis or the presence of thiols, enzymes (including metals) and superoxides.[94] Furthermore, RSNOs can act as a chain of nitric oxide donors through transnitrosation of available thiols within the body; use of these nitrosylated organics circumvents complications associated with the occurrence of tolerance commonly seen in clinical drugs.

Successful research on nitric oxide precursors has led to the availability of valuable prodrugs including sodium nitroprusside, nitroglycerine, etc (Figure 1.7). Nitroglycerine is an organic nitrate commonly used for angina, or chest pain treatment. Administration of this drug occurs in various forms including transdermal patches along with ointments.[94] Despite the inclusion of three nitrate groups (nitro-oxy esters), only one mole of nitric oxide is produced by the prodrug upon activation. Several issues are posed with these prodrugs including the dependence of nitroglycerine on thiols (like GSH, etc.) in addition to the development of tolerance to treatment.[95] Further understanding of the mechanism associated with the development of resistance in nitric oxide prodrugs is needed.

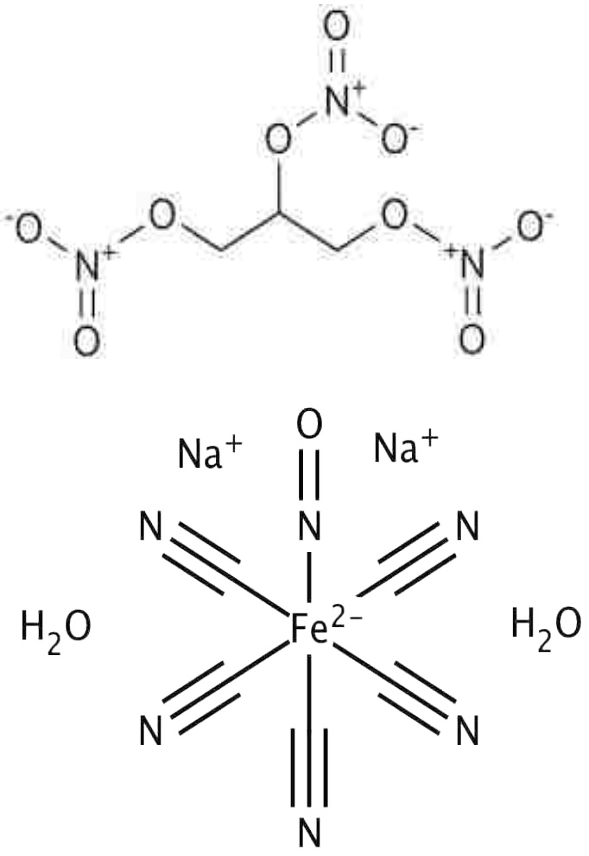

Figure 1.7. Two nitric oxide releasing drugs used clinically **(top)** nitroglycerin **(bottom)** sodium nitroprusside.

Some studies have proposed that tolerance results from failed bioconversion of nitrates to nitric oxide and rapid clearance of nitric oxide through superoxides.[95]

Frequently used in hospitals to rapidly treat elevated blood pressure typically occurring in hypertensive crises,[80] sodium nitroprusside is regarded as the drug of choice for vasodilation in clinical studies. This inorganic red sodium salt is composed of five cyanide groups along with one nitroso group bound to an iron center in an octahedral geometry.[80] Unlike nitroglycerin, sodium nitroprusside safety can be compromised by the release of the cyanide groups as cyanidosis in long-term use has been reported.[96] A further limitation of this prodrug includes its decomposition through photolysis and sole administration through intravenous routes.

Recent developments in nitric oxide research have led to the design and synthesis of nitric oxide containing non-steroidal anti-inflammatory drugs (NO-

NSAIDS). [97] The administration of two compounds to animal subjects (rats) successfully fulfilled their goal of protecting against gastrointestinal complications through the presence of nitric oxide.[80,98] Although nitric oxide is a proven candidate in the treatment of numerous diseases, its high level of reactivity makes working with nitric oxide a laborious task. Consequently, a number of research efforts are focused on the fabrication of adequate delivery vehicles in which appreciable amounts of nitric oxide can be loaded and delivered efficiently to eliminate existing issues with nitric oxide prodrugs.

1.5 Delivery Methods of Nitric Oxide

A successful drug delivery vehicle must be capable of storing the molecule of interest in appreciable amounts and delivering it to the intended target with minimal drug loss, reducing the chance of side effects. Furthermore, it's imperative that there is no adverse reactivity between the host and guest molecules. Lastly, it is important that guest molecule must be releasable from the delivery vehicle in a slow and sustained manner. Although nitric oxide is known for its physiological roles, including being named molecule of the year in 1992, its benefits are overshadowed due to difficulties in storage and subsequent transport to the desired target. One of the major obstacles associated with this free radical is its bioavailability and relatively short half-life of seconds in the blood stream, one too short to deliver directly, thus limiting the extent of nitric oxide use in pharmaceuticals.

Without a feasible exogenous drug delivery vehicle for nitric oxide and

molecules with similar chemical and physical characteristics, a gap in the discovery of highly effective drugs and available treatments may exist. In order to circumvent these shortcomings, the scientific community has been charged with the task of bridging this gap. The bridging of this gap requires extensive study of several nanomaterials including that of zeolites, COFs, liposomes, nanoparticles, polymers and MOFs to focus on their potential role in nitric oxide drug delivery. Whilst overcoming issues associated with nitric oxides reactivity is of relative importance, one must presume that identifying current shortcomings with available transporters is paramount to move forward in the construction of new drug delivery vehicles. Currently cited issues with nitric oxide-transport through the use of nanomaterials includes biocompatibility and the fact that appreciable amounts of nitric oxide are not always capable of being stored or delivered.

On the quest for adequate nitric oxide loading and delivery, many materials including nanogels,[100] micelles,[101] nanoparticles[102-104] and self-assembled monolayers have been used in addition to the exploration of MOFs. Several cases of zeolite storage and transport of nitric oxide have been proposed. [7] The use of a zeolitic compound termed Zeolite A is commercially used in detergents,[8,65] but researchers have demonstrated its use in biomedical applications. Incorporation of Zeolite A into polymeric fibers provides the first case in which zeolites are used to construct nitric oxide releasing bandages.[65] While decreases in nitric oxide release rates are desired, methods to further extend the timeframe of nitric oxide release through precursors are sought out. One such example of this includes the use of the MCM-41 zeolite to store nitric oxide after catalytically generating nitric oxide from

nitrite ions, further slowing down nitric oxide depletion. [107]

Unlike MOFs, zeolites exhibit poor tunability as only subtle changes to the transition metal sequestered within the pores can be exchanged to affect adsorbed amounts of nitric oxide.[29,62,90,108-110] To obtain further tunability, research efforts should be directed towards MOFs for greater control of nitric oxide storage and delivery. The stimuli responsive nature of MOFs has gained recent interest for their potential roles as drug storage and delivery vehicles. The transportation of once cumbersome molecules including nitric oxide has been made possible. Biomedical applications of MOFs have been cited with a notable case involving vasodilation through the use of NO-loaded MOFs. Successful demonstration of vasodilation has occurred on the coronary arteries of pigs in which measured vasodilation was higher in MOF-mediated nitric oxide release versus free nitric oxide control studies.[51,55,112,113]

A myriad of MOFs capable of adequate storage and subsequent release of nitric oxide has been detailed in literature. The most common metal center nodes present in these studies include copper, nickel, iron, zinc and magnesium. The CPO-27 (M=Zn, Ni, Mg) class of MOFs has been probed for their capacity to store nitric oxide at the undersaturated metal center upon evacuation of the coordinated solvent.[112,114] Results of this study reveal the nitric oxide releasing properties of these MOFs; however, the nickel compound exudes higher levels of nitric oxide release in addition to higher levels of toxicity.

Due to contrasting results of the different metal centers, efforts were made to

fabricate mixed-MOF systems to capture the benefits of presenting two separate metals within a single framework. This led the Morris group to compare results from a CPO-27 MOF with varying compositions of Mg/Ni and Zn/Ni. It was concluded that an increase of nitric oxide uptake from 4 nitric oxide molecules to 20 occurs upon the incorporation of Ni at 40% composition within the Mg-CPO-27 framework. Furthermore, introduction of Mg-CPO-27 to humid conditions triggered little to no release of nitric oxide. Doping of this MOF with increasing levels of Ni (40%) produces 6 additional nitric oxide molecules per unit cell under humid conditions.

Due to the level of variability in the composition of MOFs, additional modifications within the framework can be exploited to alter the amounts and rates of nitric oxide release. In conjunction with a search of adequate delivery systems, researchers have also proposed the functionalization of MOFs via organic linkers or metal centers with amine groups to allow the formation of NONOates upon nitric oxide adsorption. While this allows for a great deal of control over nitric oxide release, it requires post-synthetic modification, which requires much care to synthesize the desired materials. As an alternative to the direct loading of nitric oxide or the required functionalization of MOFs with secondary amines, recent experimental work has shown that nitric oxide can be stored chemically as s-nitrosocysteine (CysNO) and used in conjunction with HKUST-1.[115] The release of stored nitric oxide from CysNO is the consequence of a decomposition reaction that takes place in the presence of a catalyst, which in this case is the MOF-bound copper ion.

$$2RSNO \xrightarrow{Cu^{+},\ RSH} RSSR + 2NO$$

(Equation 1.1)

Work performed by Harding et al. compared the rates of nitric oxide released from a solution of free copper ions within an ethanol solvent to the HKUST-1 framework.[115,116] Conclusions drawn from their work imply that the presence of HKUST-1 plays a role in slowing the release rate of nitric oxide from approximately 20 min to over 10 hr. Although this study lacked the complete mechanism for which CysNO was decomposed into free nitric oxide, it provided the authors with a high level of certainty that a thiol (RSH) was necessary. Moreover, this was the first time in which nitric oxide was chemically stored in the form of a RSNO and loaded into a MOF to demonstrate a slow, controlled and sustained level of nitric oxide release.

1.6 Introduction to Silylenol Formation

Natural products are small organic molecules produced by an array of organisms with no involvement in the critical functions of an organism. The diverse chemical structure and function of these materials gives rise to widespread use as pharmaceuticals. Several examples exist outlining the pharmacological activity exhibited by these molecules including their use as antimicrobials, anticancer[118] and anti-inflammatory agents.[119] The structural complexity of many natural products underlies the synthetic challenges associated with the fabrication of natural product inspired molecules. Development of novel chemistries capable of

facilitating the challenging synthetic routes in natural product synthesis is an area of interest for many scientists. Of particular importance is the incorporation of an indole to a disubstituted ketone through a S_{N1} reaction mechanism to yield a single silylenol ether product. The feasibility of this reaction requires the use of an oxyallyl cation intermediate.

While Ayala et al. successfully demonstrated the use of this synthetic route to produce the silylenol ether at yields of up to 91% with complete regiocontrol, an explanation for the 99:1 regioselectivity at the α' versus the α position of the silyloxyallyl carbocation was lacking.[1] Further work involved the investigation of methoxy substituted ketones; intriguingly, these molecules were responsible for a nearly 1:1 production of α/α' functionalized methoxyenol ethers. Employment of electronic structure calculations allows probing of the thermodynamic properties of this system where the complete reaction mechanism was mapped out. It is the overarching goal of this research to determine the source of regioselectivity in disubstituted silyl-containing ketones as the nucleophilic attack of a methoxy containing ketone fails to encompass this level of regiocontrol.

1.7 Dissertation Overview

Work contained herein focuses on understanding chemical reactions from an atomistic level through quantum calculations and classical molecular dynamics simulations. The first project pertains to the chemical storage and delivery of nitric oxide through the use of copper based MOFs as catalytic centers. To accurately

model this system for study, parameterization of key interactions using the genetic algorithm and least squares method was performed and before the start of MD simulations where the free energy of RSNO's approach to the metal center was further studied. The second part of this work focuses on probing thermodynamic properties of an S_{N1} reaction mechanism where the reactants, products and relevant transition states, were obtained through electronic structure calculations and used to determine factors that affect the selectivity of indole addition.

Chapter 2 will describe all quantum calculations used for metal organic frameworks including the methods used to optimize reactants and products of the guest molecules. Location of relevant transition states and their confirmation through the intrinsic reaction coordinate (IRC) methods for the elucidation of the reaction pathway will be performed. Lastly, steps taken for force field development needed for subsequent molecular dynamics simulations of the free copper/ethanol solution and MOF environment will be described herein.

Chapter 3 will provide an introduction to classical molecular dynamics (MD) simulations, statistical mechanics and enhanced sampling methods. Furthermore, parameters from the in-house derived force field in conjunction with the Dreiding force field are used to measure free energy changes upon the approach of RSNO to the catalytic center in the presence and absence (free copper solution) of the complex MOF environment. Lastly, insight into changes within the solvation environment of the catalytic center will be probed upon RSNOs approach through the calculation of radial distribution functions.

Chapter 4 centers on the use of electronic structure calculations to investigate the origins of regioselectivity by the stepwise mechanism for the S_{N1} reaction of various oxyallyl cations and the nucleophilic addition of an indole. Chapter 5 is the reserved to discuss conclusions drawn from all work presented herein.

1.8 References

(1) Lehn, J.-M.: From Molecular to Supramolecular Chemistry. In *Supramolecular Chemistry*; Wiley-VCH Verlag GmbH & Co. KGaA, 2006; pp 1-9.

(2) McLaughlin, C. K.; Hamblin, G. D.; Sleiman, H. F. Supramolecular DNA assembly. *Chemical Society Reviews* **2011**, *40*, 5647-5656.

(3) Chen, Y.; Dong, C.-M. pH-Sensitive Supramolecular Polypeptide-Based Micelles and Reverse Micelles Mediated by Hydrogen-Bonding Interactions or Host–Guest Chemistry: Characterization and In Vitro Controlled Drug Release. *The Journal of Physical Chemistry B* **2010**, *114*, 7461-7468.

(4) Reger, D. L.; Leitner, A.; Pellechia, P. J.; Smith, M. D. Framework Complexes of Group 2 Metals Organized by Homochiral Rods and π···π Stacking Forces: A Breathing Supramolecular MOF. *Inorganic Chemistry* **2014**, *53*, 9932-9945.

(5) Davis, M. E. Zeolites from a Materials Chemistry Perspective. *Chemistry of Materials* **2014**, *26*, 239-245.

(6) Pagis, C.; Morgado Prates, A. R.; Farrusseng, D.; Bats, N.; Tuel, A. Hollow Zeolite Structures: An Overview of Synthesis Methods. *Chemistry of Materials* **2016**, *28*, 5205-5223.

(7) Su, F.; Lu, C. CO2 capture from gas stream by zeolite 13X using a dual-column temperature/vacuum swing adsorption. *Energy & Environmental Science* **2012**, *5*, 9021-9027.

(8) Mofarahi, M.; Gholipour, F. Gas adsorption separation of CO2/CH4 system using zeolite 5A. *Microporous and Mesoporous Materials* **2014**, *200*, 1-10.

(9) Amorim, R.; Vilaça, N.; Martinho, O.; Reis, R. M.; Sardo, M.; Rocha, J.; Fonseca, A. M.; Baltazar, F.; Neves, I. C. Zeolite Structures Loading with an Anticancer Compound As Drug Delivery Systems. *The Journal of Physical Chemistry C* **2012**, *116*, 25642-25650.

(10) Datt, A.; Fields, D.; Larsen, S. C. An Experimental and Computational Study of the Loading and Release of Aspirin from Zeolite HY. *The Journal of Physical Chemistry C* **2012**, *116*, 21382-21390.

(11) Krajišnik, D.; Daković, A.; Malenović, A.; Kragović, M.; Milić, J. Ibuprofen sorption and release by modified natural zeolites as prospective drug carriers. *Clay Minerals* **2015**, *50*, 11-22.

(12) Khodaverdi, E.; Honarmandi, R.; Alibolandi, M.; Baygi, R. R.; Hadizadeh, F.; Zohuri, G. Evaluation of synthetic zeolites as oral delivery vehicle for anti-inflammatory drugs. *Iranian Journal of Basic Medical Sciences* **2014**, *17*, 337-343.

(13) Arnaud, F.; Tomori, T.; Carr, W.; McKeague, A.; Teranishi, K.; Prusaczyk, K.; McCarron, R. Exothermic Reaction in Zeolite Hemostatic Dressings: QuikClot ACS and ACS+®. *Annals of Biomedical Engineering* **2008**, *36*, 1708-1713.

(14) Li, J.; Cao, W.; Lv, X.-x.; Jiang, L.; Li, Y.-j.; Li, W.-z.; Chen, S.-z.; Li, X.-y. Zeolite-based hemostat QuikClot releases calcium into blood and promotes blood coagulation in vitro. *Acta Pharmacol Sin* **2013**, *34*, 367-372.

(15) Narsimhan, K.; Iyoki, K.; Dinh, K.; Román-Leshkov, Y. Catalytic Oxidation of Methane into Methanol over Copper-Exchanged Zeolites with Oxygen at Low Temperature. *ACS Central Science* **2016**, *2*, 424-429.

(16) Hammond, C.; Forde, M. M.; Ab Rahim, M. H.; Thetford, A.; He, Q.; Jenkins, R. L.; Dimitratos, N.; Lopez-Sanchez, J. A.; Dummer, N. F.; Murphy, D. M.; Carley, A. F.; Taylor, S. H.; Willock, D. J.; Stangland, E. E.; Kang, J.; Hagen, H.; Kiely, C. J.; Hutchings, G. J. Direct Catalytic Conversion of Methane to Methanol in an Aqueous Medium by using Copper-Promoted Fe-ZSM-5. *Angewandte Chemie International Edition* **2012**, *51*, 5129-5133.

(17) Zhao, Z.-J.; Kulkarni, A.; Vilella, L.; Nørskov, J. K.; Studt, F. Theoretical Insights into the Selective Oxidation of Methane to Methanol in Copper-Exchanged Mordenite. *ACS Catalysis* **2016**, *6*, 3760-3766.

(18) Zhang, X.-L.; Qiu, L.-F.; Ding, M.-Z.; Hu, N.; Zhang, F.; Zhou, R.-F.; Chen, X.-S.; Kita, H. Preparation of Zeolite T Membranes by a Two-Step Temperature Process for CO2 Separation. *Industrial & Engineering Chemistry Research* **2013**, *52*, 16364-16374.

(19) Wang, B.; Ho, W. S. W.; Figueroa, J. D.; Dutta, P. K. Bendable Zeolite Membranes: Synthesis and Improved Gas Separation Performance. *Langmuir* **2015**, *31*, 6894-6901.

(20) Aguado, S.; Bergeret, G.; Daniel, C.; Farrusseng, D. Absolute Molecular Sieve Separation of Ethylene/Ethane Mixtures with Silver Zeolite A. *Journal of the American Chemical Society* **2012**, *134*, 14635-14637.

(21) Waller, P. J.; Gándara, F.; Yaghi, O. M. Chemistry of Covalent Organic Frameworks. *Accounts of Chemical Research* **2015**, *48*, 3053-3063.

(22) Xu, H.; Gao, J.; Jiang, D. Stable, crystalline, porous, covalent organic frameworks as a platform for chiral organocatalysts. *Nat Chem* **2015**, *7*, 905-912.

(23) Ding, S.-Y.; Gao, J.; Wang, Q.; Zhang, Y.; Song, W.-G.; Su, C.-Y.; Wang, W. Construction of Covalent Organic Framework for Catalysis: Pd/COF-LZU1 in Suzuki–Miyaura Coupling Reaction. *Journal of the American Chemical Society* **2011**, *133*, 19816-19822.

(24) Ganz, E.; Dornfeld, M. Energetics and Thermodynamics of the Initial Stages of Hydrogen Storage by Spillover on Prototypical Metal–Organic Framework and Covalent–Organic Framework Materials. *The Journal of Physical Chemistry C* **2014**, *118*, 5657-5663.

(25) Srepusharawoot, P.; Scheicher, R. H.; Moysés Araújo, C.; Blomqvist, A.; Pinsook, U.; Ahuja, R. Ab Initio Study of Molecular Hydrogen Adsorption in Covalent Organic Framework-1. *The Journal of Physical Chemistry C* **2009**, *113*, 8498-8504.

(26) Mendoza-Cortes, J. L.; Pascal, T. A.; Goddard, W. A. Design of Covalent Organic Frameworks for Methane Storage. *The Journal of Physical Chemistry A* **2011**, *115*, 13852-13857.

(27) Babarao, R.; Custelcean, R.; Hay, B. P.; Jiang, D.-e. Computer-Aided Design of Interpenetrated Tetrahydrofuran-Functionalized 3D Covalent Organic Frameworks for CO2 Capture. *Crystal Growth & Design* **2012**, *12*, 5349-5356.

(28) Aguirre-Díaz, L. M.; Gándara, F.; Iglesias, M.; Snejko, N.; Gutiérrez-Puebla, E.; Monge, M. Á. Tunable Catalytic Activity of Solid Solution Metal–Organic

Frameworks in One-Pot Multicomponent Reactions. *Journal of the American Chemical Society* **2015**, *137*, 6132-6135.

(29) Wilmer, C. E.; Leaf, M.; Lee, C. Y.; Farha, O. K.; Hauser, B. G.; Hupp, J. T.; Snurr, R. Q. Large-scale screening of hypothetical metal–organic frameworks. *Nat Chem* **2012**, *4*, 83-89.

(30) Zhang, Y.-B.; Furukawa, H.; Ko, N.; Nie, W.; Park, H. J.; Okajima, S.; Cordova, K. E.; Deng, H.; Kim, J.; Yaghi, O. M. Introduction of Functionality, Selection of Topology, and Enhancement of Gas Adsorption in Multivariate Metal–Organic Framework-177. *Journal of the American Chemical Society* **2015**, *137*, 2641-2650.

(31) Rowsell, J. L. C.; Yaghi, O. M. Metal–organic frameworks: a new class of porous materials. *Microporous and Mesoporous Materials* **2004**, *73*, 3-14.

(32) Colon, Y. J.; Snurr, R. Q. High-throughput computational screening of metal-organic frameworks. *Chemical Society Reviews* **2014**, *43*, 5735-5749.

(33) Orellana-Tavra, C.; Baxter, E. F.; Tian, T.; Bennett, T. D.; Slater, N. K.; Cheetham, A. K.; Fairen-Jimenez, D. Amorphous metal–organic frameworks for drug delivery. *Chemical Communications* **2015**, *51*, 13878-13881.

(34) Jenness, G. R.; Schmidt, J. R. Unraveling the Role of Metal–Support Interactions in Heterogeneous Catalysis: Oxygenate Selectivity in Fischer–Tropsch Synthesis. *ACS Catalysis* **2013**, *3*, 2881-2890.

(35) Chughtai, A. H.; Ahmad, N.; Younus, H. A.; Laypkov, A.; Verpoort, F. Metal-organic frameworks: versatile heterogeneous catalysts for efficient catalytic organic transformations. *Chemical Society Reviews* **2015**, *44*, 6804-6849.

(36) Yang, D.; Odoh, S. O.; Wang, T. C.; Farha, O. K.; Hupp, J. T.; Cramer, C. J.; Gagliardi, L.; Gates, B. C. Metal–Organic Framework Nodes as Nearly Ideal Supports for Molecular Catalysts: NU-1000- and UiO-66-Supported Iridium Complexes. *Journal of the American Chemical Society* **2015**, *137*, 7391-7396.

(37) He, Y.; Zhou, W.; Qian, G.; Chen, B. Methane storage in metal-organic frameworks. *Chemical Society Reviews* **2014**, *43*, 5657-5678.

(38) Bae, Y.-S.; Hauser, B. G.; Farha, O. K.; Hupp, J. T.; Snurr, R. Q. Enhancement of CO2/CH4 selectivity in metal-organic frameworks containing lithium cations. *Microporous and Mesoporous Materials* **2011**, *141*, 231-235.

(39) Haldoupis, E.; Borycz, J.; Shi, H.; Vogiatzis, K. D.; Bai, P.; Queen, W. L.; Gagliardi, L.; Siepmann, J. I. Ab Initio Derived Force Fields for Predicting CO2 Adsorption and Accessibility of Metal Sites in the Metal–Organic Frameworks M-MOF-74 (M = Mn, Co, Ni, Cu). *The Journal of Physical Chemistry C* **2015**, *119*, 16058-16071.

(40) McDaniel, J. G.; Li, S.; Tylianakis, E.; Snurr, R. Q.; Schmidt, J. R. Evaluation of Force Field Performance for High-Throughput Screening of Gas Uptake in Metal–Organic Frameworks. *The Journal of Physical Chemistry C* **2015**, *119*, 3143-3152.

(41) Li, J.-R.; Kuppler, R. J.; Zhou, H.-C. Selective gas adsorption and separation in metal-organic frameworks. *Chemical Society Reviews* **2009**, *38*, 1477-1504.

(42) Alawisi, H.; Li, B.; Alfooty, K.; Wu, L.; Xiang, S.; Wang, H.; Chen, B. A two dimensional microporous metal-organic framework for selective gas separation. *Inorganic Chemistry Communications* **2014**, *50*, 106-109.

(43) Bae, Y.-S.; Mulfort, K. L.; Frost, H.; Ryan, P.; Punnathanam, S.; Broadbelt, L. J.; Hupp, J. T.; Snurr, R. Q. Separation of CO2 from CH4 Using Mixed-Ligand Metal–Organic Frameworks. *Langmuir* **2008**, *24*, 8592-8598.

(44) Kim, K. C.; Lee, C. Y.; Fairen-Jimenez, D.; Nguyen, S. T.; Hupp, J. T.; Snurr, R. Q. Computational Study of Propylene and Propane Binding in Metal–Organic Frameworks Containing Highly Exposed Cu+ or Ag+ Cations. *The Journal of Physical Chemistry C* **2014**, *118*, 9086-9092.

(45) Verma, P.; Xu, X.; Truhlar, D. G. Adsorption on Fe-MOF-74 for C1–C3 Hydrocarbon Separation. *The Journal of Physical Chemistry C* **2013**, *117*, 12648-12660.

(46) Wu, X.-Q.; Ma, J.-G.; Li, H.; Chen, D.-M.; Gu, W.; Yang, G.-M.; Cheng, P. Metal-organic framework biosensor with high stability and selectivity in a bio-mimic environment. *Chemical Communications* **2015**, *51*, 9161-9164.

(47) Wang, X.; Lu, X.; Wu, L.; Chen, J. 3D metal-organic framework as highly efficient biosensing platform for ultrasensitive and rapid detection of bisphenol A. *Biosensors and Bioelectronics* **2015**, *65*, 295-301.

(48) Liu, Y.; Moon, S.-Y.; Hupp, J. T.; Farha, O. K. Dual-Function Metal–Organic Framework as a Versatile Catalyst for Detoxifying Chemical Warfare Agent Simulants. *ACS Nano* **2015**, *9*, 12358-12364.

(49) DeCoste, J. B.; Demasky, T. J.; Katz, M. J.; Farha, O. K.; Hupp, J. T. A UiO-66 analogue with uncoordinated carboxylic acids for the broad-spectrum removal of toxic chemicals. *New Journal of Chemistry* **2015**, *39*, 2396-2399.

(50) Mondloch, J. E.; Katz, M. J.; Isley Iii, W. C.; Ghosh, P.; Liao, P.; Bury, W.; Wagner, G. W.; Hall, M. G.; DeCoste, J. B.; Peterson, G. W.; Snurr, R. Q.; Cramer, C. J.; Hupp, J. T.; Farha, O. K. Destruction of chemical warfare agents using metal–organic frameworks. *Nat Mater* **2015**, *14*, 512-516.

(51) Grunker, R.; Bon, V.; Muller, P.; Stoeck, U.; Krause, S.; Mueller, U.; Senkovska, I.; Kaskel, S. A new metal-organic framework with ultra-high surface area. *Chemical Communications* **2014**, *50*, 3450-3452.

(52) Farha, O. K.; Özgür Yazaydın, A.; Eryazici, I.; Malliakas, C. D.; Hauser, B. G.; Kanatzidis, M. G.; Nguyen, S. T.; Snurr, R. Q.; Hupp, J. T. De novo synthesis of a metal–organic framework material featuring ultrahigh surface area and gas storage capacities. *Nat Chem* **2010**, *2*, 944-948.

(53) Furukawa, H.; Ko, N.; Go, Y. B.; Aratani, N.; Choi, S. B.; Choi, E.; Yazaydin, A. Ö.; Snurr, R. Q.; O'Keeffe, M.; Kim, J.; Yaghi, O. M. Ultrahigh Porosity in Metal-Organic Frameworks. *Science* **2010**, *329*, 424-428.

(54) Chang, N.; Gu, Z.-Y.; Wang, H.-F.; Yan, X.-P. Metal–Organic-Framework-Based Tandem Molecular Sieves as a Dual Platform for Selective Microextraction and High-Resolution Gas Chromatographic Separation of n-Alkanes in Complex Matrixes. *Analytical Chemistry* **2011**, *83*, 7094-7101.

(55) Lowe, A.; Chittajallu, P.; Gong, Q.; Li, J.; Balkus Jr, K. J. Storage and delivery of nitric oxide via diazeniumdiolated metal organic framework. *Microporous and Mesoporous Materials* **2013**, *181*, 17-22.

(56) Chung, Y. G.; Camp, J.; Haranczyk, M.; Sikora, B. J.; Bury, W.; Krungleviciute, V.; Yildirim, T.; Farha, O. K.; Sholl, D. S.; Snurr, R. Q. Computation-Ready, Experimental Metal–Organic Frameworks: A Tool To Enable High-Throughput Screening of Nanoporous Crystals. *Chemistry of Materials* **2014**, *26*, 6185-6192.

(57) Supronowicz, B.; Mavrandonakis, A.; Heine, T. Interaction of Biologically Important Organic Molecules with the Unsaturated Copper Centers of the HKUST-1 Metal–Organic Framework: an Ab-Initio Study. *The Journal of Physical Chemistry C* **2015**, *119*, 3024-3032.

(58) Valenzano, L.; Civalleri, B.; Chavan, S.; Palomino, G. T.; Areán, C. O.; Bordiga, S. Computational and Experimental Studies on the Adsorption of CO, N2, and CO2 on Mg-MOF-74. *The Journal of Physical Chemistry C* **2010**, *114*, 11185-11191.

(59) Cattaneo, D.; Warrender, S. J.; Duncan, M. J.; Kelsall, C. J.; Doherty, M. K.; Whitfield, P. D.; Megson, I. L.; Morris, R. E. Tuning the nitric oxide release from CPO-27 MOFs. *RSC Advances* **2016**, *6*, 14059-14067.

(60) Al-Janabi, N.; Deng, H.; Borges, J.; Liu, X.; Garforth, A.; Siperstein, F. R.; Fan, X. A Facile Post-Synthetic Modification Method To Improve Hydrothermal Stability and CO2 Selectivity of CuBTC Metal–Organic Framework. *Industrial & Engineering Chemistry Research* **2016**, *55*, 7941-7949.

(61) McDonald, T. M.; Lee, W. R.; Mason, J. A.; Wiers, B. M.; Hong, C. S.; Long, J. R. Capture of Carbon Dioxide from Air and Flue Gas in the Alkylamine-Appended Metal–Organic Framework mmen-Mg2(dobpdc). *Journal of the American Chemical Society* **2012**, *134*, 7056-7065.

(62) Farha, O. K.; Eryazici, I.; Jeong, N. C.; Hauser, B. G.; Wilmer, C. E.; Sarjeant, A. A.; Snurr, R. Q.; Nguyen, S. T.; Yazaydın, A. Ö.; Hupp, J. T. Metal–Organic Framework Materials with Ultrahigh Surface Areas: Is the Sky the Limit? *Journal of the American Chemical Society* **2012**, *134*, 15016-15021.

(63) Murdock, C. R.; Hughes, B. C.; Lu, Z.; Jenkins, D. M. Approaches for synthesizing breathing MOFs by exploiting dimensional rigidity. *Coordination Chemistry Reviews* **2014**, *258–259*, 119-136.

(64) Alhamami, M.; Doan, H.; Cheng, C.-H. A Review on Breathing Behaviors of Metal-Organic-Frameworks (MOFs) for Gas Adsorption. *Materials* **2014**, *7*, 3198.

(65) Chen, Y.; Lykourinou, V.; Vetromile, C.; Hoang, T.; Ming, L.-J.; Larsen, R. W.; Ma, S. How Can Proteins Enter the Interior of a MOF? Investigation of Cytochrome c Translocation into a MOF Consisting of Mesoporous Cages with Microporous Windows. *Journal of the American Chemical Society* **2012**, *134*, 13188-13191.

(66) Huxford, R. C.; Rocca, J. D.; Lin, W. Metal-Organic Frameworks as Potential Drug Carriers. *Current opinion in chemical biology* **2010**, *14*, 262-268.

(67) Jia, Y.; Wei, B.; Duan, R.; Zhang, Y.; Wang, B.; Hakeem, A.; Liu, N.; Ou, X.; Xu, S.; Chen, Z.; Lou, X.; Xia, F. Imparting biomolecules to a metal-organic framework material by controlled DNA tetrahedron encapsulation. *Scientific Reports* **2014**, *4*, 5929.

(68) Morris, W.; Briley, W. E.; Auyeung, E.; Cabezas, M. D.; Mirkin, C. A. Nucleic Acid–Metal Organic Framework (MOF) Nanoparticle Conjugates. *Journal of the American Chemical Society* **2014**, *136*, 7261-7264.

(69) Liu, H. A.; Balkus, K. J. Novel Delivery System for the Bioregulatory Agent Nitric Oxide. *Chemistry of Materials* **2009**, *21*, 5032-5041.

(70) Abman, S. H.: Inhaled Nitric Oxide for the Treatment of Pulmonary Arterial Hypertension. In *Pharmacotherapy of Pulmonary Hypertension*; Humbert, M., Evgenov, V. O., Stasch, J.-P., Eds.; Springer Berlin Heidelberg: Berlin, Heidelberg, 2013; pp 257-276.

(71) Casey, D. P.; Walker, B. G.; Ranadive, S. M.; Taylor, J. L.; Joyner, M. J. Contribution of nitric oxide in the contraction-induced rapid vasodilation in young and older adults. *Journal of Applied Physiology* **2013**, *115*, 446-455.

(72) Prast, H.; Philippu, A. Nitric oxide as modulator of neuronal function. *Progress in Neurobiology* **2001**, *64*, 51-68.

(73) Raju, K.; Doulias, P.-T.; Evans, P.; Krizman, E. N.; Jackson, J. G.; Horyn, O.; Daikhin, Y.; Nissim, I.; Yudkoff, M.; Nissim, I.; Sharp, K. A.; Robinson, M. B.;

Ischiropoulos, H. Regulation of brain glutamate metabolism by nitric oxide and S-nitrosylation. *Science signaling* **2015**, *8*, ra68-ra68.

(74) Farrugia, G.; Szurszewski, J. H. Carbon Monoxide, Hydrogen Sulfide, and Nitric Oxide as Signaling Molecules in the Gastrointestinal Tract. *Gastroenterology* **2014**, *147*, 303-313.

(75) Blum, A. New oral nitric oxide-dependent medications for patients with coronary artery disease who have persistent angina pectoris. *Coronary artery disease* **2015**, *26*, 639-641.

(76) Tanaka, A.; Node, K. A novel cardioprotective mechanism of exogenous nitric oxide: inhibition of Rho-associated kinase activity. *Hypertension Research* **2015**, *38*, 461-462.

(77) Knowles, R.; Chan, M.; Hayman, M.; Armstrong, P.; Tucker, A.; Timmis, A.; Warner, T. 158 The Anti-Platelet Effectiveness of P2Y12 Receptor Blockade is Strongly Influenced by the Endothelium-Derived Mediators Nitric Oxide and Prostacyclin. *Heart* **2015**, *101*, A90-A91.

(78) Sharma, K.; Chakrapani, H. Site-directed delivery of nitric oxide to cancers. *Nitric Oxide* **2014**, *43*, 8-16.

(79) Lu, Y.; Shah, A.; Hunter, R. A.; Soto, R. J.; Schoenfisch, M. H. S-Nitrosothiol-modified nitric oxide-releasing chitosan oligosaccharides as antibacterial agents. *Acta biomaterialia* **2015**, *12*, 62-69.

(80) Worley, B. V.; Slomberg, D. L.; Schoenfisch, M. H. Nitric oxide-releasing quaternary ammonium-modified poly (amidoamine) dendrimers as dual action antibacterial agents. *Bioconjugate chemistry* **2014**, *25*, 918-927.

(81) Lu, Y.; Slomberg, D. L.; Schoenfisch, M. H. Nitric oxide-releasing chitosan oligosaccharides as antibacterial agents. *Biomaterials* **2014**, *35*, 1716-1724.

(82) Ignarro, L. J.; Buga, G. M.; Wood, K. S.; Byrns, R. E.; Chaudhuri, G. Endothelium-derived relaxing factor produced and released from artery and vein is nitric oxide. *Proceedings of the National Academy of Sciences of the United States of America* **1987**, *84*, 9265-9269.

(83) Moncada, S.; Higgs, E. A. The discovery of nitric oxide and its role in vascular biology. *British Journal of Pharmacology* **2006**, *147*, S193-S201.

(84) Miller, M. R.; Megson, I. L. Recent developments in nitric oxide donor drugs. *British Journal of Pharmacology* **2007**, *151*, 305-321.

(85) Friedman, A.; Blecher, K.; Sanchez, D.; Tuckman-Vernon, C.; Gialanella, P.; Friedman, J. M.; Martinez, L. R.; Nosanchuk, J. D. Susceptibility of Gram-positive and -negative bacteria to novel nitric oxide-releasing nanoparticle technology. *Virulence* **2011**, *2*.

(86) Frostell, C.; Fratacci, M. D.; Wain, J. C.; Jones, R.; Zapol, W. M. Inhaled nitric oxide. A selective pulmonary vasodilator reversing hypoxic pulmonary vasoconstriction. *Circulation* **1991**, *83*, 2038-2047.

(87) Keefer, L. K.; Nims, R. W.; Davies, K. M.; Wink, D. A.: "NONOates" (1-substituted diazen-1-ium-1,2-diolates) as nitric oxide donors: Convenient nitric oxide dosage forms. In *Methods in Enzymology*; Academic Press, 1996; Vol. Volume 268; pp 281-293.

(88) Drago, R. S.; Paulik, F. E. The Reaction of Nitrogen(II) Oxide with Diethylamine. *Journal of the American Chemical Society* **1960**, *82*, 96-98.

(89) Thompson, A. J.; Mander, P. K.; Brown, G. C. The NO donor DETA-NONOate reversibly activates an inward current in neurones and is not mediated by the released nitric oxide. *British Journal of Pharmacology* **2009**, *158*, 1338-1343.

(90) Majumder, S.; Sinha, S.; Siamwala, J. H.; Muley, A.; Reddy Seerapu, H.; Kolluru, G. K.; Veeriah, V.; Nagarajan, S.; Sridhara, S. R. C.; Priya, M. K.; Kuppusamy, M.; Srinivasan, S.; Konikkat, S.; Soundararajan, G.; Venkataraman, S.; Saran, U.; Chatterjee, S. A comparative study of NONOate based NO donors: Spermine NONOate is the best suited NO donor for angiogenesis. *Nitric Oxide* **2014**, *36*, 76-86.

(91) *Nanocarriers for Nitric Oxide Delivery*, 2011; Vol. 2011.

(92) Monti, M.; Solito, R.; Puccetti, L.; Pasotti, L.; Roggeri, R.; Monzani, E.; Casella, L.; Morbidelli, L. Protective Effects of Novel Metal-Nonoates on the Cellular

Components of the Vascular System. *Journal of Pharmacology and Experimental Therapeutics* **2014**, *351*, 500-509.

(93) Liang, H.; Nacharaju, P.; Friedman, A.; Friedman, J. M. Nitric oxide generating/releasing materials. *Future science OA* **2015**, *1*, 10.4155/fso.4115.4154.

(94) Riccio, D. A.; Schoenfisch, M. H. Nitric oxide release: Part I. Macromolecular scaffolds. *Chemical Society Reviews* **2012**, *41*, 3731-3741.

(95) Broniowska, K. A.; Diers, A. R.; Hogg, N. S-NITROSOGLUTATHIONE. *Biochimica et biophysica acta* **2013**, *1830*, 3173-3181.

(96) Veleeparampil, M. M.; Aravind, U. K.; Aravindakumar, C. T.: *Decomposition of S-Nitrosothiols Induced by UV and Sunlight*, 2009; Vol. 2009.

(97) Fortenberry, J. D.; Owens, M. L.; Chen, N. X.; Brown, L. A. S. S-nitrosoglutathione inhibits TNF-α-induced NFκB activation in neutrophils. *Inflammation Research* **2001**, *50*, 89-95.

(98) Sage, P. R.; de la Lande, I. S.; Stafford, I.; Bennett, C. L.; Phillipov, G.; Stubberfield, J.; Horowitz, J. D. Nitroglycerin Tolerance in Human Vessels. *Evidence for Impaired Nitroglycerin Bioconversion* **2000**, *102*, 2810-2815.

(99) Hottinger, D. G.; Beebe, D. S.; Kozhimannil, T.; Prielipp, R. C.; Belani, K. G. Sodium nitroprusside in 2014: A clinical concepts review. *Journal of Anaesthesiology, Clinical Pharmacology* **2014**, *30*, 462-471.

(100) Borhade N, P. A., Halder S, Karwa M, Dhiman M, Pamidiboina V, Gund M, Deshattiwar JJ, Mali SV, Deshmukh NJ, Senthilkumar SP, Gaikwad P, Tipparam SG, Mudgal J, Dutta MC, Burhan AU, Thakre G, Sharma A, Deshpande S, Desai DC, Dubash NP, Jain AK, Sharma S, Nemmani KV, Satyam A. NO-NSAIDs. Part 3: nitric oxide-releasing prodrugs of non-steroidal anti-inflammatory drugs. *Chem Pharm Bull (Tokyo)* **2012**, *60*, 465-481.

(101) Koshland, D. The molecule of the year. *Science* **1992**, *258*, 1861-1861.

(102) Amedea B. Seabra, P. D. M., Larissa B. de Paula,; Durán, N. New Strategy for Controlled Release of Nitric Oxide. *Journal of Nano Research* **2012**, *20*, 61-67.

(103) Jo, Y. S.; van der Vlies, A. J.; Gantz, J.; Thacher, T. N.; Antonijevic, S.; Cavadini, S.; Demurtas, D.; Stergiopulos, N.; Hubbell, J. A. Micelles for Delivery of Nitric Oxide. *Journal of the American Chemical Society* **2009**, *131*, 14413-14418.

(104) Taladriz-Blanco, P.; Pastoriza-Santos, V.; Pérez-Juste, J.; Hervés, P. Controllable Nitric Oxide Release in the Presence of Gold Nanoparticles. *Langmuir* **2013**, *29*, 8061-8069.

(105) Bloch, E. D.; Queen, W. L.; Chavan, S.; Wheatley, P. S.; Zadrozny, J. M.; Morris, R.; Brown, C. M.; Lamberti, C.; Bordiga, S.; Long, J. R. Gradual Release of Strongly Bound Nitric Oxide from Fe2(NO)2(dobdc). *Journal of the American Chemical Society* **2015**, *137*, 3466-3469.

(106) Horcajada, P.; Gref, R.; Baati, T.; Allan, P. K.; Maurin, G.; Couvreur, P.; Férey, G.; Morris, R. E.; Serre, C. Metal–Organic Frameworks in Biomedicine. *Chemical Reviews* **2012**, *112*, 1232-1268.

(107) Kim, J.; Saravanakumar, G.; Choi, H. W.; Park, D.; Kim, W. J. A platform for nitric oxide delivery. *Journal of Materials Chemistry B* **2014**, *2*, 341-356.

(108) Xiao, B.; Wheatley, P. S.; Morris, R. E.: The adsorption, storage and release of nitric oxide using ion exchanged zeolites. In *Studies in Surface Science and Catalysis*; Ruren Xu, Z. G. J. C., Wenfu, Y., Eds.; Elsevier, 2007; Vol. Volume 170; pp 902-909.

(109) Kawase, J.; Nakae, A.; Tsuji, K. Determination of zeolite-a in detergent powders as acid-soluble aluminum by high-performance liquid chromatography with post-column derivatization. *Analytica Chimica Acta* **1981**, *131*, 213-222.

(110) Boës, A.-K.; Xiao, B.; Megson, I. L.; Morris, R. E. Simultaneous Gas Storage and Catalytic Gas Production Using Zeolites—A New Concept for Extending Lifetime Gas Delivery. *Topics in Catalysis* **2009**, *52*, 35-41.

(111) McKinlay, A. C.; Allan, P. K.; Renouf, C. L.; Duncan, M. J.; Wheatley, P. S.; Warrender, S. J.; Dawson, D.; Ashbrook, S. E.; Gil, B.; Marszalek, B.; Düren, T.; Williams, J. J.; Charrier, C.; Mercer, D. K.; Teat, S. J.; Morris, R. E. Multirate delivery of multiple therapeutic agents from metal-organic frameworks. *APL Mater.* **2014**, *2*, 124108.

(112) Sun, C.-Y.; Qin, C.; Wang, X.-L.; Su, Z.-M. Metal-organic frameworks as potential drug delivery systems. *Expert opinion on drug delivery* **2013**, *10*, 89-101.

(113) Harding, J. L.; Reynolds, M. M. Composite materials with embedded metal organic framework catalysts for nitric oxide release from bioavailable S-nitrosothiols. *Journal of Materials Chemistry B* **2014**, *2*, 2530-2536.

(114) Matsuyama, K.; Hayashi, N.; Yokomizo, M.; Kato, T.; Ohara, K.; Okuyama, T. Supercritical carbon dioxide-assisted drug loading and release from biocompatible porous metal–organic frameworks. *Journal of Materials Chemistry B* **2014**, *2*, 7551-7558.

(115) Cattaneo, D.; Warrender, S. J.; Duncan, M. J.; Castledine, R.; Parkinson, N.; Haley, I.; Morris, R. E. Water based scale-up of CPO-27 synthesis for nitric oxide delivery. *Dalton Transactions* **2016**, *45*, 618-629.

(116) Peikert, K.; McCormick, L. J.; Cattaneo, D.; Duncan, M. J.; Hoffmann, F.; Khan, A. H.; Bertmer, M.; Morris, R. E.; Fröba, M. Tuning the nitric oxide release behavior of amino functionalized HKUST-1. *Microporous and Mesoporous Materials* **2015**, *216*, 118-126.

(117) McKinlay, A. C.; Eubank, J. F.; Wuttke, S.; Xiao, B.; Wheatley, P. S.; Bazin, P.; Lavalley, J. C.; Daturi, M.; Vimont, A.; De Weireld, G.; Horcajada, P.; Serre, C.; Morris, R. E. Nitric Oxide Adsorption and Delivery in Flexible MIL-88(Fe) Metal–Organic Frameworks. *Chemistry of Materials* **2013**, *25*, 1592-1599.

(118) Harding, J. L.; Reynolds, M. M. Metal Organic Frameworks as Nitric Oxide Catalysts. *Journal of the American Chemical Society* **2012**, *134*, 3330-3333.

(119) Cai, W.; Wang, X.; Elshahawi, S. I.; Ponomareva, L. V.; Liu, X.; McErlean, M. R.; Cui, Z.; Arlinghaus, A. L.; Thorson, J. S.; Van Lanen, S. G. Antibacterial and Cytotoxic Actinomycins Y6–Y9 and Zp from Streptomyces sp. Strain Gö-GS12. *Journal of Natural Products* **2016**.

(120) Walton, K.; Berry, J. P. Indole Alkaloids of the Stigonematales (Cyanophyta): Chemical Diversity, Biosynthesis and Biological Activity. *Marine Drugs* **2016**, *14*, 73.

(121) Dias, D. A.; Urban, S.; Roessner, U. A Historical Overview of Natural Products in Drug Discovery. *Metabolites* **2012**, *2*, 303.

(122) Ayala, C. E.; Dange, N. S.; Fronczek, F. R.; Kartika, R. Brønsted Acid Catalyzed α' - Functionalization of Silylenol Ethers with Indoles. *Angewandte Chemie* **2015**, *127*, 4724-4728.

CHAPTER 2. QUANTUM CALCULATIONS OF METAL ORGANIC FRAMEWORKS

2.1 Introduction of Quantum Mechanics

Most of the tangible world around us can be defined through principles of classical mechanics. When chemist and physicist seek to understand the subatomic properties and phenomenon of a system, a new set of laws must be employed to understand these processes. To describe interactions and motions of atoms and subatomic particles, the electronic structure of molecules must be treated through the use of quantum mechanics. In quantum mechanics the total energy operator of a system is known the Hamiltonian ($\hat{H}$); analogous to classical mechanics, the total energy of the system is equal to the kinetic ($\hat{T}$) and potential energies ($\hat{V}$) operators as follows:

$$\hat{H} = \hat{T} + \hat{V} \qquad \text{(Equation 2.1)}$$

The kinetic and potential energy operators can be written as

$$\hat{T} = -\frac{\hbar^2}{2m}\frac{d^2}{dx^2} \qquad \text{(Equation 2.2)}$$

$\hbar$ is the reduced Planck's constant, m is the mass of the electron, x is the position.

$$\hat{V} = V(x) \qquad \text{(Equation 2.3)}$$

The potential energy operator can be written to equal the potential energy (V) of the system as a function of position. From Equations 2.2 and 2.3, the Hamiltonian takes the form of Equation 2.4:

$$\hat{H} = -\frac{\hbar^2}{2m}\frac{d^2}{dx^2} + V(x) \qquad \text{(Equation 2.4)}$$

The molecular Hamiltonian can be expressed through five terms associated with the nuclear and electronic kinetic energies in addition to the potential energies as shown below in Equation 2.5:

$$\hat{H} = -\frac{\hbar^2}{2m}\sum_i \nabla_i^2 - \sum_A \frac{\hbar^2}{2M_A}\nabla_A^2 - \sum_{A,i}\frac{Z_A e^2}{4\pi\varepsilon_0 r_{Ai}} + \sum_{A>B}\frac{Z_A Z_B e^2}{4\pi\varepsilon_0 R_{AB}} + \sum_{i>j}\frac{e^2}{4\pi\varepsilon_0 r_{ij}}$$

(Equation 2.5)

∇ is the LaPlacian operator, M_A is the mass of the nuclei, Z is the charge of the nuclei, e is the charge of the electron, ε_0 is the electric constant (or permittivity of a vacuum), r_{Ai} is the distance between nuclei and electron and R_{AB} is the distance between nuclei.

Equation 2.5 can also be depicted as shown in Equation 2.6:

$$\hat{H} = \hat{T}_N(R) + \hat{T}_e(r) + \hat{V}_{eN}(r,R) + \hat{V}_{NN}(R) + \hat{V}_{ee}(r)$$

(Equation 2.6)

where $\hat{T}_N$ and $\hat{T}_e$ represents the kinetic energy operator for both the nuclei and electrons, respectively. The potential energy operators $\hat{V}_{eN}$, $\hat{V}_{NN}$ and $\hat{V}_{ee}$ correspond to the Coulombic interactions for the electron-nuclear, nuclear-nuclear, and electron-electron terms, respectively.

Akin to Newton's laws in classical mechanics, the Schrödinger equation serves the purpose of predicting future behaviors of a quantum system. When probing systems quantum mechanically, solving the Schrödinger equation is critical. While this equation provides the necessary information of a system, including electronic energy and electron density, in most cases it is not feasible to do so as a result of the many-body problem. *Ab initio* calculations are computational methods employed to investigate the quantum mechanics of a system through solving the Schrödinger equation.

Despite difficulties with solving this equation, the implementation of approximations allows for the electronic Schrödinger equation to be solved in many-electron systems. One such approximation bases its principles on the subatomic composition of an atom, which includes the proton and neutron-containing nucleus in addition to a surrounding electron cloud. The small size and high speeds of the orbiting electrons in comparison to the massive, slow moving nucleus, permits the nucleus to be treated as stationary. Due to the stationary state of the nucleus, the relatively massive $\hat{V}_{NN}$ term can be neglected and the resultant equation defines the electronic Hamiltonian, $\hat{H}_{el}$.

$$\hat{H}_{el} = \hat{T}_e(r) + \hat{V}_{eN}(r,R) + \hat{V}_{ee}(r) \qquad \text{(Equation 2.7)}$$

Following this transformation the clamped-nuclei Schrodinger's equation is

$$\hat{H}_{el}\,\Psi(r;R) = E_{el}\Psi(r;R) \qquad \text{(Equation 2.8)}$$

where r represents the electronic distance, R is the nuclear separation, E_{el} is the electronic energy and the wavefunction (Ψ) is defined as

$$\Psi_i(r;R) = \chi_i\phi_i \qquad \text{(Equation 2.9)}$$

From this we have defined the Born-Oppenheimer approximation allowing us to decouple motions of electronic, ϕ_i and nuclear terms, χ_i. While this approximation allows one to solve the electronic Schrödinger equation, it does not solve issues associated with the electronic Hamiltonian due to electron-electron repulsions.

Bypassing this issue requires the implementation of assumptions leading to the independent particle model to look at electrons as independent of one another, thus eliminating the correlation behavior of electrons. One crude level of theory negating the effects of electron-electron repulsion while obeying the fermion requirements of antisymmetry is the Hartree-Fock method. To account for the interactions between an electron and its neighbors, the mean field theory treats the electric field of other electrons as an averaged value. The Hartree-Fock level of theory assumes that a single Slater determinant is capable of approximating the exact N-body wave function of a system. A fundamental flaw with the Hartree-Fock

method is the neglect of electron correlation; as such, alternative levels of theory have been developed to improve upon Hartree-Fock methods. One such method is the density functional theory (DFT), which fully accounts for electron correlation. Unlike Hartree-Fock, which treats electron correlation as an average, DFT is able to approximate these values.

The DFT level of theory treats the total energy of a system as a functional of electron density, which is the probability of locating an electron at a specific location. The electron density functional is a function of three coordinates as opposed to the 3N coordinates of N electrons and thus requires less computational resource. Emphasis must be placed on the appropriate selection of functionals based on the system of study. The utilization of hybrid functions allows the incorporation of gradient correction that begins with local-density approximations in addition to the integration of empirically fitted Hartree-Fock exchange. B3LYP is a commonly used hybrid function known for generating reasonable results for equilibrium geometries. After defining the components associated with choosing a level of theory, an accurate depiction of the atomic orbitals must be carried out.

Work contained herein employs Gaussian type orbitals (GTOs) to represent atomic orbitals due to the Gaussian Product Theorem which states that the product of GTOs centered on two different atoms equals the finite sum of Gaussians that are centered on a point along the axis that connects them.[2] Basis sets using this method display a speedup of up to 5 orders of magnitude faster than that of Slater orbitals.[3] The polarization of an atomic orbital results in its distortion upon the approach of

an atom. Polarization functions must be added into the calculations to account for this behavior within a system. In addition, inclusion of diffuse functions may be used to describe charged systems with loosely bound electrons held far from the nucleus.

The quantum mechanical methods discussed are used to probe MOFs for the chemical storage, delivery and release of nitric oxide precursors to obtain the rudimentary interactions responsible for the ultimate release of nitric oxide. It is important to first consider the accurate depiction of the HKUST-1 framework including its charge and ability to breathe, as it has been reported that the approach of guest molecules can cause changes to the volume of these materials.[4] Zhao et al constructed an accurate force field for HKUST-1 capable of capturing the flexibility exhibited by these materials. To define this force field, a mix of parameters obtained from DFT calculations and the DREIDING force field was used.[5]

DFT calculations performed by Zhao et al. focused on the parameterization of angle bending parameters around the copper ions within HKUST-1.[5] In doing so, a small cluster was employed to represent the larger framework, consisting of the metal centers each sharing coordination to four carboxylates and their benzene constituent. Execution of this force field in MD simulations resulted in reported bond lengths and angles that are in good agreement with experimental data. Furthermore, adsorption studies of CO_2 utilizing the flexible framework for HKUST-1 are in further agreement than previously used rigid force fields.[5,6]

Although parameterized force fields accurately captured the innate ability of MOFs to effectively “breathe” by changing volume, the generalized nature of the

Dreiding force field is not capable of sufficiently defining key interactions between these nanomaterials and the RSNO guest molecules of the system proposed herein. The lack of proper parameters arises from coordination bonds formed by Cu(I) with sulfur and oxygen atoms of the RSNOs in addition to the oxygen of ethanol solvent molecules. While *ab initio* (quantum mechanics (QM)) calculations of this system would be ideal, this method is quite computationally costly due to the size and time needed to access relative time scales of the system. To overcome this dilemma, we perform *ab initio* (in this case electronic structure) analyses on appropriate sub-systems that are computationally feasible and utilize the data obtained in the construction of models that can be used to explore longer length and time scales.

Development of these models further allows probing into interactions that are critical in understanding how RSNO approaches the copper center and how changes in energy are associated with these events. Further discussion will focus on parameters obtained through DFT calculations as a result of its ability to integrate accuracy with comparative computational efficiency; subsequent parameters obtained from DREIDING will be discussed in Chapter 3.

2.2 Computational Methods

Gas phase calculations on clusters representative of the HKUST-1 framework were performed for the following reasons: 1) to determine the role of the thiol molecule. 2) The elucidation of the relevant reaction pathway for the approach of RSNO to the copper center. 3) To define parameters for the guest interactions with

the active catalyst. In experimental work performed by Harding et al. it was reported that a thiol was necessary for the release of nitric oxide from the RSNO precursor in the presence of the MOF environment.[7] The role of the thiol has been suggested in the reduction of Cu(II) to Cu(I), the active catalyst. To further probe the role of the thiol, electronic structure calculations were performed on CH_3SH, Cu(II), and an explicit ethanol molecule in an implicit ethanol solvent using the polarizable continuum model (PCM). The oxidation state of the Cu(II) ion gives the system a charge of +2 and multiplicity of 2. Further investigation using the Natural Bond Order (NBO) analysis[8] is carried out to probe the orbital occupancy of Cu(II) in the presence of the thiol.

Elucidation of the reaction pathway was probed through electronic structure calculations where geometry optimizations are performed to find the reactants, products and their relevant transition state. The transition state is verified through a synchronous transit-guided quasi-newton method[9] and confirmed to correspond to the reported reactants and products through the intrinsic reaction coordinate (IRC) calculations.[10] The electrostatic behavior of the MOF is represented through point charges obtained using the CHELPG method, which fits the charge to the electrostatic potential of the molecule and is performed on the representative cluster; partial charges of all remaining atoms are also performed using the CHELPG method.[11] CHELPG is a robust method of providing accurate partial charges independent of the level of theory and basis set used.

2.3 Results & Discussion

To determine the role of the thiol molecule within the system, electronic structure calculations were performed. Figure 2.1 shows results from the optimization of a thiol in the presence of Cu(II) and an explicit ethanol molecule within a simulated solvent (PCM, epsilon=2.3741). The geometry optimization of these molecules resulted in the transfer of a proton from the thiol to form a protonated ethanol molecule, CH_3S^- and the Cu(II) ion to form the $[Cu^{2+}\text{-}CH_3S^-]^+$ complex. Previous studies have considered the copper (I) oxidation state to be the catalytically active species for the reaction thus labeling this proton transfer as one possible mechanism for the generation of the catalytic species. To further validate these findings, the reduction of the copper center was scrutinized through natural bond order (NBO) analysis. Furthermore, NBO analysis shows the complexed copper ion has a full d-orbital ($3d^{10}$), further suggesting that the role of the thiol is to reduce copper (II) to the Cu(I) oxidation state.

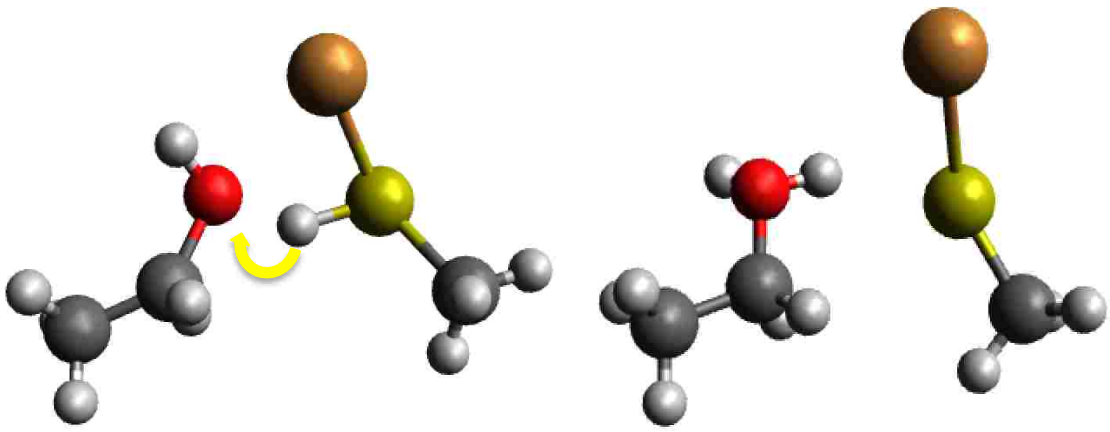

Figure 2.1. Shows the (left) pre-optimized structure and (right) optimized structure of an explicit ethanol molecule, copper ion and thiol. Electronic structure calculations show the transfer of a proton from the thiol to produce a protonated ethanol and $[Cu^{2+}\text{-}RS^-]^+$ complex.

As NBO analysis verifies the addition of an electron into the 3d orbital for the reduced copper ion, further validation that the change in charge occurs specifically at the metal center was needed. Results reported from Zhao et al. show the partial charge at each copper center within the MOF is 1.09 e.[5] To represent the catalytic copper centers in the +1 oxidation state, the 1.09 e charge obtained by Zhao et al. was reduced to 0.09 e, a reduction in charge of -1. To justify the utilization of this charge, CHELPG calculations were performed on a highly negative cluster (-6 e), neutralized through 6 symmetrically placed sodium ions (Figure 2.2) used to further verify that changes in charge occur directly at the copper center with little effect on

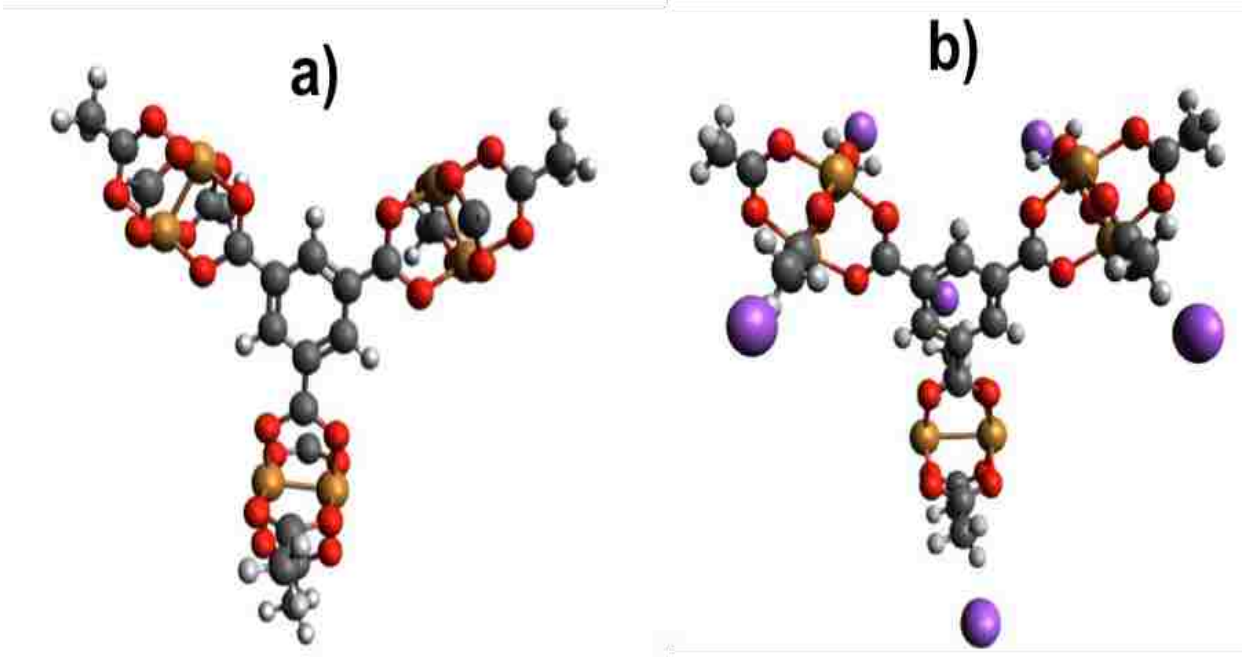

Figure 2.2. (a) Representative cluster with Cu(II) used to determine charges using the CHELPG method in work by Yang et al.[1]; (b) this cluster contains copper in the +1 oxidation state and yields a negatively charged cluster that is capped with 6 sodium ions (purple). Cu atoms are in orange, carbon atoms in grey, hydrogen atoms in white and oxygen atoms in red.

the surrounding atoms. Results of this charge analysis shows a reduction in charge at the copper center of ~0.06 e, nearly a reduction of one from the 1.09 e charge reported by Zhao et al.[5]

Through geometry optimizations of reactants CH_3SNO and Cu(I), two isomers are revealed as the Cu(I) ion forms a bond through the sulfur or the oxygen atom (Figure 2.3). The most energetically favorable isomer is that of the Cu^+ species bound through the sulfur atom of the RSNO, as such the reaction coordinate is taken

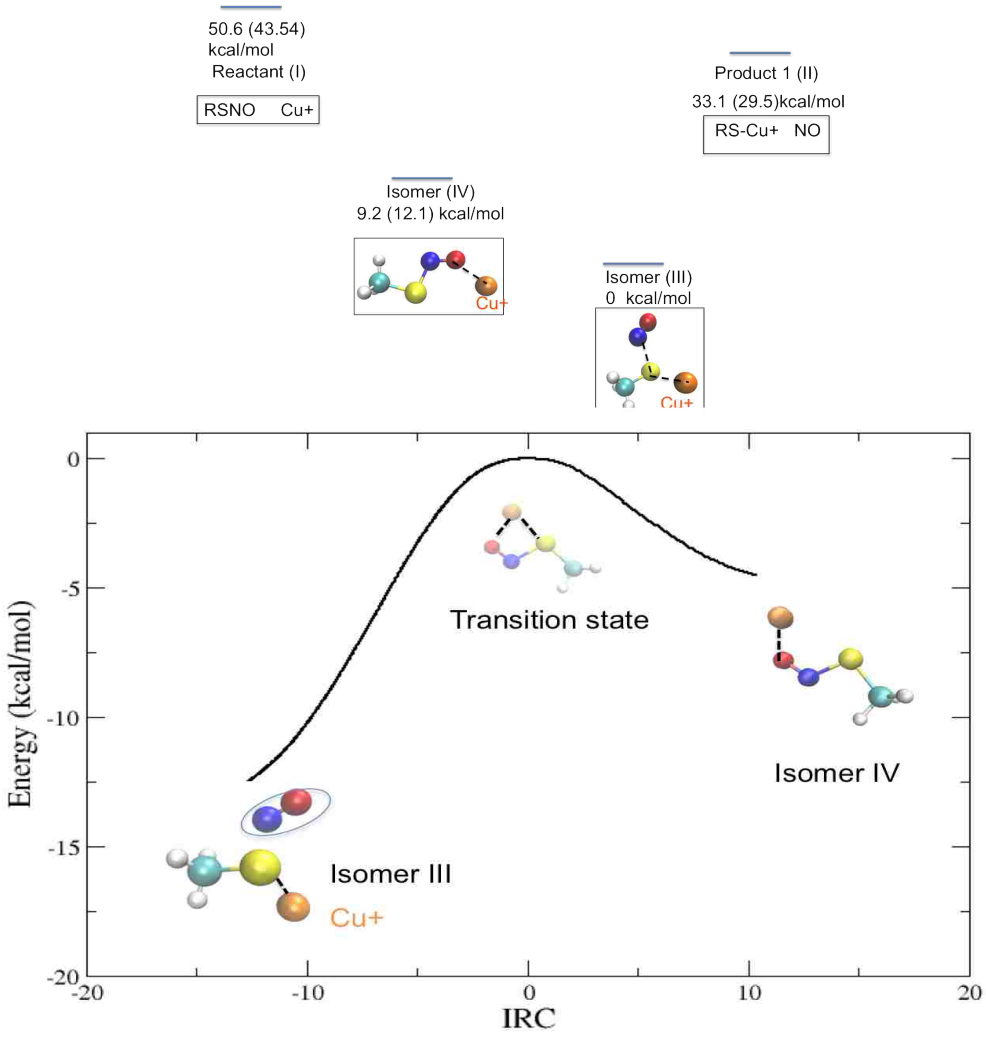

Figure 2.3. The minimum energy path shows the conversion of isomer IV to isomer III through the transition state.

as the copper-sulfur distance for this study. Coordination of Cu(I) to sulfur results in a bond length of approximately 2.25 Å (Figure 2.4b) which agrees well with experimentally reported values ranging from 2.1-2.3 Å.[12] Upon formation of this bond, an elongation of the sulfur-nitrogen bond with respect to the optimized free RSNO moiety is observed while a simultaneous decrease in the nitrogen-oxygen bond is observed. The adjustment in bond length for these atoms implies that the release of nitric oxide is imminent, further validating the $r_{Cu\text{-}S}$ reaction pathway.

The second lowest isomer involves the coordination of Cu(I) to oxygen but shows a decrease in sulfur-nitrogen bond length. The approach of the CH_3SNO to the copper ion initially shows a smaller distance between Cu(I)-O; however, the

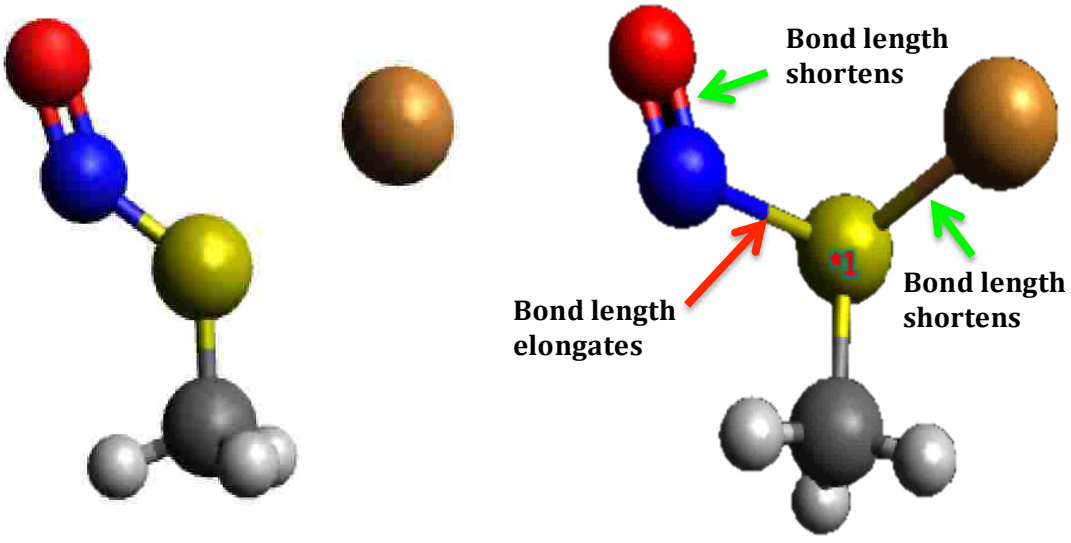

Figure 2.4. (left) pre-optimized structure of CH_3SNO approximately 3 A from the copper ion (right) optimized structure of CH_3SNO results in an elongation of the S-N bond while a simultaneous decrease in bond length for N-O.

orientation of CH_3SNO turns towards a configuration where sulfur is nearest to the copper ion. Further work shows the conversion of this isomer (copper-oxygen) to the $[Cu\text{-}CH_3S]^+$ complex and nitric oxide product through a transition state involving the coordination of both sulfur and oxygen to the copper ion. The obtained transition state was confirmed using a frequency calculation that showed only one imaginary frequency and connected the reactant and products through IRC calculations. It is shown that the catalytic release of nitric oxide can occur in two manners, either through coordination of an RSNO directly to Cu(I) or mediated through a $[Cu^{2+}\text{-}RS^-]^+$ complex. The release of nitric oxide was investigated in both starting catalyst and shows the approach of an initial CH_3SNO towards Cu(I) results in the release of nitric oxide upon the formation of a Cu-S coordination bond.

Furthermore, approach of a second CH_3SNO to the same copper center results in the release of an additional molecule of nitric oxide and ultimately the formation of a disulfide bond to generate the organic by-product RSSR. It is noteworthy to mention that although the release of nitric oxide from two RSNOs is necessary for the formation of the RSSR by-product and completion of the catalytic cycle, nitric oxide can be released by the coordination of one RSNO to the copper center. The coordination of CH_3SNO to $[Cu\text{-}CH_3S^-]^+$ as the starting complex also results in the release of nitric oxide and leads to a disulfide by-product (Figure 2.5). This demonstrates that regardless of which starting catalyst is used, nitric oxide release occurs in an identical manner and ultimately generates a disulfide by-product.

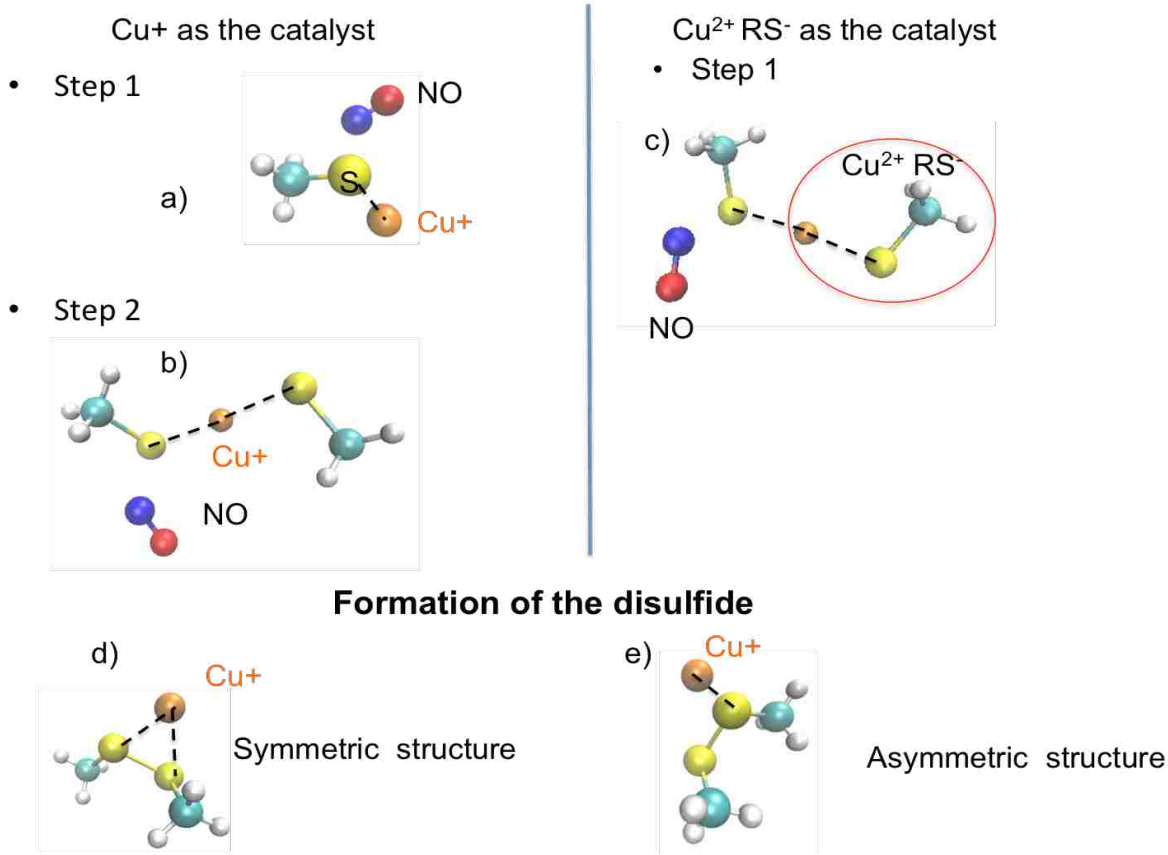

Figure 2.5. Reaction steps show that either Cu(I) or $[Cu^{2+}\text{-}RS^{-}]^{+}$ can interact with RSNO and generate nitric oxide and RSSR by-product.

Two distinct structures are identified for the formation of a disulfide bond in which the sulfur atoms are symmetrically and asymmetrically coordinated to the copper ion. The asymmetric structure is shown to be more stable by 2.8kcal/mol. Electronic structure calculations in this work were performed using the Gaussian09[13] suite at the DFT level of theory[14], using the M06 functional[15] (with the exception of CHELPG calculations for consistency with Zhong) and a mixed basis set. The mixed basis set consist of the LANLDZ for copper and 6-311G+(d,p) for all remaining atoms. It is also important to note that cases in which atoms contain an unpaired spin unrestricted methods were used (i.e. Cu^{2+} and NO).

2.3.1 Force Field Development. The in-house force field used in this work was developed by fitting the model energies to the interaction energies obtained from *ab initio* calculations. Listed below is an outline of the steps used to determine fitted van der Waals interactions between the active catalyst, Cu(I) and CH_3SNO (C, S, N, O) as well as ethanol (CH_2, O, H)[16]. (1) Perform relaxed *ab initio* potential energy scans for the purpose of obtaining the interaction energies. The above-mentioned scans were performed as a function of the Cu-S and Cu-O distances, where the sulfur and oxygen are located on the s-nitroso end of the molecule. (2) Point charges were obtained through the CHELPG (B3LYP functional) method[11] and are outlined in Figure 2.6 (3) The obtained *ab initio* interaction energies for these calculations are used to fit the model and obtain the parameters in Table 2.1, using the genetic algorithm and the least squares method (Figure 2.7).

This algorithm seeks to optimize the parameters used in a fashion that mimics that of natural selection, through several steps including representation, evaluation, selection and recombination. Initial selection is done randomly and evaluated or tested against a set of criteria. The genetic algorithm sets out to maximize $1/\chi^2$ to assess to goodness of the fit (χ^2) by the equation below:

$$\chi^2 = \sum_{i=1}^{N} \left(E_{\mathrm{mod},i} - E_{ab-inito,i} \right)^2 \qquad \text{(Equation 2.10)}$$

in which the *ab initio* interaction energy is $E_{ab-inito,i}$ and the interaction energy of the model is $E_{\mathrm{mod},i}$. Likewise, potential energy scans were also performed in a similar manner to obtain interaction energies for Cu(I)-OEtH as a function of the Cu-O

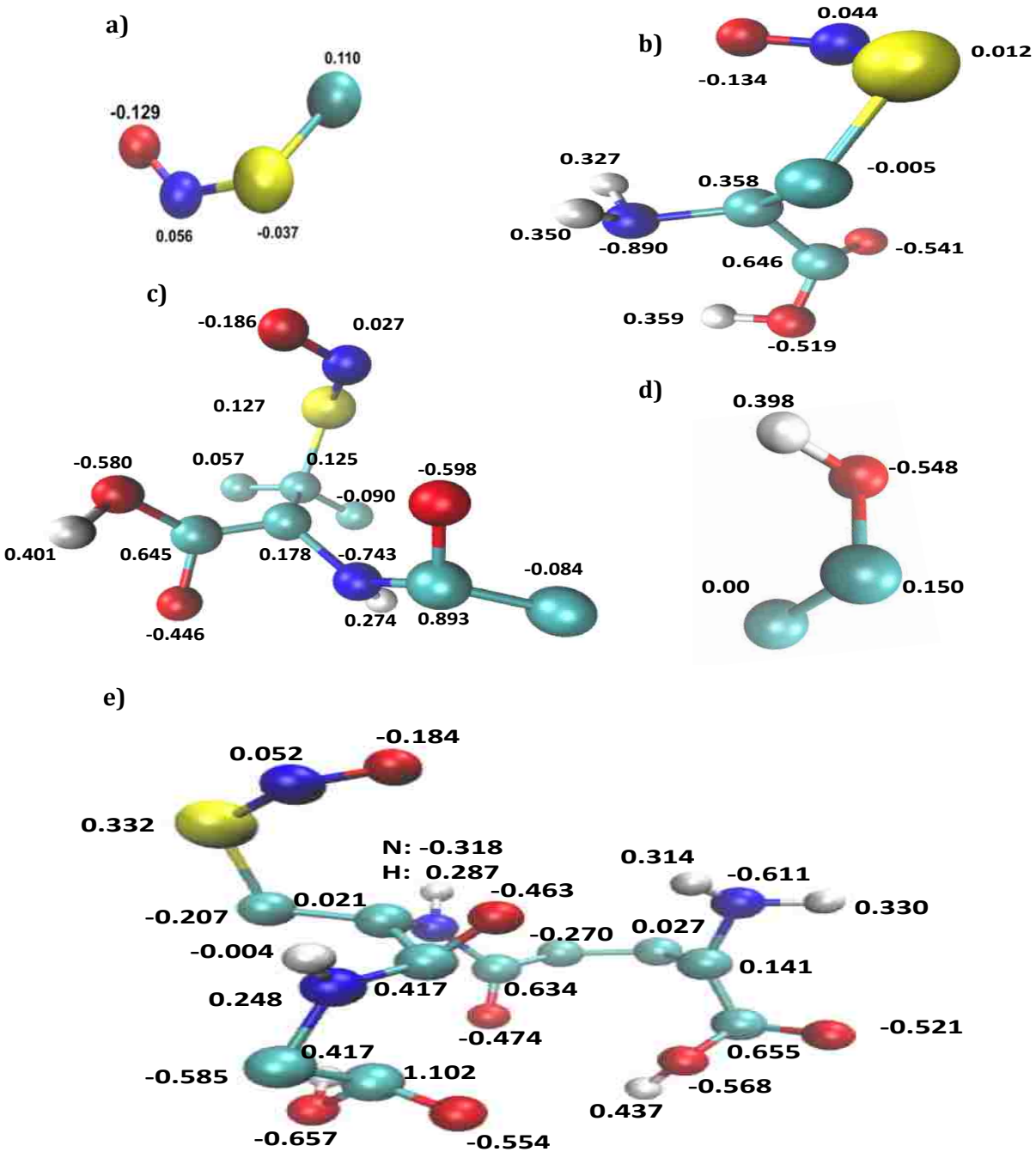

Figure 2.6. CHELPG derived charges for (a) CH_3SNO (b) CysNO (c) SNAP (d) ethanol (e) GSNO

distance for O, H and CH_2. The energy parameters obtained from the genetic algorithm at various points (distances) are plotted for both copper with sulfur and oxygen in Figure 2.7; these parameters are also plotted for copper with ethanol. These plots confirm that our model agrees with that of the *ab initio* derived energies. The resultant A and B parameters can be found for CH_3SNO and ethanol in Table 2.1.

Table 2.1. A list of the van der Waals parameters for the non-bonded interactions. All remaining parameters were obtained from the Dreiding force field. Units: A) kJ mol^{-1} nm^{12} B) kJ mol^{-1} nm^6

	A	**B**
CH_3SNO		
Cu-CH_3	3.5×10^{-4}	3.1×10^{-1}
Cu-S	4.9×10^{-7}	1.7×10^{-2}
Cu-N	3.2×10^{-5}	1.1×10^{-1}
Cu-O	2.1×10^{-9}	5.2×10^{-1}
EtOH		
Cu-CH_2	1.0×10^{-4}	1.9×10^{-1}
Cu-O	1.5×10^{-9}	1.6×10^{-4}
Cu-H	1.5×10^{-6}	1.7×10^{-2}

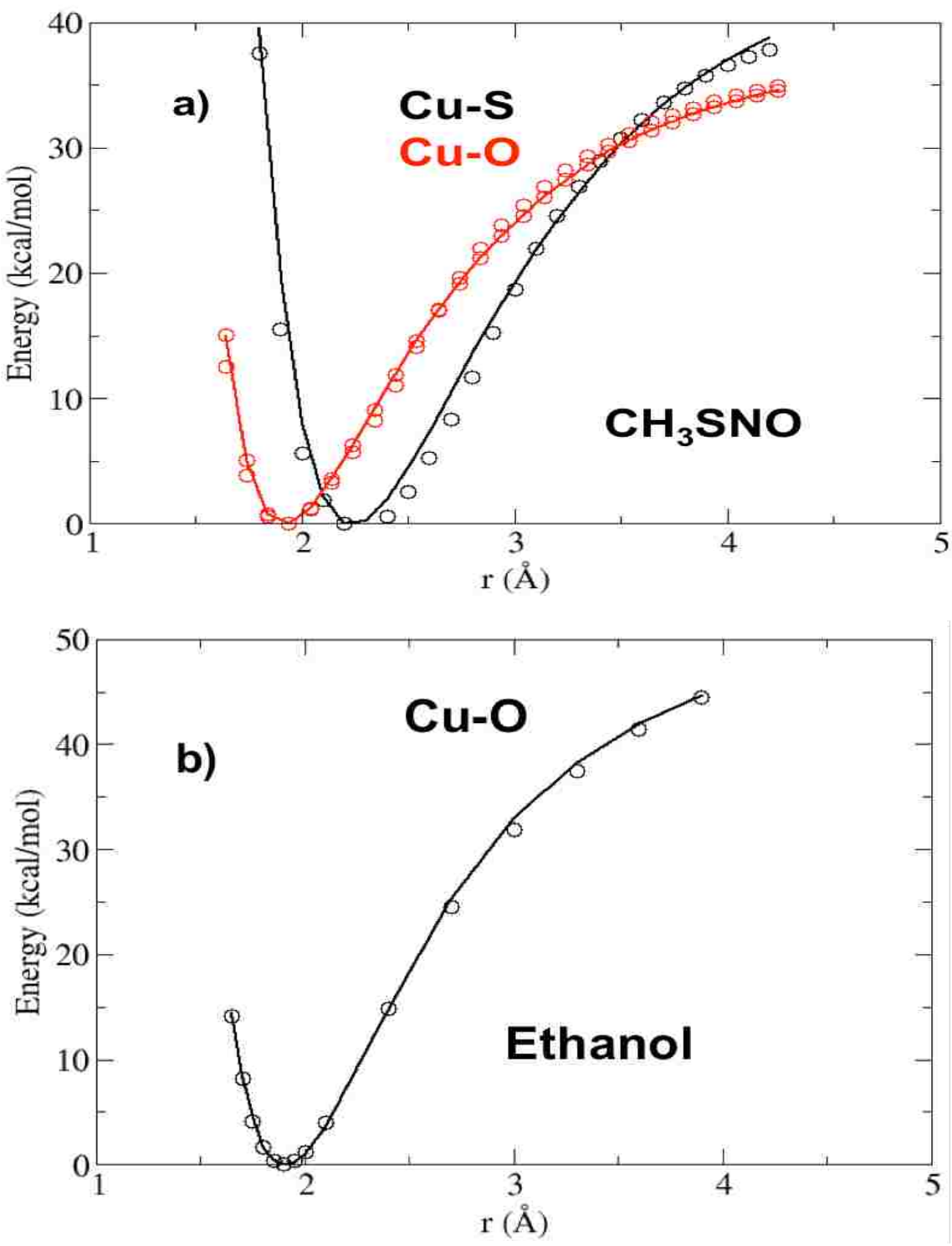

Figure 2.7. Energy scans from *ab initio* calculations (circles) are compared to the model (solid line) for the (top) Cu(I) and CH_3SNO and (bottom) Cu(I) and an ethanol molecule to fit the van der Waals interactions for Cu(I) with both CH_3SNO and ethanol.

2.4 Expansion of the MOF Library: MOF-143

For the purpose of probing how changes in the MOFs organic linker size are capable of affecting the release rate of nitric oxide, an expanded MOF similar to that of HKUST-1 is desired. MOF-143 contains an expanded tribenzoate linker as opposed to the 1,3,5-benzene carboxylate (trimesic acid) linker used in HKUST-1; the resulting pore diameter for MOF-143 is 20.4 A, approximately two times larger than HKUST-1. In order to represent the flexibility of MOF-143, parameters from HKUST-1 are extrapolated onto MOF-143 and used in subsequent MD simulations. Partial charges for MOF-143 are also obtained through a representative cluster of MOF-143 where the CHELPG method is utilized on a neutral cluster (Table 2.2). The charge for Cu(II) was taken to be 1.08 e from CHELPG calculations, nearly identical to the 1.09 e charge exhibited on Cu(II) within the HKUST-1 framework.

Table 2.2. Partial charges on the MOF-143 system. C(1) refers to the oxalate carbon, C(2) to the carbon connected to the oxalate and C(3) to the remaining carbon atoms.

Atom Type	Charge (e)
Cu	1.080
O	-0.731
C(1)	0.866
C(2)	-0.119
C(3)	-0.052
H	0.110

To further demonstrate that the loss of charge occurs at the metal center, the cluster was also probed with copper in the +1 oxidation state (Figure 2.8).

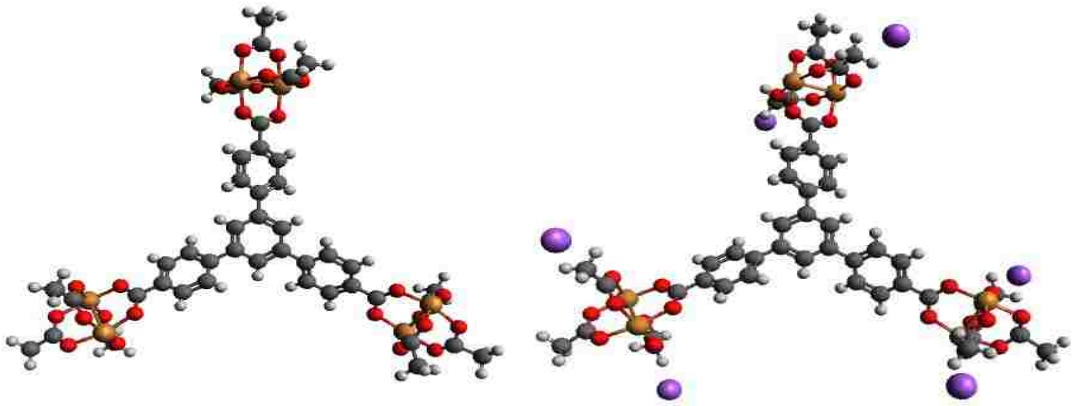

Figure 2.8. (left) MOF-143 cluster with copper ions in the +2 oxidation state, yielding a neutral cluster (right) MOF-143 cluster contains copper with a +1 oxidation state resulting in a highly negative (-6 e) system, neutralization of this fragment occurs through capping with 6 sodium ions.

This system results in a highly charged system (-6 e) that is neutralized with the addition of 6 sodium ions (Figure 2.8). Results from this show that the charge at the metal centers is reduced from 1.08 e to -0.007 e, nearly a reduction in charge of -1. The associated charge trends for MOF-143 are in good agreement with that of the HKUST-1 calculations and further validates the choice of charge at the metal center for HKUST-1.

2.5 References

(1) Yang, Q.; Zhong, C. Molecular Simulation of Carbon Dioxide/Methane/Hydrogen Mixture Adsorption in Metal–Organic Frameworks. *The Journal of Physical Chemistry B* **2006**, *110*, 17776-17783.

(2) Friesner, R. A. Ab initio quantum chemistry: Methodology and applications. *Proceedings of the National Academy of Sciences of the United States of America* **2005**, *102*, 6648-6653.

(3) Helgaker, T.; Taylor, P. R. Gaussian basis sets and molecular integrals. *Modern Electronic Structure* **1995**.

(4) Liu, L. Z. Q. Y. Q. M. C. Z. J. M. D. A force field for dynamic Cu-BTC metal-organic framework. *J Mol Model* **2010**, *17*, 227-234.

(5) Zhao, L.; Yang, Q.; Ma, Q.; Zhong, C.; Mi, J.; Liu, D. A force field for dynamic Cu-BTC metal-organic framework. *Journal of Molecular Modeling* **2011**, *17*, 227-234.

(6) Harding, J. L.; Reynolds, M. M. Metal Organic Frameworks as Nitric Oxide Catalysts. *Journal of the American Chemical Society* **2012**, *134*, 3330-3333.

(7) Weinhold, F. Natural bond orbital analysis: A critical overview of relationships to alternative bonding perspectives. *Journal of Computational Chemistry* **2012**, *33*, 2363-2379.

(8) Peng, C.; Bernhard Schlegel, H. Combining Synchronous Transit and Quasi-Newton Methods to Find Transition States. *Israel Journal of Chemistry* **1993**, *33*, 449-454.

(9) Maeda, S.; Harabuchi, Y.; Ono, Y.; Taketsugu, T.; Morokuma, K. Intrinsic reaction coordinate: Calculation, bifurcation, and automated search. *International Journal of Quantum Chemistry* **2015**, *115*, 258-269.

(10) Determining Atomic Charges using the CHELPG Scheme. (accessed March 10 2014).

(11) Zhang, S.; Melzer, M. M.; Sen, S. N.; Çelebi-Ölçüm, N.; Warren, T. H. A motif for reversible nitric oxide interactions in metalloenzymes. *Nat Chem* **2016**, *8*, 663-669.

(12) Frisch, M.; Trucks, G.; Schlegel, H.; Scuseria, G.; Robb, M.; Cheeseman, J.; Montgomery, J.; Vreven, T.; Kudin, K.; Burant, J. Gaussian 03, revision C. 02. **2008**.

(13) Parr, R. G. Density Functional Theory. *Annual Review of Physical Chemistry* **1983**, *34*, 631-656.

(14) Zhao, Y.; Truhlar, D. The M06 suite of density functionals for main group thermochemistry, thermochemical kinetics, noncovalent interactions, excited states, and transition elements: two new functionals and systematic testing of four M06-class functionals and 12 other functionals. *Theor Chem Account* **2008**, *120*, 215-241.

(15) Li, T.; Taylor-Edinbyrd, K.; Kumar, R. A computational study of the effect of the metal organic framework environment on the release of chemically stored nitric oxide. *Physical Chemistry Chemical Physics* **2015**, *17*, 23403-23412.

CHAPTER 3. MOLUECLAR DYNAMICS SIMULATIONS OF METAL ORGANIC FRAMEWORKS

3.1 Introduction to Molecular Dynamics Simulations

Employment of extremely accurate computational methods including quantum mechanics comes at a large cost with limitations in system size and time scale. The advent of simulation methods that utilize classical treatment of the system provide the ability to study larger, more complex systems along relevant time scales, albeit with less accuracy. Although quantum mechanical calculations are ideal, the large size of our system and time scales needed to probe relevant events, these methods are unfeasible. Molecular dynamics (MD) is a computational method capable of simulating the motions of atoms and molecules through numerical integration of Newton's laws of motion. Following Newton's second law of motion,

$$F_i = m_i a_i \qquad \text{(Equation 3.1)}$$

the acceleration (a) of an object is directly proportional to the magnitude of the force (F), where m is the mass of an object. From this, the dynamical behavior of a system at any time (t) can be predicted as the system propagates through time. The force each atom exerts on all other atoms in the simulation can also be expressed through Equation 3.2 where the negative gradient (∇) of the potential energy (U) defines the force as:

$$F_i = -\nabla_i U \qquad \text{(Equation 3.2)}$$

here the potential energy is derived from parameters of the force field. Force fields provide a simplified description of the systems under study.[17,18] The representation of a classical force field shows the intramolecular (bonded) and intermolecular (non-bonded) interactions as follows:

$$E_{total} = E_{bonded} + E_{nonbonded} \qquad \text{(Equation 3.3)}$$

The bonded and non-bonded components are broken down below:

$$E_{bonded} = E_{bond} + E_{angle} + E_{dihedral} \qquad \text{(Equation 3.4)}$$

$$E_{nonbonded} = E_{electrostatic} + E_{vdw} \qquad \text{(Equation 3.5)}$$

The bonded terms depend on the following Equations for the bond, angle and dihedral (torsional angle), respectively:

$$V_{bond}\left(r_{ij}\right) = \frac{k_{ij}}{2}\left(r_{ij} - r_0\right)^2 \qquad \text{(Equation 3.6)}$$

$$V_{angle}\left(\theta\right) = \frac{k_{ijk}^{\theta}}{2}\left(\theta_{ijk} - \theta_{ijk}^0\right)^2 \qquad \text{(Equation 3.7)}$$

$$V_{torsion}\left(\phi_{ijkl}\right) = \sum_n \frac{V_n}{2}\left[1 + \cos\left(n\phi_{ijkl} + \phi_o\right)\right] \qquad \text{(Equation 3.8)}$$

where k is the force constant, r_{ij} is the distance between particles i and j, r_0 is the equilibrium bond distance, θ_{ijk} is the angle between i, j and k, θ_{ijk}^0 is the equilibrium angle between i, j and k, ϕ_{ijkl} is the dihedral angle between i, j, k, l, V_n is the barrier

height, n is an integer and ϕ_o equilibrium dihedral angle. Non-bonded terms such as the electrostatic ($E_{electrostatic}$) and van der Waals (E_{vdw}) components are represented by the Coulomb interactions of point charges located on an atom and Lennard-Jones type interactions, respectively. The electrostatic term is dependent on the charge of particles (i and j), q, as a function of their separation distance, r_{ij}. The interaction can be described by the Equation:

$$V_{elec.}\left(r_{ij}\right) = \frac{q_i q_j}{4\pi\varepsilon_o r_{ij}} \qquad \text{(Equation 3.9)}$$

It is here that we should also discuss the Lennard-Jones (LJ or 12-6) potential as it describes van der Waals interactions. The Lennard-Jones potential describes the energy (intermolecular potential) of interaction between two atoms as a function of distance and can be mathematically depicted as:

$$V_{LJ} = 4\varepsilon\left[\left(\frac{\sigma}{r_{ij}}\right)^{12} - \left(\frac{\sigma}{r_{ij}}\right)^{6}\right] \qquad \text{(Equation 3.10)}$$

where ε is the well depth and conveys how strongly two atoms attract each other and σ is the distance in which the intermolecular potential for the two particles equals zero. Equation 3.11 can be rewritten through the combination of Equations

3.6-3.10 as follows:

$$E = \frac{k_{ij}}{2}\left(r_{ij} - r_0\right)^2 + \frac{k_{ijk}^{\theta}}{2}\left(\theta_{ijk} - \theta_{ijk}^0\right)^2 + \sum_n \frac{V_n}{2}\left[1 + \cos\left(n\phi_{ijkl} + \phi_o\right)\right] + \frac{q_i q_j}{4\pi\varepsilon_o r_{ij}} + 4\varepsilon\left[\left(\frac{\sigma}{r_{ij}}\right)^{12} - \left(\frac{\sigma}{r_{ij}}\right)^{6}\right]$$

(Equation 3.11)

While several force fields are available, the Dreiding force field[19] was chosen due to work by Zhao et al. to develop accurate force fields capable of retaining Cu-BTC flexibility characteristics.[5] Parameters are provided from this simplified force field for all atoms except the van der Waals interactions of Cu(I) with S, N, O, C atoms of the RSNO species and the atoms of the ethanol molecule. Using the above force-field descriptions, molecular dynamics simulations of the system can be carried out. As monitoring the free energy as function of Cu(I)-S distance is critical to understanding the approach of an RSNO to the copper catalytic center, adequate sampling of phase space along the Cu(I)-S reaction coordinate is necessary.

In MD simulations the complete sampling across all phase space is essential to satisfy the ergodic hypothesis, which states that the time average of a system is equal to the ensemble average. In theory, given an infinite amount of time, all possible states within a system will be sampled. Due to finite simulation times and the existence of barriers much larger than k_BT, complete sampling of all phase space may not occur for rare events. Furthermore, as a result of these barriers, it is possible to become trapped within a local minimum thus reducing sampling. Methods capable of adequate sampling in unfavorable regions to satisfy ergodicity are named enhanced sampling methods.

One such algorithm is that of umbrella sampling (US), which can apply a bias in the form of a harmonic potential along a reaction coordinate. In our simulation the Cu-S distance is scanned, as it is the reaction coordinate chosen to be studied. The mathematical representation of the bias is below[8]:

$$\omega_i\left(\xi\right) = \frac{\boldsymbol{k}}{\mathbf{2}}\left(\xi - \xi_i^{ref}\right)^2 \qquad \text{(Equation 3.12)}$$

where $\omega_i\left(\xi\right)$ is the bias potential, k is the force constant and ξ is the reaction coordinate. The bias potential forces the simulations to sample the region around ξ_i^{ref} by restricting the system within a specific window The removal of this bias upon completion of the simulation is executed by the weighted histogram analysis method (WHAM) as long as sufficient overlap in sampling has occurred.[20] As the name implies, WHAM ensures that the different configurations explored are weighted, instead of taken into account evenly. Utilization of WHAM is crucial, as umbrella sampling alone doesn't produce a meaningful free energy surface due to the existence of the bias. The unbiased free energy, $A_i\left(\xi\right)$, can be obtained from the following Equation:

$$A_i(\xi) = -\left(\frac{1}{\beta}\right)\ln P_i^b(\xi) - \omega_i(\xi) + F_i \qquad \text{(Equation 3.13)}$$

where $\beta = \frac{1}{k_b T}$, P_i^b is the biased probability distribution, $\omega_i\left(\xi\right)$ is the bias potential and F_i is arbitrarily chosen.

Behaviors associated with finite systems display different properties than bulk systems; these differences are more distinct along the boundaries of a system and result in surface effects along the boundary of the simulation box. Periodic boundary conditions provide a solution capable of infinitely expressing a finite system to minimize surface effects and imitate a system with bulk behavior. This method involves the infinite replication of the original image in all three directions and requires a concomitant movement of the image particles with the original particle; movement out of the simulation box in one direction ensures its reappearance in the opposite direction with the same velocity. Careful consideration must be taken to prevent interactions between images while preserving the ability for all other interactions to be considered. The minimum image convention states that for each particle only interactions occurring with the nearest copy of all other remaining particles are considered.

Integrators are needed in MD simulations to model the time evolution of a system. The trajectory of an atom requires the acceleration to be calculated through use of the known force and masses of the atoms in the system. The second derivative of acceleration (a) can be defined from Equation 3.1 as:

$$a = \frac{d^2x}{dt^2} = \frac{F_i}{m_i} \qquad \text{(Equation 3.14)}$$

where x is the position, F is the force and m is the mass of an object. A commonly used integrator in MD simulations is the Verlet Leapfrog algorithm. As the name

implies, this algorithm calculates the velocity (v) and position (x) in separate ("leaping") steps as show below:

$$x_{n+1} = x_n + v_{n+1/2}\Delta t \qquad \text{(Equation 3.15)}$$

$$v_{n+1/2} = v_{n-1/2} + \frac{f_n}{m}\Delta t \qquad \text{(Equation 3.16)}$$

where m is the mass of the particle and f is the force. In this integration scheme the position is updated at integer times while updates to the velocity occur at half-time steps.

3.2 Computational Methods for Condensed Phase MD Simulations

Intermolecular interactions of the system are defined through Coulomb interactions between partial charges located on the atomic sites and van der Waals interactions, represented using Lennard-Jones potentials. The present work includes the use of fitted Lennard-Jones parameters previously described (in Chapter 2) for the van der Waals interactions between Cu(I)/CH_3SNO and extrapolates them onto the -CSNO atoms of GSNO, CysNO and SNAP molecules. Similar methods were performed to represent the Lennard-Jones potentials for interactions between Cu(I) and ethanol. Intramolecular parameters for the MOFs were obtained from the work of Yang et al.;[5,6] parameters for the remaining molecules are obtained from the Dreiding force field[19].

All simulations were performed through the employment of the GROMACS package[21] with periodic boundary conditions and are performed in the *NPT* ensemble. To maintain the temperature of 300K and a pressure of 1 bar, a Nose-Hoover thermostat[22] and Parrinello-Rahman Barostat, [23] respectively, were used. Long-range electrostatics are addressed using the smoothed particle mesh Ewald (SPME) algorithm[24]. The real space cutoff distance used is 9 Å and van der Waals interaction cutoff was set at 12 Å with a 0.5 fs time step.

Electronic structure calculations described in Chapter 2 reveal the existence of two catalytic centers, Cu^{+} and $[Cu^{2+}\text{-}SR^{-}]^{+}$, both capable of releasing nitric oxide from the RSNO precursors upon their approach towards the reactive centers. Consequently, the reaction coordinate for this study is taken to be the Cu-S distance. Although electronic structure calculations were capable of showing bond topologies, this work does not use reactive modes, thus bond breaking and formation cannot be seen. This work focuses on understanding the possible effects of the environment on the reaction rate and the associated barriers as various RSNO moieties approach the catalytic copper center of both HKUST-1 and MOF-143.

3.2.1 Free Copper Solutions. Two sets of simulations were carried out for the free copper (I) case in an ethanol solution for each RSNO moiety. Firstly, the approach of an initial RSNO to the Cu(I) site was studied and denoted as 1RSNO. Upon interaction of 1RSNO with the Cu(I) center, a second simulation was carried out to study the barriers corresponding to the approach of a second RSNO, namely 2RSNO.

Furthermore, approach of the second RSNO to this Cu-SR reactive site, the second type of catalytic center proposed in this work, demonstrates an additional route for the catalytic conversion of RSNO to free nitric oxide.

In the free copper case of one RSNO, a periodic cubic box with an initial length of 27 Å was used. This simulation box contained one RSNO, one copper in the +1 oxidation state and 206 ethanol molecules. To facilitate the addition of a subsequent RSNO it was necessary to remove an ethanol molecule for CH_3SNO and 2 ethanol molecules for the remaining RSNOs and re-equilibrate the system before a production run was carried out. The decomposition of the free energy into its enthalpic and entropic terms was performed through use of the finite-difference (FD) method in the free copper ion/CH_3SNO system at temperatures, 315 and 300 K.

3.2.2 Complex MOF Environment. In an effort to account for an array of potential pathways and thus reaction rates, three sets of simulations were performed for each RSNO in the presence of the complex MOF environment (Figure 3.1). Studies began with one RSNO (1RSNO) approaching the copper center (reduced to Cu^+), once bound at the copper center a second set of simulations are carried out with a second RSNO (2RSNO) approaching the same copper center (Cu1). A third set of simulations involved the approach of the second RSNO (RSNO2) towards the adjacent copper center, which is also reduced to Cu(I) in these simulations.

Simulations including the HKUST-1 MOF were carried out using a periodic cubic box (length of 26 Å) containing the MOF, 151 ethanol molecules and one RSNO

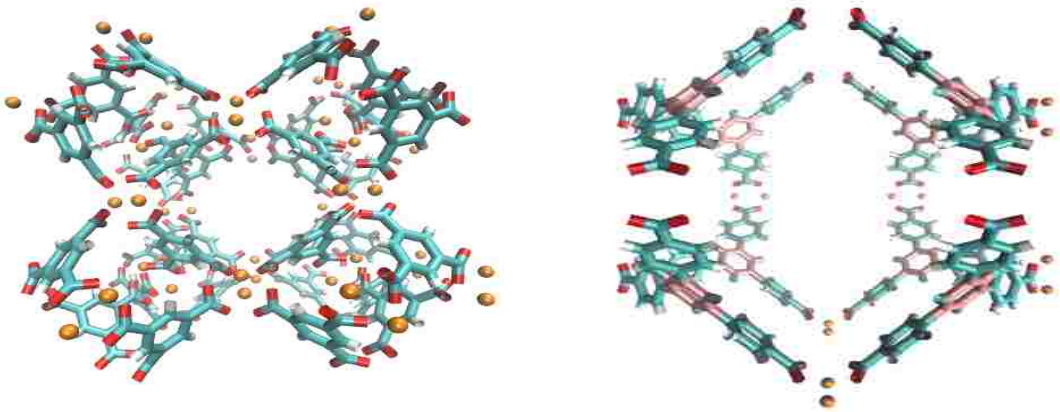

Figure 3.1. (left) Shows the HKUST-1 MOF (right) MOF-143, an analog of HKUST-1 has an extended linker leading to a large pore.

within the pore of the MOF. The HKUST-1 MOF contains 48 equivalent copper centers; one of these centers is assumed to be reduced to the Cu(I) oxidation state. The integration of a second RSNO molecule within the pore necessitates the removal of additional ethanol molecules. The crystal structure of MOF-143 was obtained from the group of Omar Yaghi[25] and visualized using the Avogadro software package[26]. As shown in Figure 3.2, MOF-143 consist of a 4,4',4''-benzene-1,3,5-triyl-tribenzoate (BTB) organic linker and copper metal center forming the copper paddle wheel structure with a pto topology unlike that of the tbo topology reported for the smaller analog HKUST-1[27]. The extended BTB linker leads to MOF-143 having a pore size diameter of 20.4Å[28], which is double that of HKUST-1.

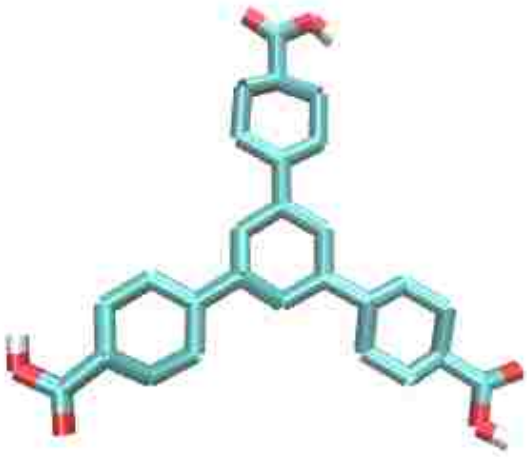

Figure 3.2. MOF-143 BTB Linker

It should also be noted that water oxygens originally present in the obtained crystal structure are removed and that the MOF is connected periodically in all three dimensions to represent an infinite framework. The dimensions of this cubic structure are a=b=c=27.4719Å[28].

MOF-143 simulations included the addition of one RSNO to the pore and 200 ethanol molecules to a periodic cubic box length of 28 Å. One of the twelve equivalent coppers is selected as the catalytic site and reduced to Cu^{+} as was seen in the case of HKUST-1. Inclusion of a second RSNO into the system requires the removal of two ethanol molecules before the approach of the second RSNO towards the identical copper site. Lastly, a third set of simulations is carried out in which the second RSNO approaches the copper site adjacent to the first reactive site currently coordinated to the first RSNO. The adjacent copper site is also reduced to the +1 oxidation state.

3.3 Results of Condensed Phase MD Simulations

The overarching goal of this work centers on understanding the factors responsible for the controlled, slow and sustained release of nitric oxide through the use of RSNO precursors in conjunction with the Cu based MOF environments. Unraveling of these factors can potentially enable the design of nitric oxide releasing systems with targeted release rates. A modification made to the size of the RSNOs organic group as well as the pore diameter of the MOF is hypothesized to have effects on the release rates of nitric oxide. From these assumptions, three

biologically compatible RSNOs (CysNO, SNAP and GSNO) were studied in both HKUST-1 and MOF143 to determine how the barriers of approach change with increasing pore diameter. Results from the MOF simulations are compared to the free copper case, which exhibits a rapid release of nitric oxide unlike the slow and sustained release of nitric oxide in the MOF environment,

Electronic structure calculations provided insight into potential collective variables in the release of nitric oxide from RSNO precursors. As a consequence of these calculations, the Cu(I)-S distance is chosen as the reaction coordinate for all simulations as this coordination results in the cleavage of the S-N bond to release nitric oxide as seen in Chapter 2. Although these quantum mechanical calculations are capable of accounting for the electrons within a system, thus the depiction of bonds breaking and forming, classical MD simulations are incapable of depicting such events without the use of reactive force fields. As such, focus is not on simulating the release of nitric oxide but rather investigating barriers associated with the approach of RSNO towards the metal center, the first step in the catalytic release of nitric oxide. The solvation environment around the copper center should also be probed during the approach of RSNO as the strong coordination of ethanol to the copper center must be overcome by RSNO to allow the Cu(I)-S coordination responsible for nitric oxide release.

The implementation of umbrella sampling (US) simulations and the weighted histogram method (WHAM)[29,30] were used to ascertain the free energy profiles of RSNOs approach as a function of the Cu-S distance. The addition of a harmonic bias

required the manipulation of relevant force constants for the purpose of adequately overlapping 17 simulation windows spanning the reaction coordinate (r_{Cu-S}) from 1.8 to 7 Å. The force constant of 85,000 kcal mol^{-1} nm^{-2} was used for windows between 2-3 Å; all other simulation windows were treated with a force constant of 35,000 kcal mol^{-1} nm^{-2}. Each free copper simulation was subjected to a 20 ns equilibration run followed by a 30 ns production run, whereas each MOF simulation was allowed to equilibrate for 30 ns and subsequently a 60 ns production run was carried out.

3.3.1 CH_3SNO, a simplified case: free copper-ion ethanol solution. The free energy profiles obtained for the approach of $1CH_3SNO$ and $2CH_3SNO$ towards the copper ion appear quite similar to one another and have little to no barrier as seen in Figure 3.3. Further scrutiny of the free energy profile shows a deep minimum at a Cu-S distance of 2 Å that is indicative of the strong coordination between the sulfur atom of RSNO and the copper ion. A critical component of this investigation centers on relating thermodynamic properties of this system to changes of the solvation environment located around the catalytic center as the RSNO approaches. By decomposing the free energy into entropic ($-T\Delta S$) and enthalpic (ΔH) terms (Figure 3.4) as CH_3SNO approaches the copper ion, inferences between observed barriers and the solvation environment can be made. Upon the approach of RSNO to the copper site, a local maximum is present at 4.3 Å, which corresponds to the location of the second solvation shell (Cu-OEtH) of copper.

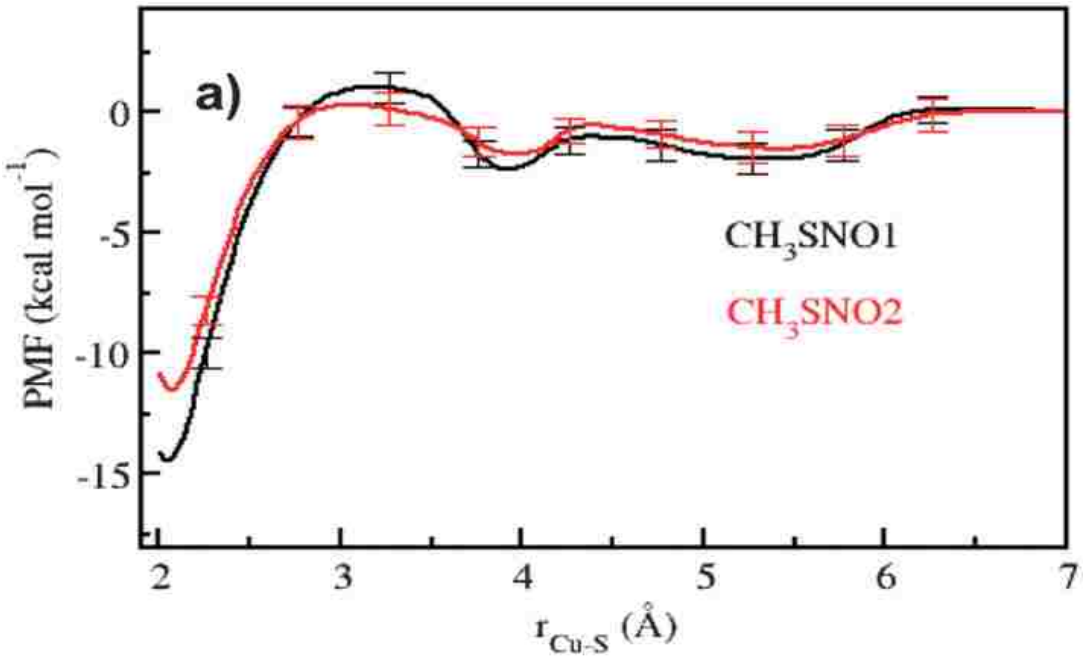

Figure 3.3. Free energy profile for CH_3SNO in the free copper ion/ethanol solution.

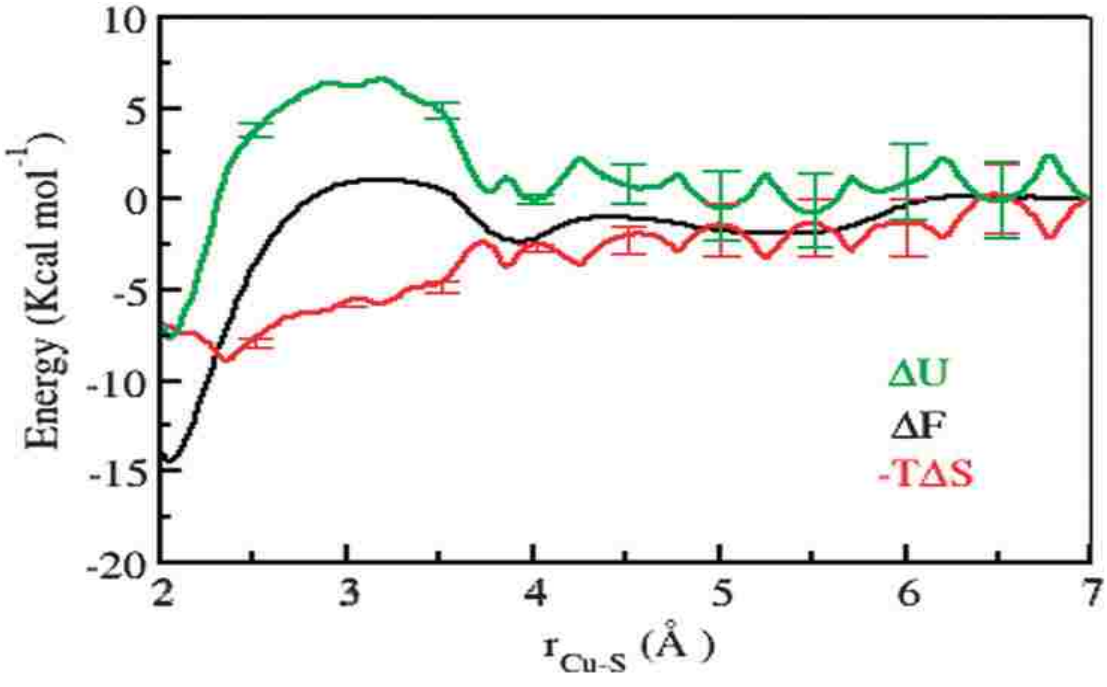

Figure 3.4. Decomposition of the free energy into entropic and enthalpic terms for CH_3SNO in the free copper ion/ethanol case.

As CH_3SNO further traverses along the Cu-S reaction coordinate, a larger barrier (3.2 Å) originating from the interruption of strong coordinate-like bonds between Cu-OEtH within the first solvation shell is encountered. The energetic penalty corresponding to the displacement of an ethanol molecule is offset by entropic gains associated with a reduction in order exhibited by the disrupted solvation shell. To further reveal the solvation environment around the copper center of interest, the radial distribution function (RDF) is computed (Figure 3.5). Through integration of the RDF from zero to the first minimum, the coordination number corresponding to the number of ethanol molecules coordinated to the copper (I) center can be written as:

$$N = \int_0^{r_0} 4\pi r^2 g(r) \rho \, dr \qquad \text{(Equation 3.17)}$$

where $g(r)$ is the radial distribution function, ρ is the bulk density of ethanol and r_0 corresponds to the position of the first minimum. The difference in coordination number for ethanol relative to when CH_3SNO is absent is presented in Table 3.1. It is apparent from this data that the approach of each CH_3SNO displaces one ethanol molecule.

3.3.2 CH_3SNO, A Simplified Case: The Complex MOF Environment of HKUST-1.

The free energy profiles generated from the approach of $1CH_3SNO$ towards the catalytic center resemble the free copper ion-CH_3SNO system. It was expected that the incorporation of this simple RSNO into the center pore would result in large

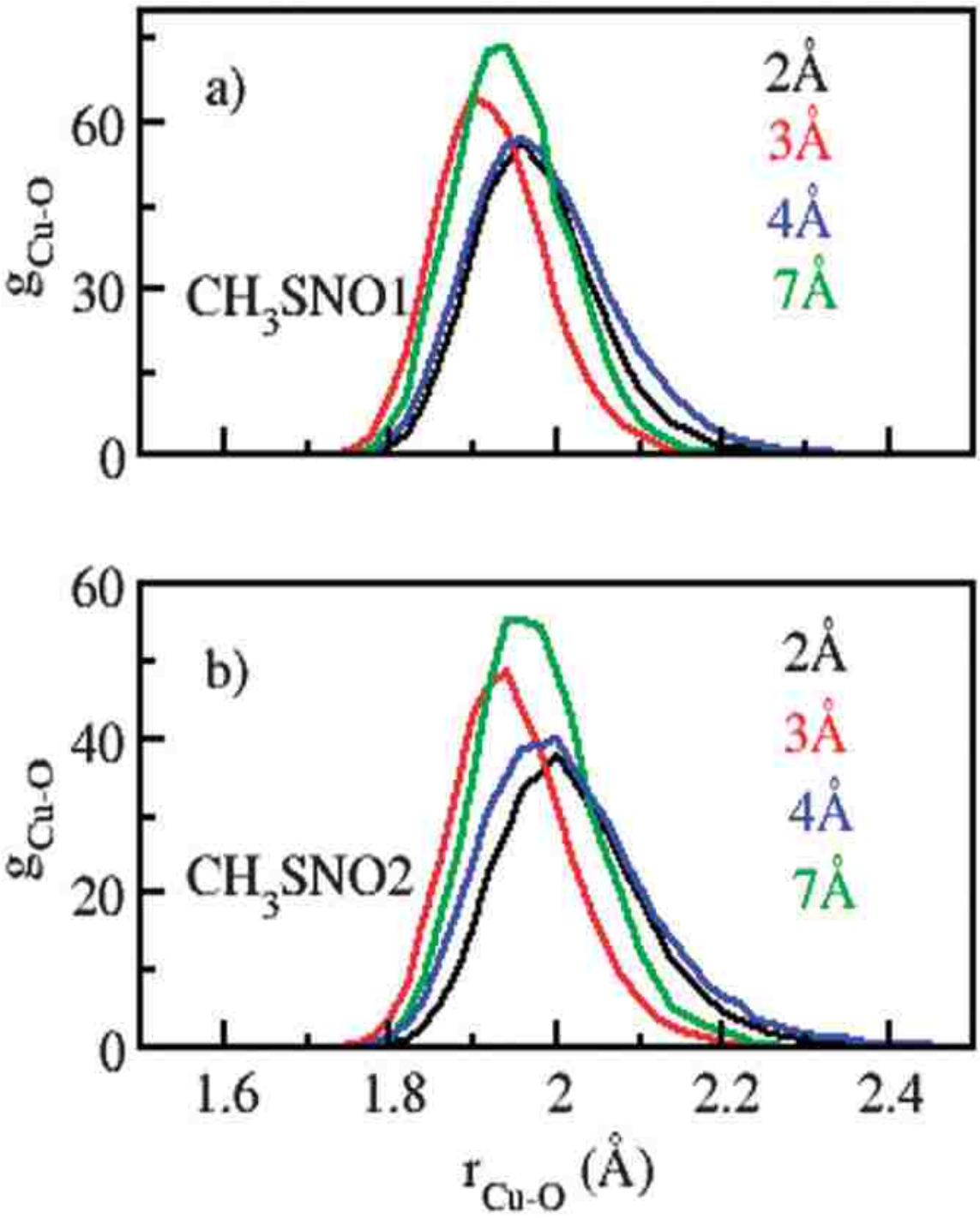

Figure 3.5. Radial distribution function (Cu-O) at various constrained Cu-S distances for one and two CH_3SNO molecules.

Table 3.1. Shows the difference in coordination number for ethanol to the copper catalytic center as CH_3SNO approaches relative to when no CH_3SNO is present.

CH_3SNO1		CH_3SNO2	
Distance (Å)	Δn	Distance (Å)	Δn
2	−1	2	−2
3	−1	3	−2
4	0	4	−1
7	0	7	−1

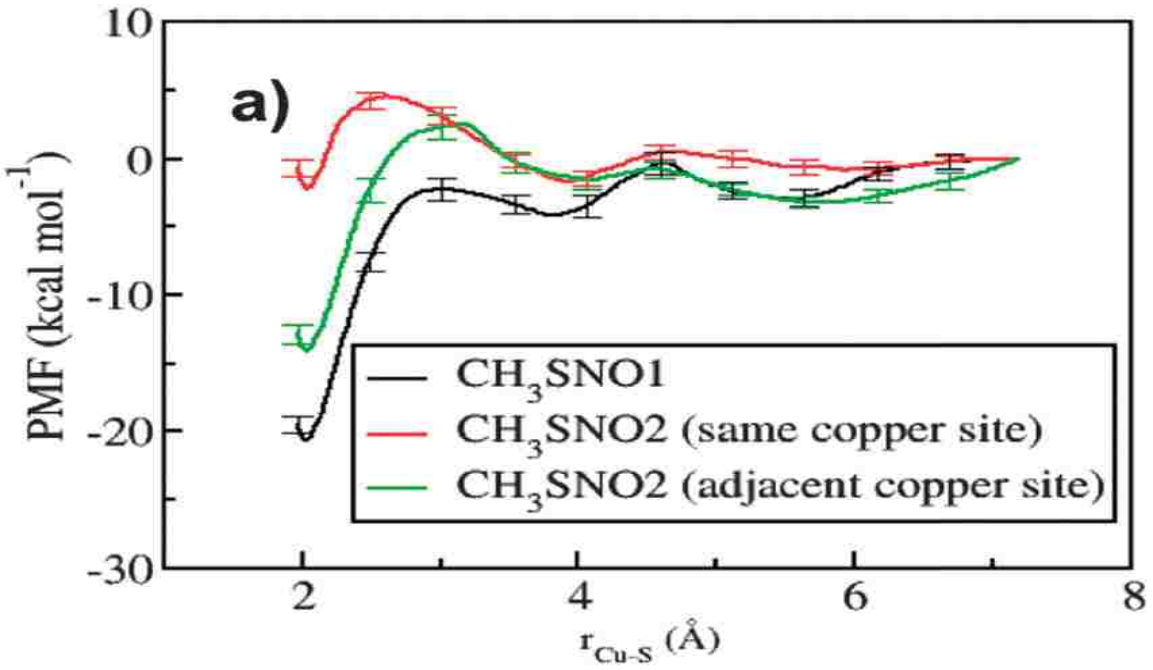

Figure 3.6. Free energy profile for simulations of three CH_3SNO cases within the HKUST-1 MOF.

barriers from steric hindrance; however, little to no barrier was observed for $1CH_3SNO$ within the HKUST-1 MOF (Figure 3.6). Furthermore, examination of the distribution angle between Cu(I), the sulfur atom of CH_3SNO and the center pore, is computed at 5 Å and 2 Å to measure steric hindrance (Figure 3.7). Narrower angles are observed as $1CH_3SNO$ continues towards the catalytic center. Although no

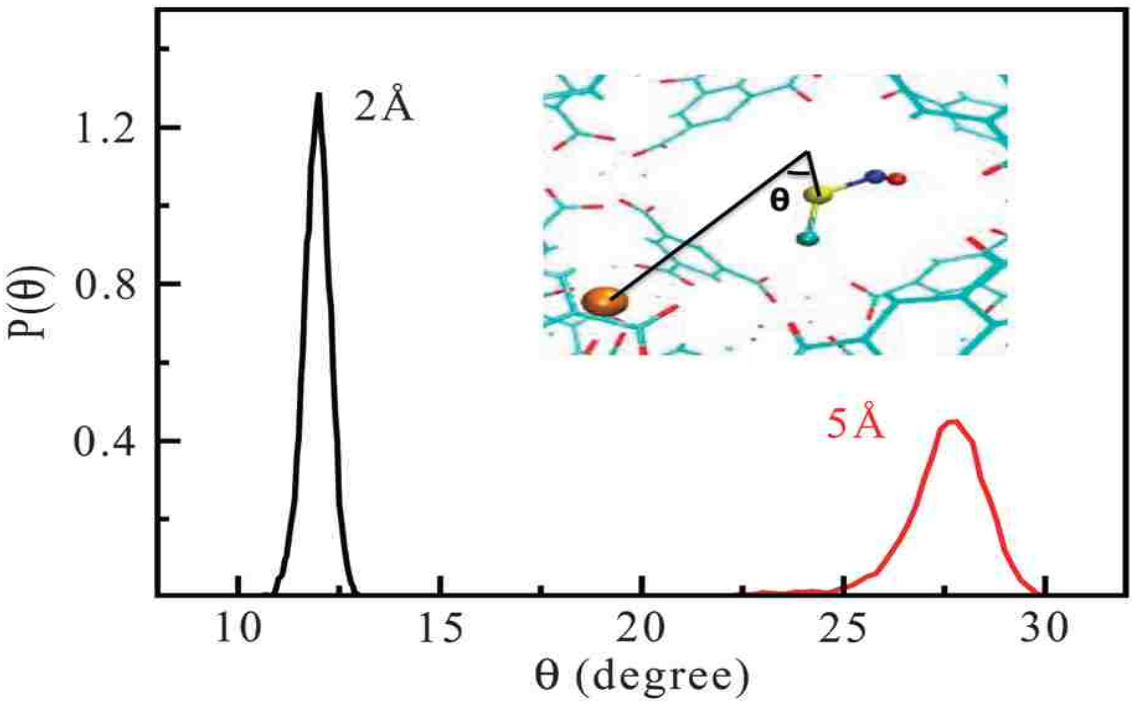

Figure 3.7. The angle distribution for the Cu(I)-center of pore-S_{RSNO} at two distances shows a narrower distribution as RSNO approaches the catalytic center.

barrier exist for the approach of $1CH_3SNO$, inclusion of a second CH_3SNO within the system shows larger free energy barriers of ~5 kcal/mol. As the distance decreases between Cu(I)-$2CH_3SNO$, examination of the trajectory shows that the first CH_3SNO is pushed out of the pore at a Cu(I)-$2CH_3SNO$ distance of 2.5 Å. The experimental work of Harding et al. suggests several rates for nitric oxide release exist.[7] The potential for different release rates of nitric oxide led to additional investigations of the environment around the catalytic copper center. Consequently, the adjacent copper site (Cu2) is reduced to the +1 oxidation state as a second CH_3SNO (referred to as CH_3SNO2) approaches and $1CH_3SNO$ remains bound to the Cu1 site (Figures 3.8, 3.9). The resulting barrier for the CH_3SNO2 case is ~2.5 kcal/mol, larger than the barrier obtained for $1CH_3SNO$ but smaller than the $2CH_3SNO$ case where the

second CH_3SNO is brought to the identical copper site. Unlike the $2CH_3SNO$ case, the approach of the CH_3SNO2 does not display a pushing effect on $1CH_3SNO$. Moreover, there is no evidence of additional steric hindrance observed by the incorporation of CH_3SNO2 at a different copper site.

In an effort to resolve the origins of the Cu2-CH_3SNO2 barrier a distribution of the distance between both coppers (Cu1 and Cu2) is examined with only one

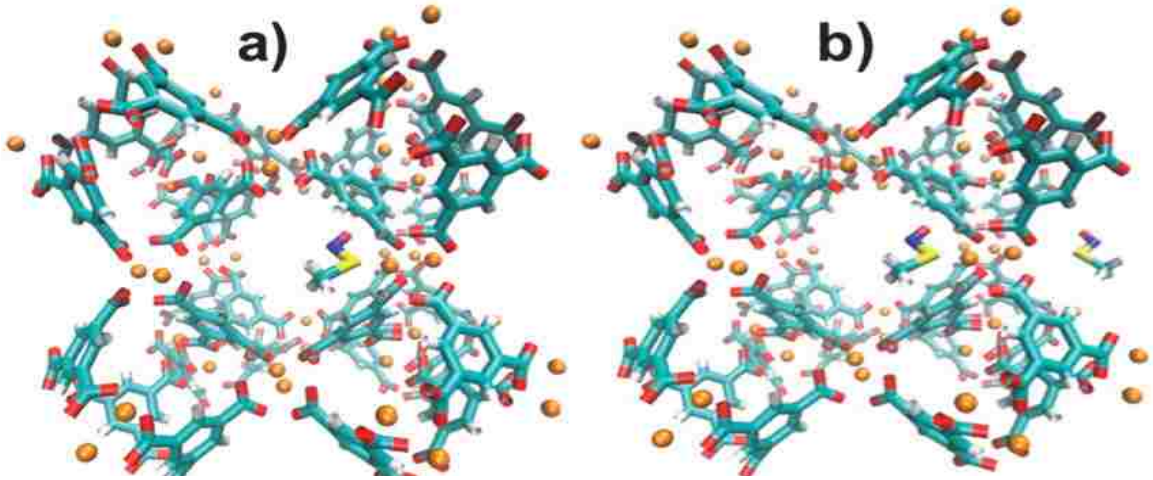

Figure 3.8. (a) HKUST-1 MOF with 1RSNO present inside the center pore. (b) A second RSNO is pulled to the adjacent copper center for the RSNO2 case.

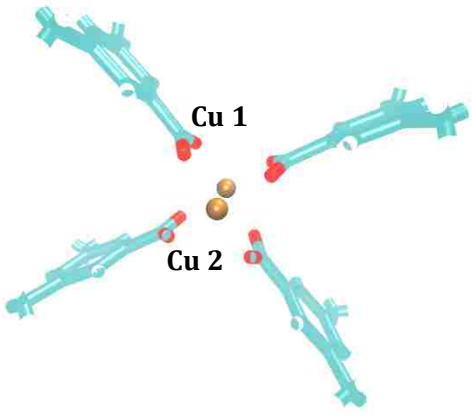

Figure 3.9. Shows the two catalytic copper sites present on each arm of the MOF. For the 1RSNO simulations: Cu 1 is reduced to the +1 oxidation state and the first RSNO approaches the copper site. 2RSNO: With the 1st RSNO fixed, a second RSNO (2RSNO) approached the same copper (Cu 1). RSNO2: Cu 2 is now **also** reduced to the +1 oxidation state and the 1st RSNO is coordinated to Cu1; however, the second RSNO (RSNO2) is now approaching the adjacent copper (Cu 2).

CH_3SNO present at the Cu1 site as well as with a CH_3SNO present at both copper sites. This distribution shows a distortion to the metal centers with distances between Cu1-Cu2 increasing from 2.5 to 3.5 Å (Figure 3.10). Work by Harding et al. shows that GSNO failed to generate nitric oxide in the presence of HKUST-1. [7] It was hypothesized that GSNOs inability to reach the catalytic centers of the MOF are a likely result of this molecules large R-group. Testing of this hypothesis leads to the incorporation of CysNO, SNAP and GSNO within a MOF with a larger pore diameter to determine the effect on the barriers of approach.

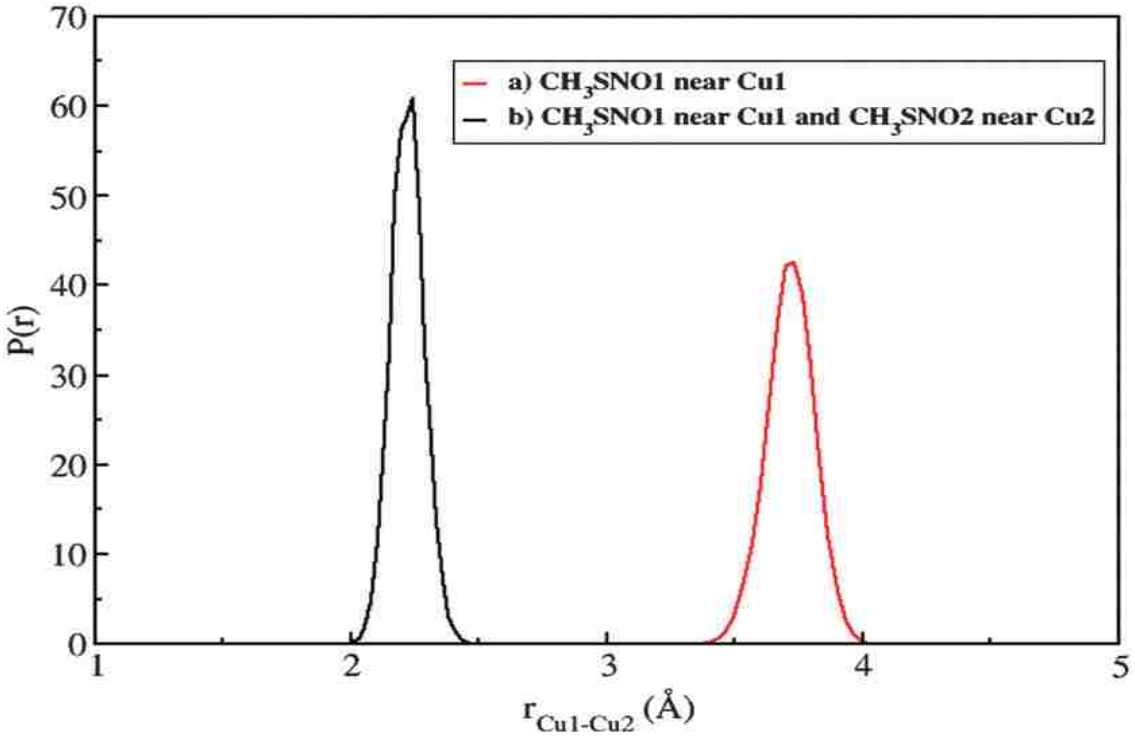

Figure 3.10. The probability distribution of the distance between the Cu1-Cu2 sites when one CH_3SNO (black line) is at the Cu1 site and a CH_3SNO is at both copper (I) sites (red line).

The remainder of this work will focus on the above-mentioned modifications and their effects on the free energy barriers and thus nitric oxide release in biologically relevant RSNOs.

3.3.3 Nitrosylated Amino Acids: Free Copper-Ion Ethanol Solution. CH_3SNO served as a simple molecule to perform initial studies for the release of nitric oxide. Further research was performed on applicable systems containing nitrosylated amino acid derivatives as nitric oxide precursors. The free energy barriers corresponding to the approach of CysNO, SNAP and GSNO in the free copper ion/ethanol solution follow the trends observed in CH_3SNO. No significant differences are observed upon the addition of a second RSNO to the free copper ion/ethanol solution as both 1 & 2RSNO cases are nearly identical (Figure 3.11). Likewise, strong coordination occurs for each case when the distance (r_{Cu-S}) reaches ~2 Å, this is depicted by the deep minimum observed at this point. Although the thermodynamic behavior of the system is of interest, understanding how the varying RSNO size effects the copper solvation environment can assist in explaining thermodynamic quantities.

The radial distribution function was calculated (Figure 3.12) to probe the solvation environment of the catalytic copper center in the ethanol solvent. At a r_{Cu-S} of 7 Å for CysNO, SNAP and GSNO, the coordination number (Figure 3.13) corresponding to the oxygen of the ethanol molecules was calculated as six in the first solvation shell around the catalytic copper center. As the distance (r_{Cu-S})

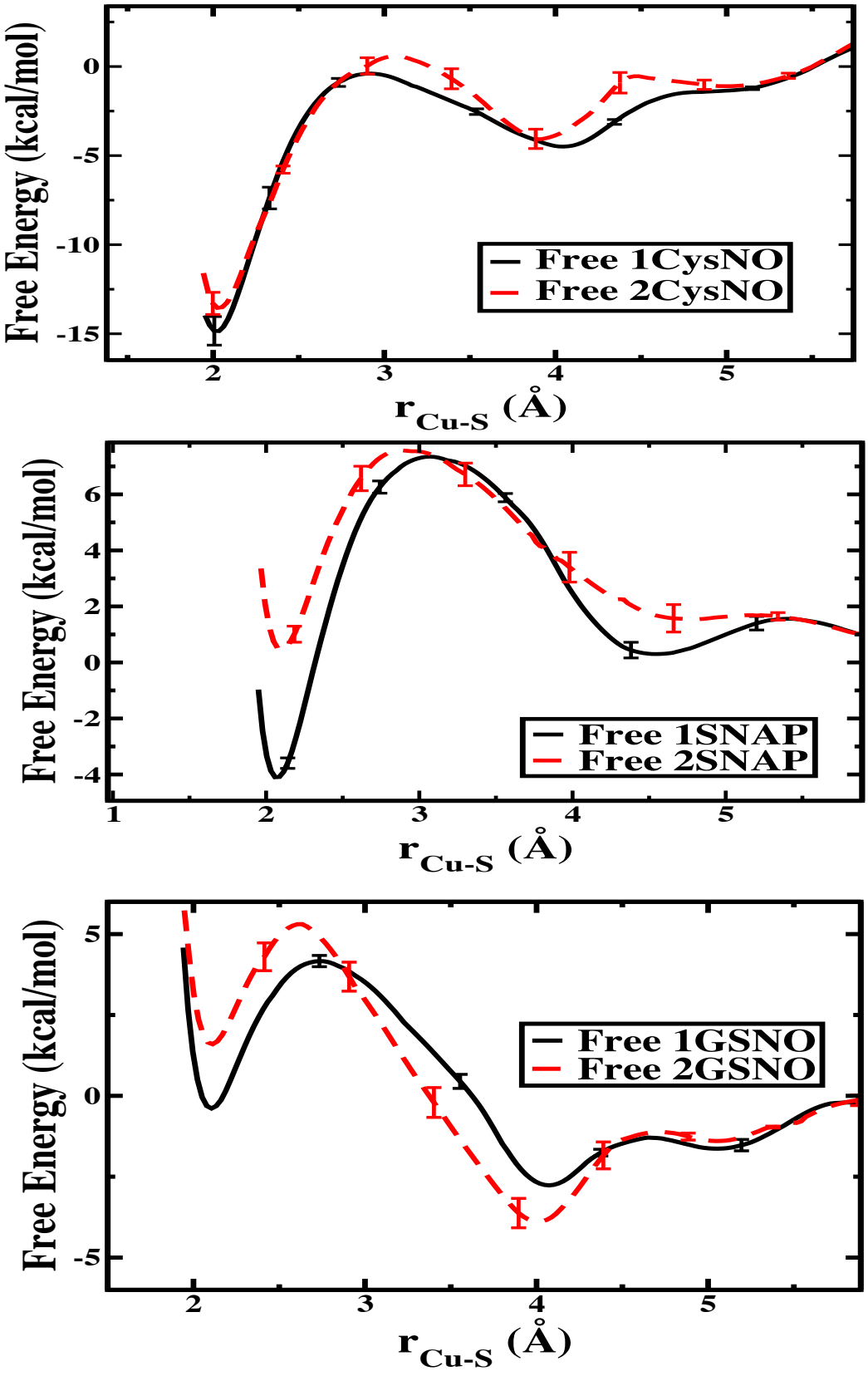

Figure 3.11. Free energy profiles for CysNO, SNAP and GSNO.

decreases there is also a decrease in the number of ethanol coordinated to the copper ion until the 1RSNO moiety completely displaces an ethanol. Upon the approach of a second RSNO (while 1RSNO bound to Cu with a distance of 2 Å) at 7 Å away from the copper center, CysNO and SNAP show nearly identical coordination numbers for the coordination of ethanol to the copper ion. Further approach of the second RSNO towards the copper results in another decrease of the coordination

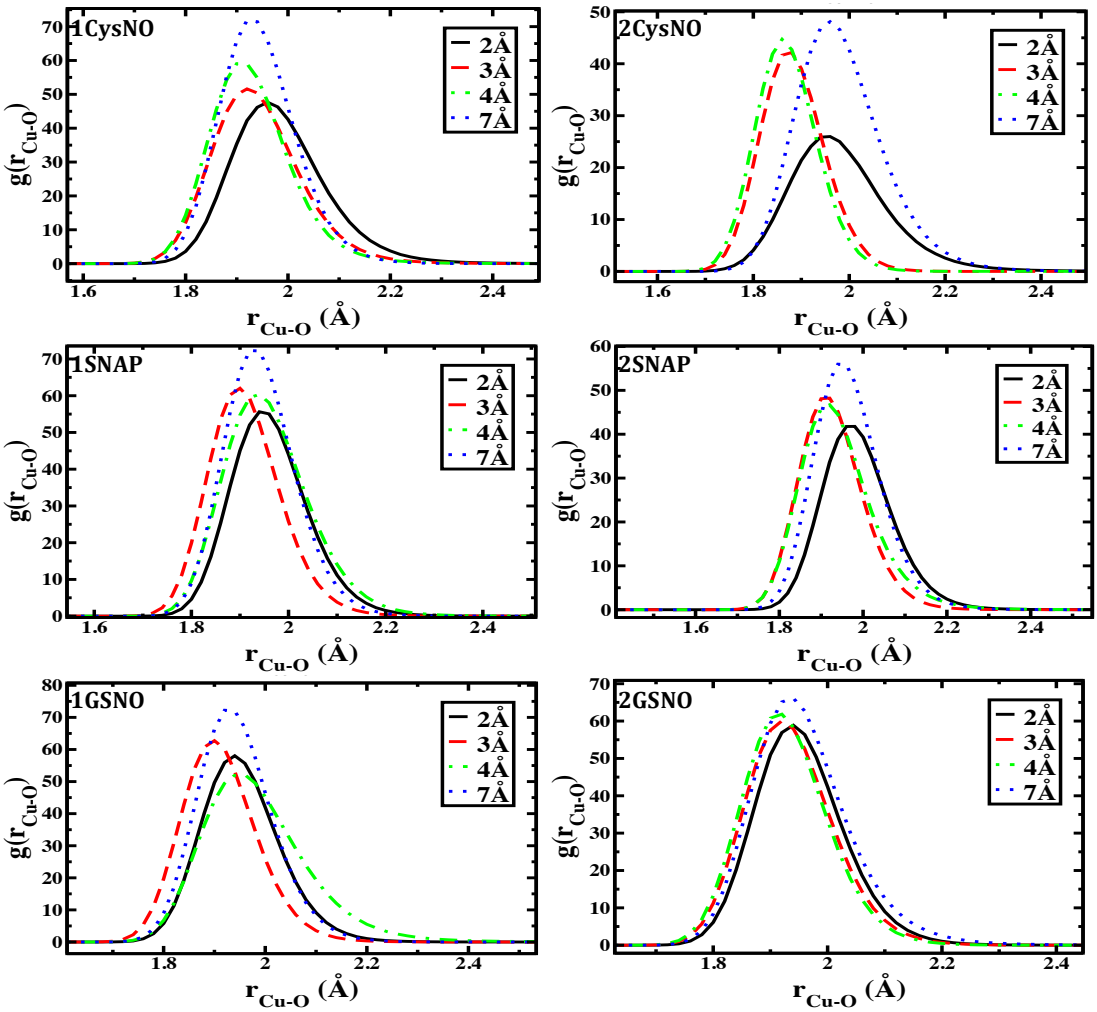

Figure 3.12. Radial distribution function for (a) CysNO (b) SNAP and (c) GSNO in the free copper ion/ethanol solution. Cu-S distances are constrained in various windows.

number by one; this can be interpreted as another ethanol being replaced by the second RSNO in both the CysNO and SNAP cases.

Moreover, the calculated coordination number as 1GSNO approaches the copper center results in the complete removal of one ethanol molecule. Unlike CH_3SNO, CysNO and SNAP, the integrated coordination numbers of GSNO shows a net replacement of only one ethanol molecule upon the coordination of 2GSNO with

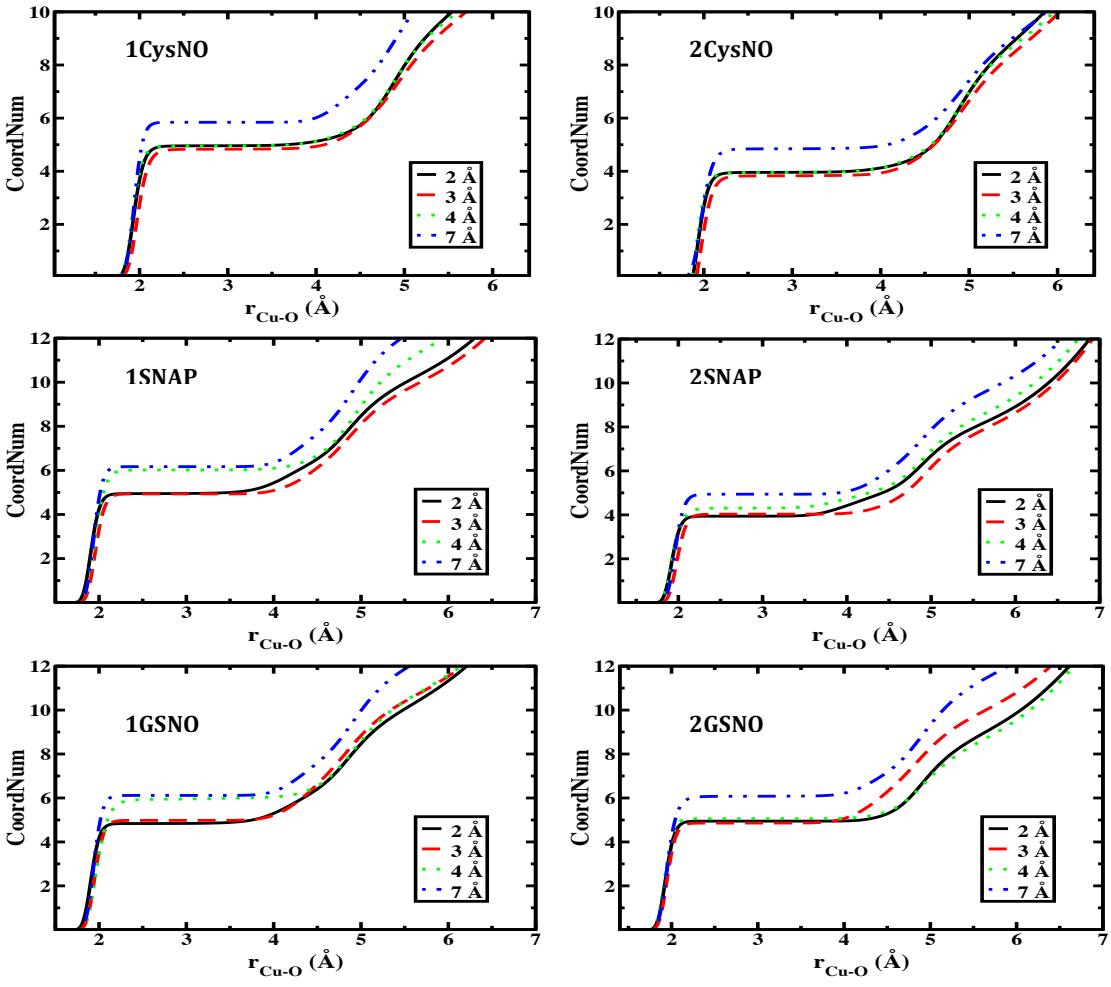

Figure 3.13. Integrated coordination numbers for ethanol molecules coordinated to copper (I) in the free copper/ethanol solution for different US windows (corresponding to different Cu(I)—S distances).

the catalytic center. Interestingly, the approach of the second GSNO towards the copper site immediately pushes away the first GSNO a substantial distance. This is a likely explanation for the removal of only one (net) ethanol molecule for the GSNO system. Additionally, the free energy profile as well as the Cu-O radial distribution functions for GSNO is quite similar to one another.

3.3.4 Nitrosylated Amino Acids: HKUST-1. The incorporation of additional RSNOs beyond the simple CH_3SNO test case is studied. For CysNO and SNAP species, the same qualitative trends of CH_3SNO are observed. Although CysNO and SNAP barriers for 1RSNO cases are minimal, the approach of a second RSNO results in a free energy barrier of approximately 20 kcal mol^{-1} and 15 kcal mol^{-1} for CysNO and SNAP, respectively (Figure 3.14). As seen in the case of CH_3SNO the largest barriers are observed upon the addition of a second RSNO towards the identical catalytic copper center. Harding et al. also attempted to generate nitric oxide from GSNO but reported the inability of GSNO to produce nitric oxide through interactions with the HKUST-1 MOF. A likely conclusion is that the large size of GSNO restricts its access to the catalytic center of the framework.

Unlike the small free energy barriers encountered for one CysNO and SNAP, 1GSNO produces a free energy barrier approximately 13 kcal mol^{-1} (Figure 3.15). The large barrier that GSNO must overcome upon its approach to the copper center suggests that GSNO is too large to fit within the HKUST-1 pore. Probing of this system was only performed with 1GSNO, as it is unlikely a second GSNO would be

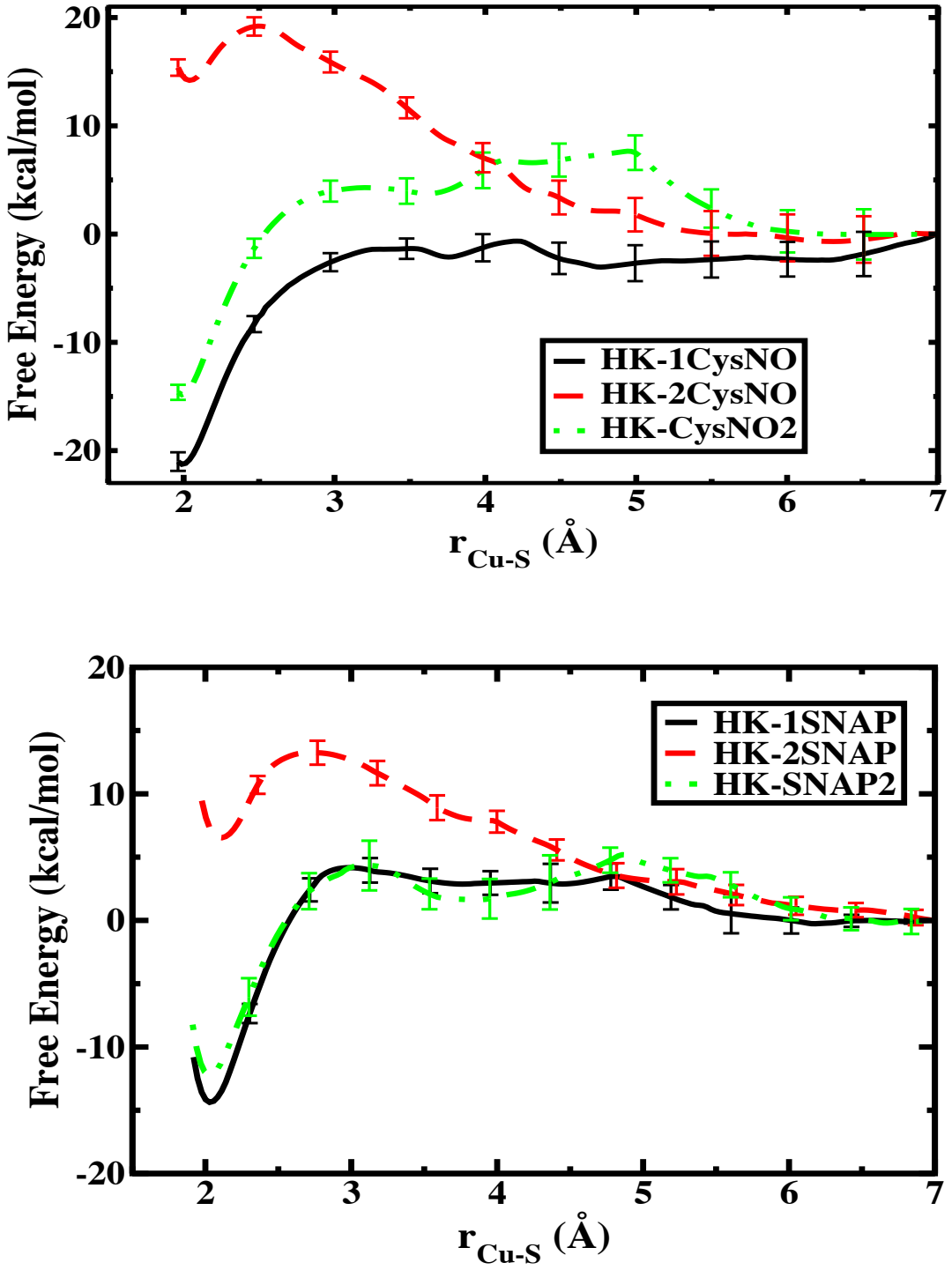

Figure 3.14. The free energy profiles show the barriers associated with the approach of (top) CysNO and (botom) SNAP towards the HKUST-1 MOF.

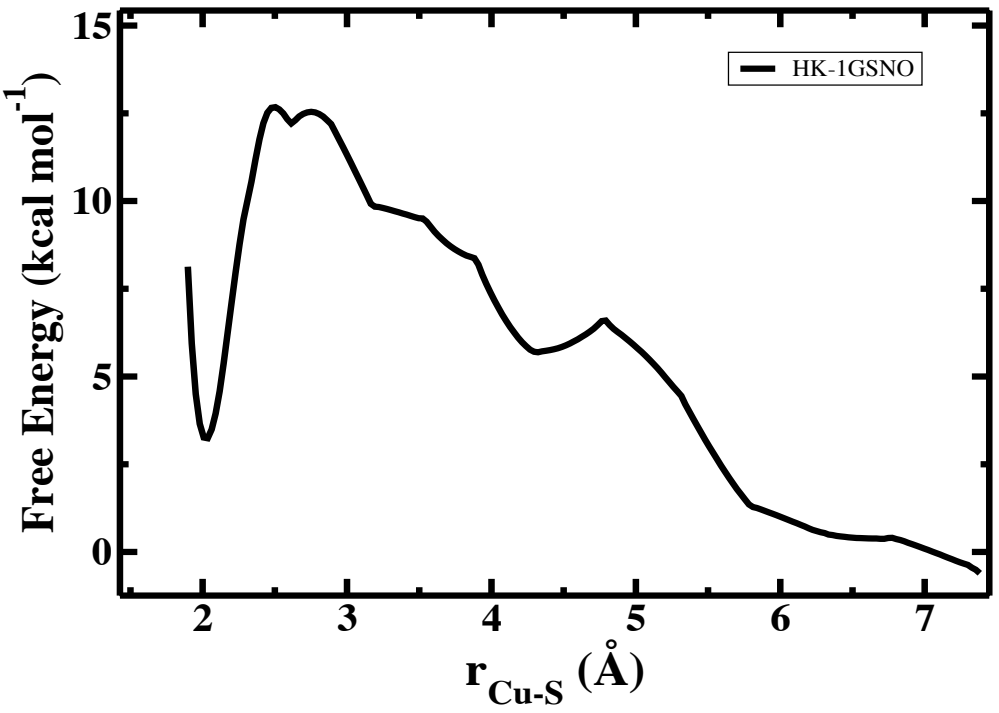

Figure 3.15. The free energy profile of 1GSNO shows a large energy barrier as it approaches the HKUST-1 catalytic center.

capable of simultaneously fitting within the HKUST-1 pore. Modulation of the release rate of nitric oxide has been explored through modifications of the RSNO R-group. Likewise, changes to the organic linker of the MOF are also assumed to affect the release rates of nitric oxide from its RSNO precursor.

3.3.5 Nitrosylated Amino Acids: MOF-143. Like the free copper/ethanol solution simulations, the approach of the first RSNO in all three cases results in a free energy profile that has little to no barrier (Figures 3.16, 3.17). Upon the addition of the second RSNOs (CysNO and SNAP), drastic changes are observed from the free copper cases. Similar to the 1RSNO cases, the approach of the second RSNO towards the adjacent

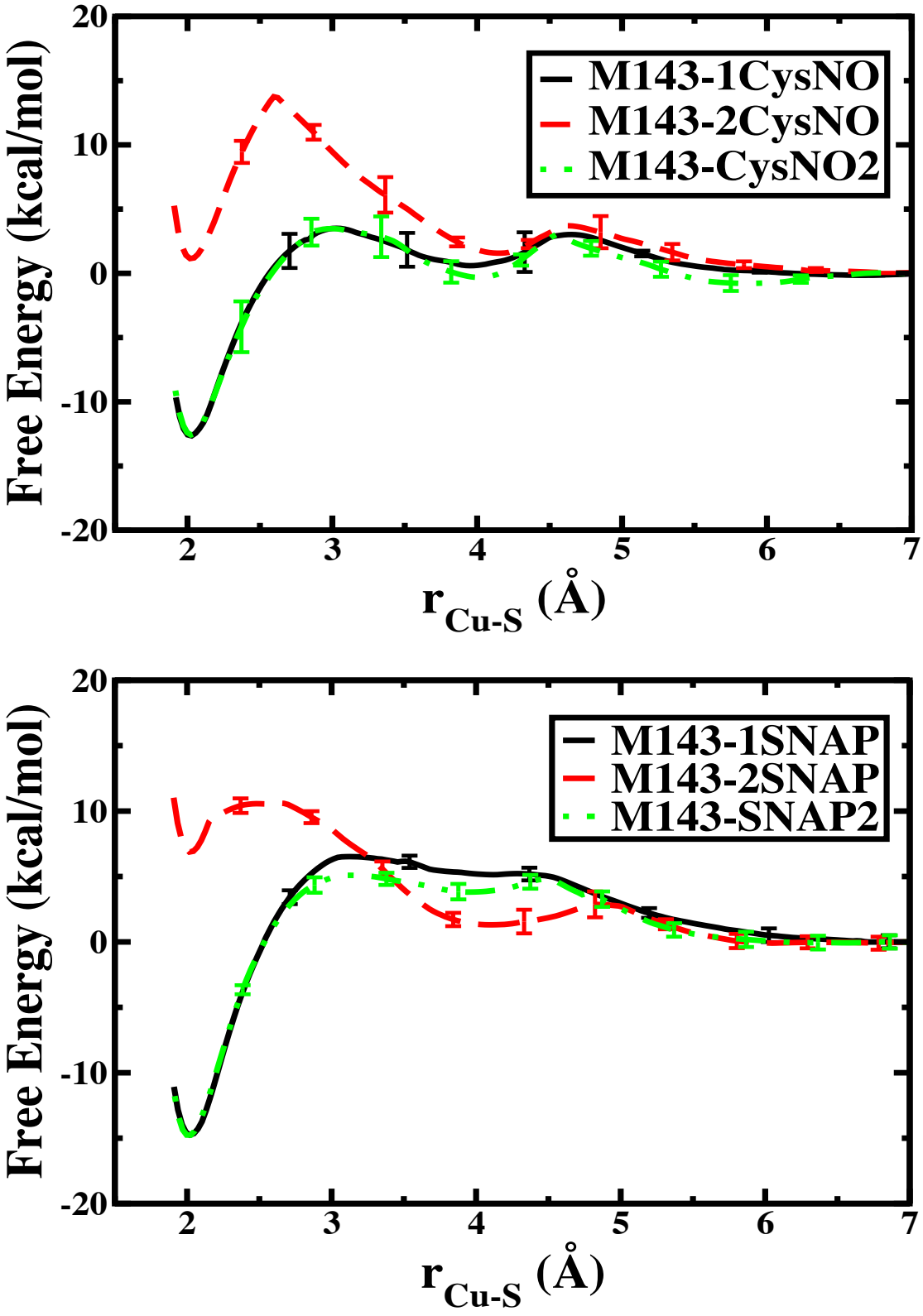

Figure 3.16. The free energy profile of (top) CysNO and (bottom) SNAP shows a large energy barrier as it approaches the HKUST-1 catalytic center.

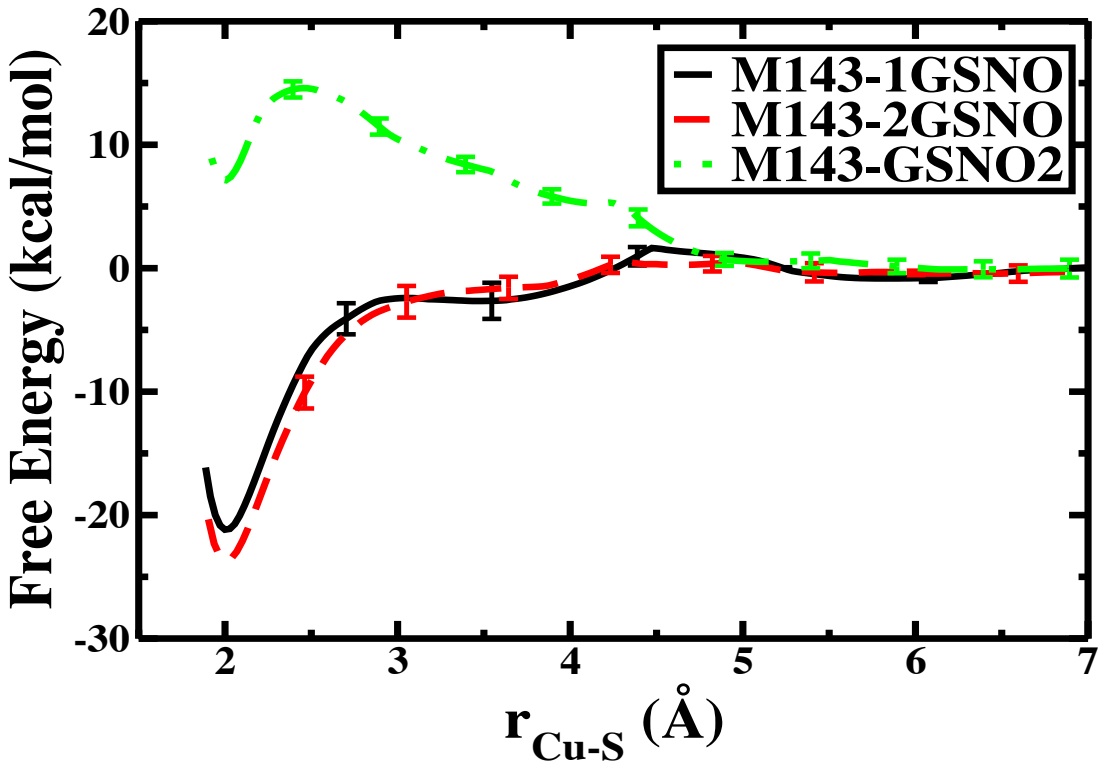

Figure 3.17. The free energy profile as GSNO approaches the copper catalytic center within the HKUST-1 MOF.

copper center (while 1RSNO is remains bound to the original copper) produces a free energy profile with relatively small barriers. Intriguingly, probing of GSNO in the presence of MOF-143 reveals that the approach of a second GSNO towards the identical copper center results in a free energy barrier nearly identical to the 1GSNO case. In contrast to the RSNO2 cases of CysNO and SNAP, the approach of GSNO2 to the adjacent copper exhibits a large free energy barrier with respect to the 1GSNO case. The barrier observed for GSNO2 looks similar to the barriers typically observed in the 2RSNO cases of H_3SNO, CysNO and SNAP.

To further understand the effects of the MOF environment on the RSNO species approach towards the catalytic center, information on the short-range

atomic makeup of the system is explored through radial distribution functions (Figure 3.18) in an effort to elucidate the solvation environment. A change of -1 for the coordination number of ethanol to the catalytically active copper is calculated as 1CysNO approaches a bond distance of approximately 2 Å to the copper ion (Figure 3.19). Although slightly larger in size, the SNAP molecule sees a similar decrease in coordination of ethanol to copper as is encountered for CysNO. The approach of GSNO is quite dissimilar to that of CysNO and SNAP in which both can occupy the pore simultaneously, thus their higher barriers for their 2RSNO systems.

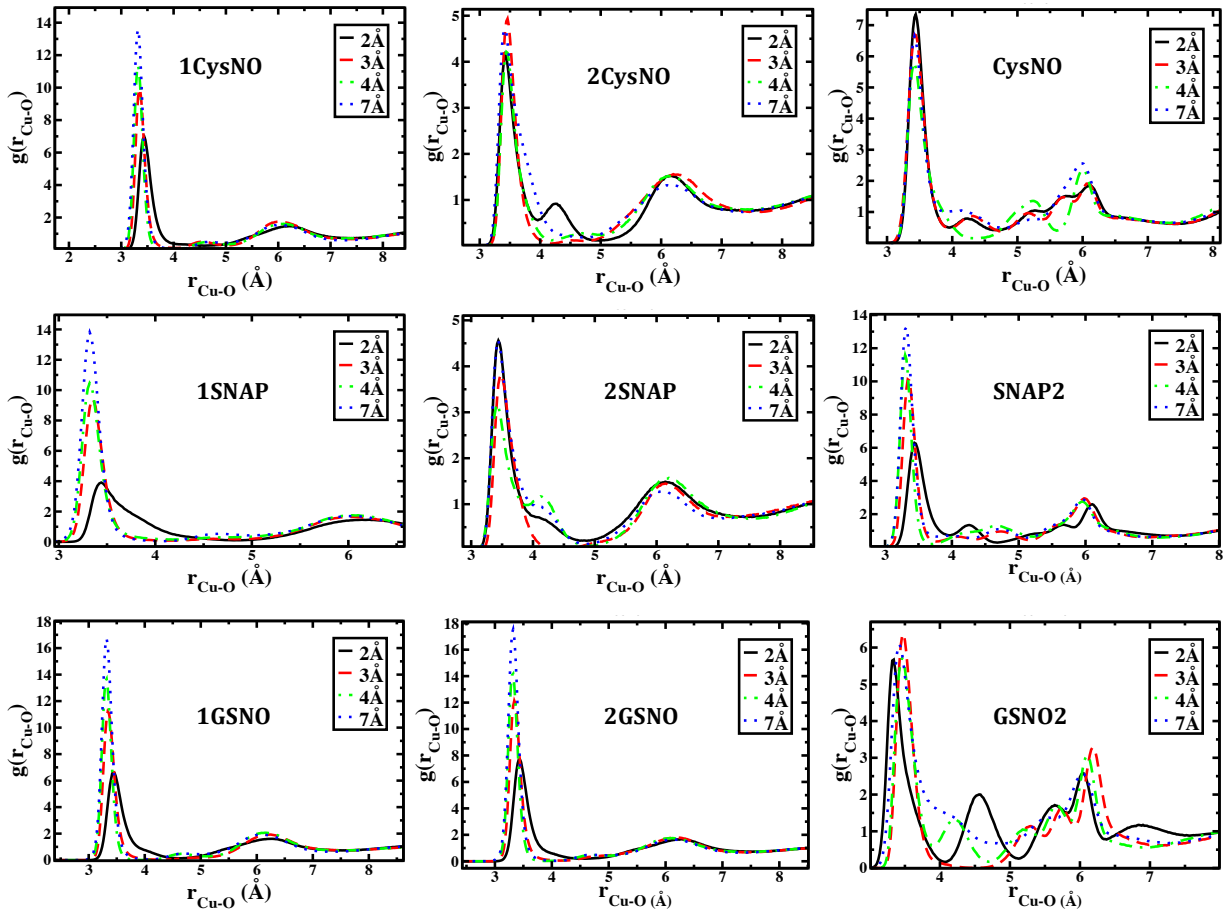

Figure 3.18. Radial distribution function for the (a) CysNO (b) SNAP and (c) GSNO with the $r_{Cu\text{-}S}$ constrained in various windows.

Furthermore, the approach of GSNO2 towards the adjacent copper center results in the net displacement of two ethanol molecules removed from the Cu1 site similar to that of the 2CysNO and 2SNAP (Figure 3.19). Unlike the RSNO2 cases of CysNO and SNAP, the approach of GSNO2 results in high-energy barriers similar to what is observed in the 2RSNO cases of CH_3SNO, CysNO and SNAP.

The barriers associated with GSNO2 can be attributed to the pushing away of a second ethanol molecule from the Cu1 site to allow GSNO2 access to the adjacent catalytic center. As such, both GSNOs are capable of nearing each while coordinating

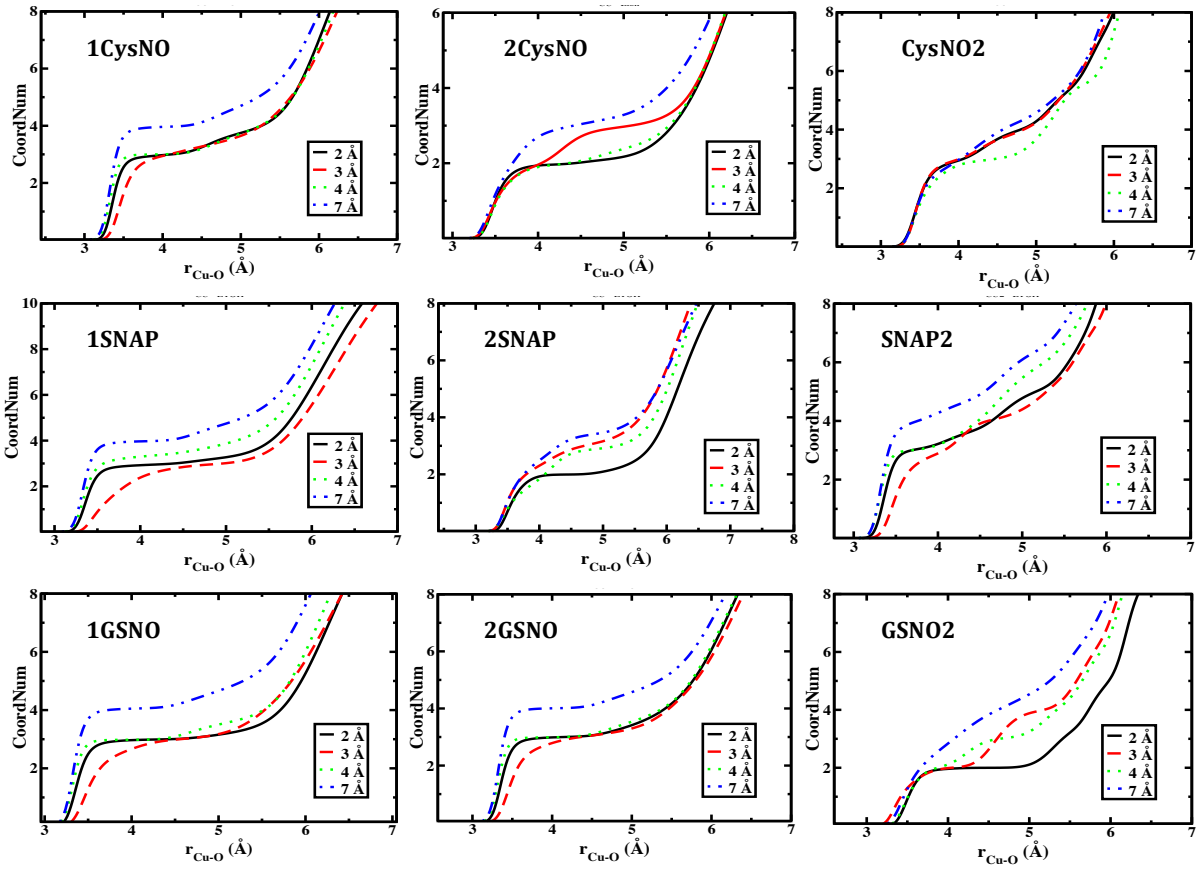

Figure 3.19. Integrated coordination numbers for ethanol molecules coordinated around copper in the MOF environment at various constrained Cu(I)-S distances.

to their respective copper sites, unlike when both approach the identical copper causing the initial GSNO to be pushed away immediately. Probing of the local solvation environment further validates the free energy profiles for 1GSNO and 2GSNO as the RDF and coordination numbers are nearly identical, suggesting that only one GSNO is capable of inhabiting the pore at a time. Interestingly, as 2GSNO is introduced into MOF143 at 7 Å, it immediately begins to push the 1GSNO molecule away from the copper center a considerable distance. Consequently, the free energy profile and RDF depicts a case that looks very much like that of 1GSNO as essentially only one GSNO is seen in the vicinity of the copper center.

To further assess how the second RSNO approaches the Cu1 center, the distribution of the S-Cu-S angle was calculated at a $r_{Cu\text{-}S}$ of 2.3 Å (Figure 3.20). From this data it is apparent that the S-Cu-S angle of 2CysNO has a more narrow distribution for its angle of approach. This explains the appearance of the shoulder

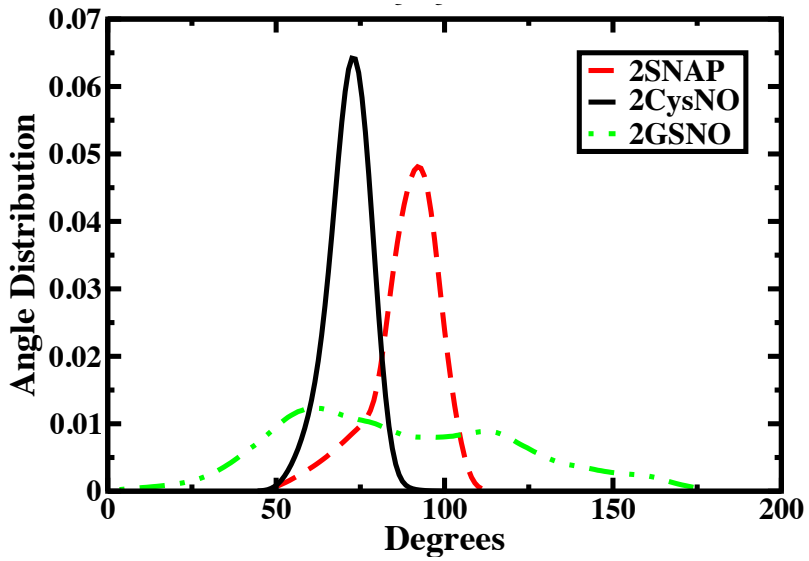

Figure 3.20. Angle distribution for the S_1-Cu-S_2 bond of a) 2CysNO b) 2SNAP and c) 2GSNO within MOF-143.

in the radial distribution function for MOF-143--2CysNO (Figure 3.18) where the small approach angle of CysNO allows an additional ethanol to move between the first and second solvation shells (Figures 3.20, 3.21). The larger approach angles of 2SNAP and 2GSNO are more restrictive of this activity. Furthermore, the large range of angles that 2GSNO takes on is likely due to the availability of space as 2GSNO pushes away the initial 1GSNO molecule upon its approach.

3.3.6 Mixed-RSNO Simulations in MOF-143. To further understand the effects of modifying the R-groups of RSNOs, simulations of mixed-RSNOs were carried out. The substantial size difference of CysNO and GSNO makes them idea candidates to study in a mixed-RSNO system for comparison with identical RSNOs. Two scenarios were investigated: firstly, CysNO bound to the copper and allowing GSNO to approach the identical copper (Cu1) and the adjacent copper (Cu2), referred to as CPG. Secondly, where GSNO is initially bound to copper and CysNO approaches Cu1 as well as Cu2, referred to as GPC.

The 2RSNO scenarios for CPG and GPC provide relatively similar free energy profiles. Scrutiny of CPG-2RSNO where CysNO is bound to copper and the GSNO is translocated towards the same copper looks somewhat similar to the profile obtained for M143-1CysNO until approximately 3 Å. It is noteworthy to mention that CysNO stays bound to copper up until this distance and begins to be pushed away from this point on in CPG-2RSNO. The approach of a second RSNO to the

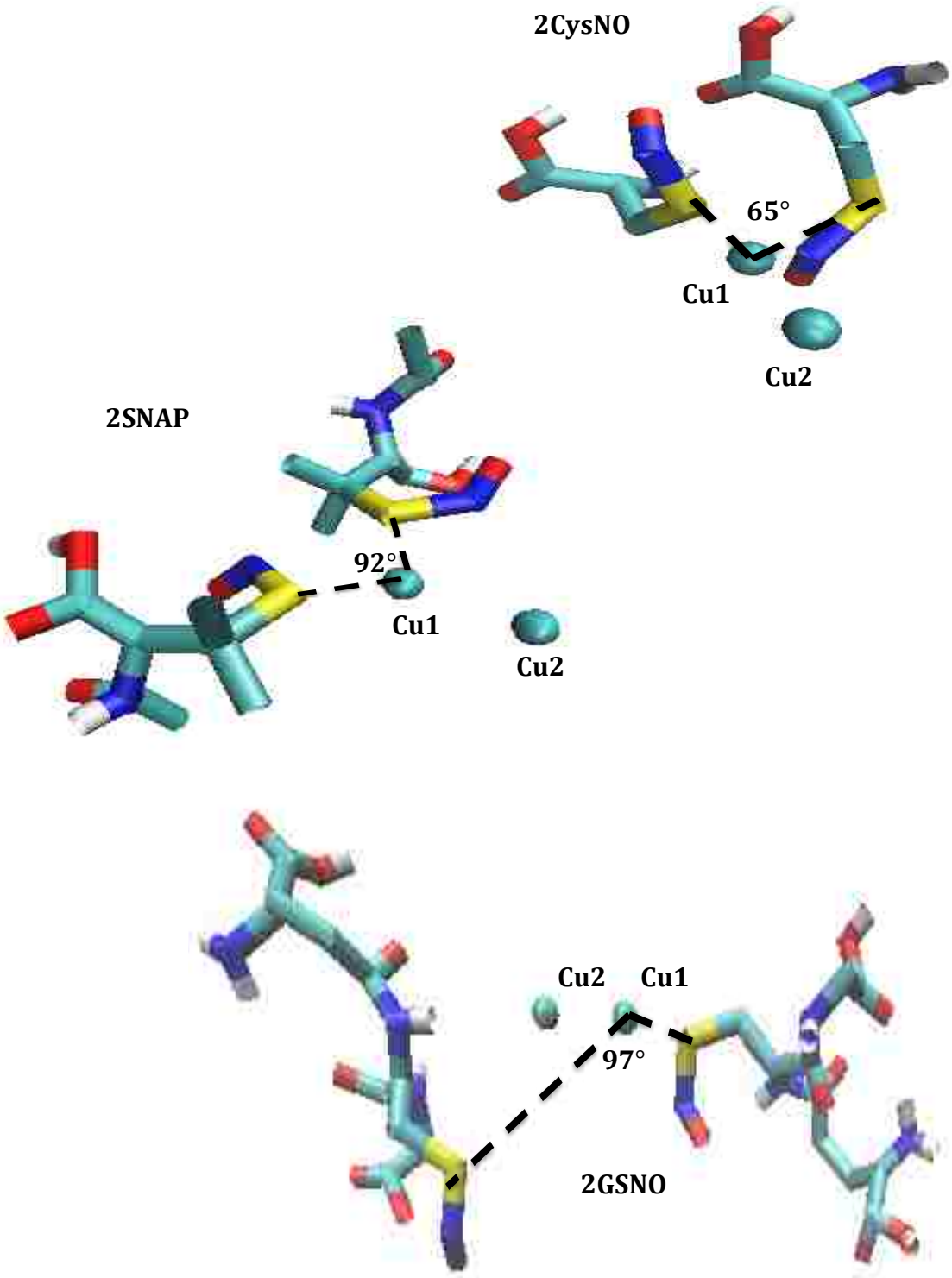

Figure 3.21. Shows the average S_1-Cu-S_2 angle as 2RSNO approaches the MOF bound copper center for (top) M143-2CysNO (middle) M143-2SNAP and (bottom) M143-2GSNO. r_{Cu-S}= ~2.3 Å. The MOF and ethanol molecules are removed for clarity.

adjacent catalytic center provides contrasting free energy profiles for the CPG and GPC systems (Figure 3.22).

To explain the disparity between both systems, visual analysis of the immediate solvation environment suggest that the orientation of GSNO is responsible for these results. CPG-RSNO2 simulations result in GSNO being bound to

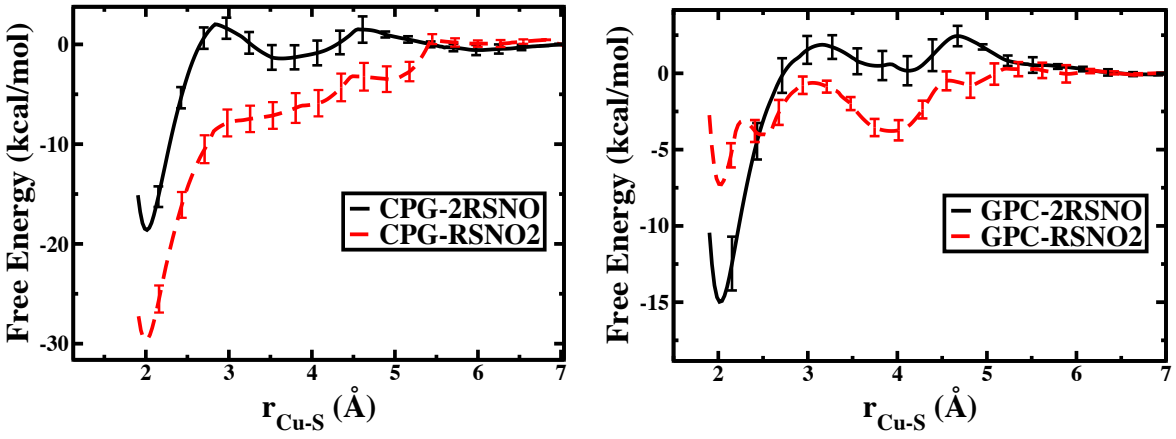

Figure 3.22. Free energy profile for mixed MOF simulations (top) CysNO bound to copper while GSNO (CPG) approaching (bottom) GSNO bound to copper as CysNO (GPC) approaches.

the Cu2 site while CysNO is displaced to approximately 11 Å away from Cu1. Moreover, GPC-RSNO2 simulations show that the distance of GSNO and CysNO are 2.0 Å and 2.5 Å, respectively. It is apparent that GSNOs approach is responsible for CysNO being pushed away as this behavior is also seen in the 2GSNO case. The orders in which these molecules approach the catalytic center are important due to the need for this large molecule to reorient as it approaches the copper center as opposed to it already reconfiguring itself to an orientation that is equilibrated before the arrival of CysNO in GPC-RSNO2 (Figure 3.23). This allows both GSNO and

CysNO to get closer together in the GPC-RSNO2 case and results in a shallower minimum than when GSNO is approaching in CPG-RSNO2 and effectively pushes away the CysNO molecule.

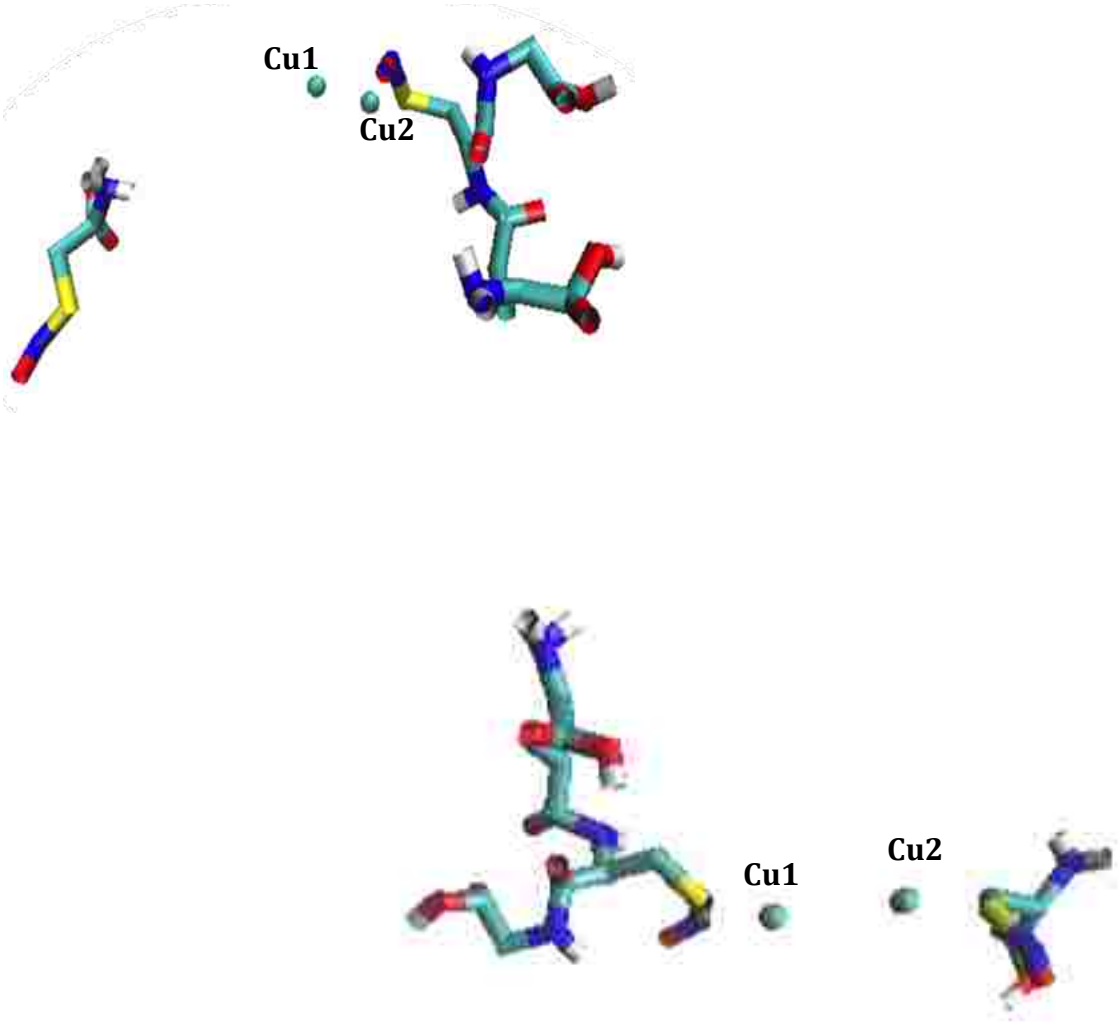

Figure 3.23. Illustrates the orientation of both CysNO and GSNO in the MOF-mixed-RSNO simulation for the RSNO2 scenario. (top) Shows the resulting orientation of CysNO at the copper center (CPG) and GSNO approaching Cu2, the adjacent center, pushing away CysNO. (bottom) Shows the resulting orientation for GSNO at the copper center (GPC) and CysNO approaching Cu2, the adjacent copper. * The MOF and ethanol molecules are removed for clarity

3.4 References

(1) Lehn, J.-M.: From Molecular to Supramolecular Chemistry. In *Supramolecular Chemistry*; Wiley-VCH Verlag GmbH & Co. KGaA, 2006; pp 1-9.

(2) Friesner, R. A. Ab initio quantum chemistry: Methodology and applications. *Proceedings of the National Academy of Sciences of the United States of America* **2005**, *102*, 6648-6653.

(3) Helgaker, T.; Taylor, P. R. Gaussian basis sets and molecular integrals. *Modern Electronic Structure* **1995**.

(4) Liu, L. Z. Q. Y. Q. M. C. Z. J. M. D. A force field for dynamic Cu-BTC metal-organic framework. *J Mol Model* **2010**, *17*, 227-234.

(5) Zhao, L.; Yang, Q.; Ma, Q.; Zhong, C.; Mi, J.; Liu, D. A force field for dynamic Cu-BTC metal-organic framework. *Journal of Molecular Modeling* **2011**, *17*, 227-234.

(6) Yang, Q.; Zhong, C. Molecular Simulation of Carbon Dioxide/Methane/Hydrogen Mixture Adsorption in Metal–Organic Frameworks. *The Journal of Physical Chemistry B* **2006**, *110*, 17776-17783.

(7) Harding, J. L.; Reynolds, M. M. Metal Organic Frameworks as Nitric Oxide Catalysts. *Journal of the American Chemical Society* **2012**, *134*, 3330-3333.

(8) Weinhold, F. Natural bond orbital analysis: A critical overview of relationships to alternative bonding perspectives. *Journal of Computational Chemistry* **2012**, *33*, 2363-2379.

(9) Peng, C.; Bernhard Schlegel, H. Combining Synchronous Transit and Quasi-Newton Methods to Find Transition States. *Israel Journal of Chemistry* **1993**, *33*, 449-454.

(10) Maeda, S.; Harabuchi, Y.; Ono, Y.; Taketsugu, T.; Morokuma, K. Intrinsic reaction coordinate: Calculation, bifurcation, and automated search. *International Journal of Quantum Chemistry* **2015**, *115*, 258-269.

(11) Determining Atomic Charges using the CHELPG Scheme. (accessed March 10 2014).

(12) Zhang, S.; Melzer, M. M.; Sen, S. N.; Çelebi-Ölçüm, N.; Warren, T. H. A motif for reversible nitric oxide interactions in metalloenzymes. *Nat Chem* **2016**, *8*, 663-669.

(13) Frisch, M.; Trucks, G.; Schlegel, H.; Scuseria, G.; Robb, M.; Cheeseman, J.; Montgomery, J.; Vreven, T.; Kudin, K.; Burant, J. Gaussian 03, revision C. 02. **2008**.

(14) Parr, R. G. Density Functional Theory. *Annual Review of Physical Chemistry* **1983**, *34*, 631-656.

(15) Zhao, Y.; Truhlar, D. The M06 suite of density functionals for main group thermochemistry, thermochemical kinetics, noncovalent interactions, excited states, and transition elements: two new functionals and systematic testing of four M06-class functionals and 12 other functionals. *Theor Chem Account* **2008**, *120*, 215-241.

(16) Li, T.; Taylor-Edinbyrd, K.; Kumar, R. A computational study of the effect of the metal organic framework environment on the release of chemically stored nitric oxide. *Physical Chemistry Chemical Physics* **2015**, *17*, 23403-23412.

(17) van Gunsteren, W. F.; Berendsen, H. J. C. Computer Simulation of Molecular Dynamics: Methodology, Applications, and Perspectives in Chemistry. *Angewandte Chemie International Edition in English* **1990**, *29*, 992-1023.

(18) Allen, M. P.; Tildesley, D. J.: *Computer Simulation of Liquids*; Oxford University Press, USA, 1989. pp. Oxford science publications.

(19) Mayo, S. L.; Olafson, B. D.; Goddard, W. A. DREIDING: a generic force field for molecular simulations. *The Journal of Physical Chemistry* **1990**, *94*, 8897-8909.

(20) Kästner, J. Umbrella sampling. *Wiley Interdisciplinary Reviews: Computational Molecular Science* **2011**, *1*, 932-942.

(21) Pronk, S.; Páll, S.; Schulz, R.; Larsson, P.; Bjelkmar, P.; Apostolov, R.; Shirts, M. R.; Smith, J. C.; Kasson, P. M.; van der Spoel, D.; Hess, B.; Lindahl, E. GROMACS 4.5: a high-throughput and highly parallel open source molecular simulation toolkit. *Bioinformatics* **2013**, *29*, 845-854.

(22) Evans, D. J.; Holian, B. L. The Nose–Hoover thermostat. *The Journal of Chemical Physics* **1985**, *83*, 4069-4074.

(23) Melchionna, S.; Ciccotti, G.; Lee Holian, B. Hoover NPT dynamics for systems varying in shape and size. *Molecular Physics* **1993**, *78*, 533-544.

(24) Essmann, U.; Perera, L.; Berkowitz, M. L.; Darden, T.; Lee, H.; Pedersen, L. G. A smooth particle mesh Ewald method. *The Journal of Chemical Physics* **1995**, *103*, 8577-8593.

(25) Furukawa, H.; Go, Y. B.; Ko, N.; Park, Y. K.; Uribe-Romo, F. J.; Kim, J.; O'Keeffe, M.; Yaghi, O. M. Isoreticular Expansion of Metal–Organic Frameworks with Triangular and Square Building Units and the Lowest Calculated Density for Porous Crystals. *Inorganic Chemistry* **2011**, *50*, 9147-9152.

(26) Hanwell, M. D.; Curtis, D. E.; Lonie, D. C.; Vandermeersch, T.; Zurek, E.; Hutchison, G. R.: *Avogadro: an advanced semantic chemical editor, visualization, and analysis platform*, 2012; Vol. 4.

(27) Clingerman, D. J.; Morris, W.; Mondloch, J. E.; Kennedy, R. D.; Sarjeant, A. A.; Stern, C.; Hupp, J. T.; Farha, O. K.; Mirkin, C. A. Stabilization of a highly porous metal-organic framework utilizing a carborane-based linker. *Chemical Communications* **2015**, *51*, 6521-6523.

(28) Furukawa, H.; Cordova, K. E.; O'Keeffe, M.; Yaghi, O. M. The Chemistry and Applications of Metal-Organic Frameworks. *Science* **2013**, *341*.

(29) Kumar, S.; Rosenberg, J. M.; Bouzida, D.; Swendsen, R. H.; Kollman, P. A. The weighted histogram analysis method for free-energy calculations on biomolecules. I. The method. *Journal of computational chemistry* **1992**, *13*, 1011-1021.

(30) Souaille, M.; Roux, B. t. Extension to the weighted histogram analysis method: combining umbrella sampling with free energy calculations. *Computer physics communications* **2001**, *135*, 40-57.

CHAPTER 4. UNDERSTANDING THE ORIGINS OF REGIOSELECTIVITY IN THE FORMATION OF ∝′ FUNCTIONALIZED SILYLENOL ETHERS

4.1 Introduction to Oxyallyl Cations

Natural products are small organic molecules found in nature and typically produced by plants and fungi.[1,2] Alternatively referred to as secondary metabolites, these molecules are not vital components of an organisms essential functions and do not participate in growth, development and reproduction processes like primary metabolites.[3] The wide range of naturally occurring secondary metabolites offers extensive structural and chemical diversities. Although originally assumed to be waste products of living organisms, natural products have become well known and studied in medicinal chemistry.[4]

To differentiate the countless number of natural products, these organic molecules are often split into five groups with the most common being alkaloids and phenols. The *Papaver somniferum* plant is responsible for the generation of morphine, the first discovered alkaloid, commonly utilized as an analgesic.[1] Moreover, caffeine and cocaine are also alkaloids with stimulative properties derived from the cocoa and coca plants, respectively.[5] The hydroxyl group containing phenol class of natural products includes salicylic acid, the active ingredient of the over the counter anti-inflammatory drug aspirin.[6]

Current production of many natural product derived pharmaceutical agents involves their direct use or implements their structures as templates. In addition to their extensive use as antibiotics,[7,8] natural products have also been used in the treatment of hypertension[9] and various cancers.[4] The Penicillium genus of fungi is capable of producing penicillin, an antibiotic, under conditions that inhibit the growth of this fungus in response to stress.[10] In spite of the success of numerous antibiotics, the adaptive properties of these microbes are responsible for the development of resistance and thus a constant supply of efficient antibiotics is needed.[11] Despite the numerous health benefits associated with the use of natural products, the functions of many secondary metabolites remain elusive.

Due to the complexities associated with the structural makeup of natural products, synthetic strategies to fabricate these molecules are desired. Organic chemist have sough to develop novel organic reactions capable of overcoming synthetic challenges often encountered in these complex materials. Of particular interest is the regioselective incorporation of substituted indole molecules to the α positions of unsymmetrical disubstituted ketones to produce enol ether compounds; the success of this methodology harnesses the use of an oxyallyl cation.

Dating back a century ago, the oxyallyl cation was implicated as an intermediate in the ubiquitous Favorskii rearrangement, a synthetic method capable of producing contracted cyclic structures bearing a carboxylate group.[12] Furthermore, the formation of cyclic structures through [4 + 3][13] and [3 + 2][14] cycloadditions is made possible through the use of oxyallyl cations to form seven

and five membered rings, respectively. The production of small organic molecules that mimic natural products requires synthetic routes capable of circumventing problematic chemistries associated with such diverse and complex molecules.

The proven utility of oxyallyl carbocations justifies the use of these intermediates in many natural product synthetic methods. Silylenol ether formation is made possible through the treatment of ketones with trialkylsilyl chlorides in Bronsted bases of varying strength to generate differentiable structures obtained through kinetic or thermodynamic control. While this method works well for monosubstituted ketones, treatment of disubstituted ketones yields a mixture of two regioisomers (Figure 4.1). Although the yield of either isomer can be biased by steric and electronic factors, methods that neglect to extort these biases for

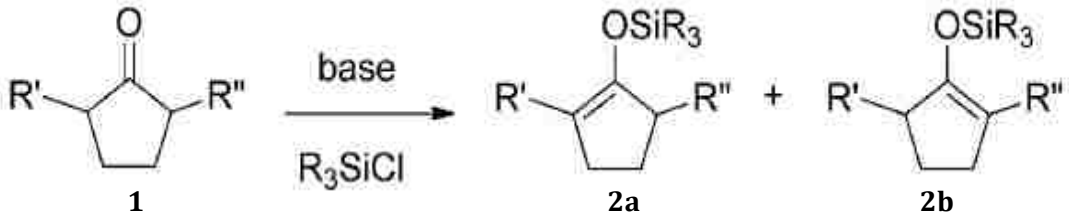

1 **2a** **2b**

Figure 4.1. Treatment of disubstituted ketones with trialkylsilyl chloride to produce silylenol ethers can result in regioisomers 2a and 2b.

regioselectivity are lacking until recently.

Through the use of an oxyallyl carbocation intermediate, Ayala et al. have developed a synthetic route capable of producing silylenol ethers as an exclusive regioisomer at yields reaching 91% (Figure 4.2).[15] Due to concerns of protodesilylation, toluene, a non-polar and non-nucleophilic solvent was used. Moreover, screening of various Bronsted acids including pyridinium tosylate,

pyridinium sulfate and pyridinium triflate was performed. From this work they found that pyridinium triflate was the most efficient generator of the silylenol ether and resulted in no protodesilylation. Synthesis of the enol ether products of this

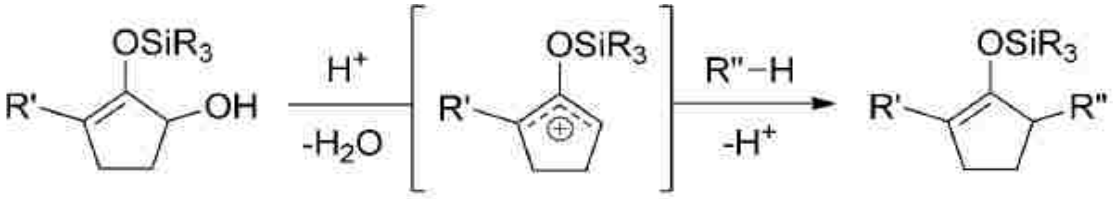

3 **4** **2a**

Figure 4.2. Regioselective control of indole addition through a carbocation intermediate predominately generates isomer 2a for this reaction.

work proceeds through a S_{N1} reaction mechanism (Figures 4.3, 4.4). The first step of this reaction involves the protonation of the leaving group through pyridinium triflate and is referred to as the rate-determining step.[16] This reaction results in the formation of the oxyallyl cation and deprotonated pyridinium triflate. The subsequent, faster step involves the nucleophilic attack of the oxyallyl carbocation by an indole to form the enol ether product. Generation of this product is performed under mild conditions with catalytic amounts of pyridinium triflate.

The synthetic method developed by the Kartika group has shown great success in directing the addition of a substituted indole to the α'-position of a carbocation intermediate. Employment of a silyloxyallyl cation intermediate was reported to produce the silylenol ether regioisomers (2a and 2b) in a 99:1 ratio. Further work was performed to determine the factors responsible for the observed regioselectivity including the probing of indoles with varying steric congestion and

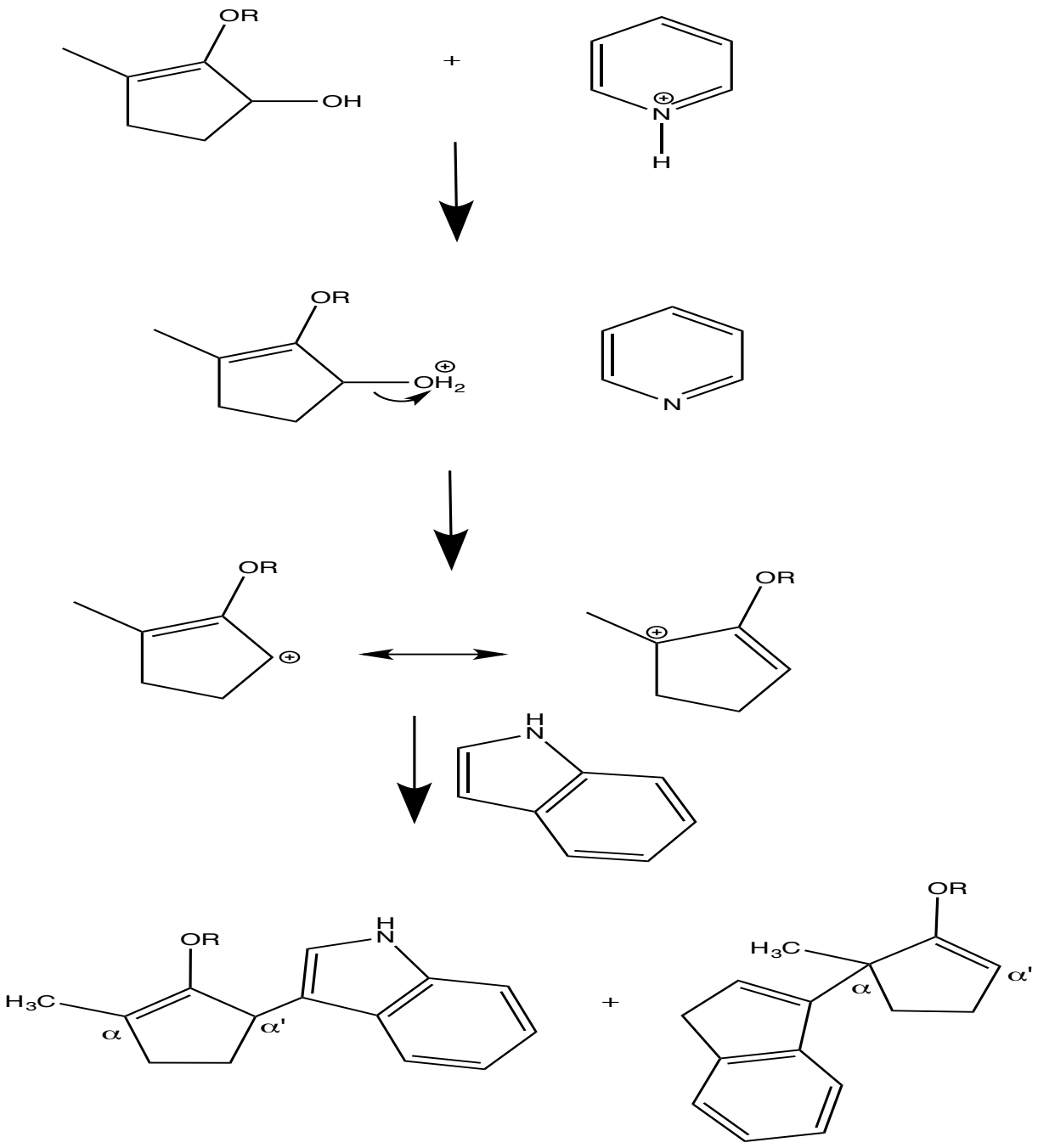

Figure 4.3. The S_{N1} reaction mechanism undergone for the generation of enol ethers where the R-group is either a methyl or silyl group.

electronic properties. Unfortunately, the use of electron poor and/or sterically congested indoles had no substantial effect on the yield of silylenol ether products. As such, results of this work suggest that neither sterics nor electronics play a substantial role in directing the site of nucleophilic addition.

To further investigate origins of regioselectivity in this system, use of a methoxy group attached through the carbonyl is explored. Unlike the

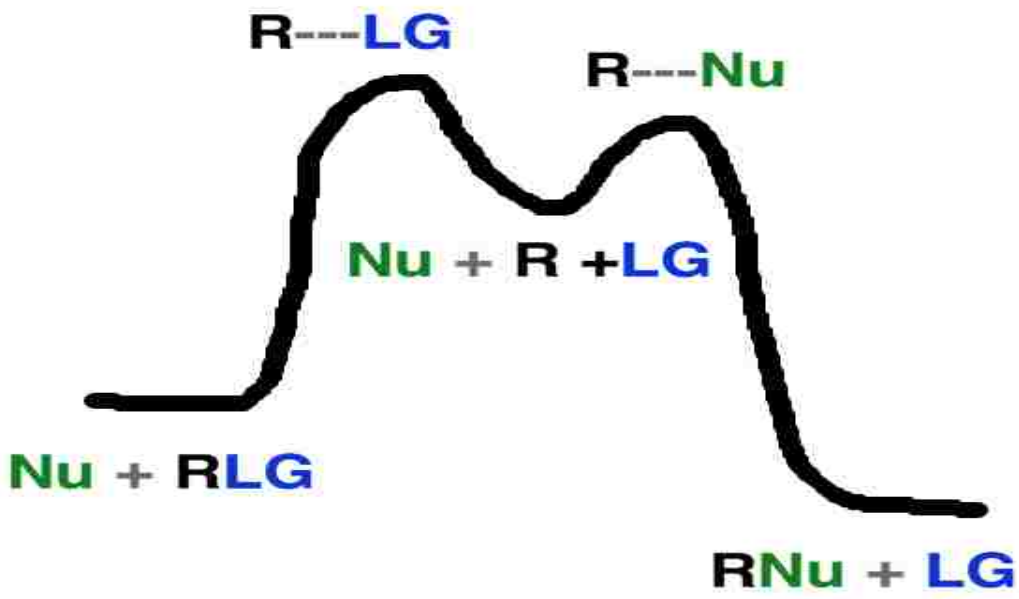

Figure 4.4. Shows the steps associated with the S_{N1} reaction mechanism. The nucleophile does not participate in the first step. Approach of a Bronsted acid results in the first transition state and is the rate-determining step. Complete protonation of the leaving group results in the formation of the carbocation intermediate and leaving group. The subsequent reaction occurs between R and the nucleophile.

regioselectivity observed in silicon containing systems, use of a methoxy group exhibits relatively no bias and produces a nearly racemic mixture of both regioisomers.[15] The disparity of these systems is perplexing and further elicits interest in the overarching goal of determining the factors that drive the selective carbon-carbon nucleophilic addition of an indole to the silyloxyallyl carbocation intermediate. Since steric congestion and electronic effects have been shown experimentally to have negligible effects on the system, it is hypothesized that the inherent chemistries of silicon along with thermodynamic behavior of the system may be responsible for the production of an exclusive regioisomer.

4.2 Computation Methods

The inability of experimental work to indicate key factors responsible for regioselective enol ether formation in silicon containing molecules has led to interest in quantum mechanical methods. As such, solving of the Schrödinger equation is necessary as it provides the wavefunction of system. Electronic structure calculations are performed to obtain the optimized energies of the reactants, products and connecting transition states. Upon retrieval of the transition state using the Synchronously Transit-Guided Quasi-Newton (STQN) methods,[17] frequency calculations of the transition state are used to confirm the presence of only one imaginary frequency. Intrinsic reaction coordinate (IRC) calculations (step size=0.100 $amu^{1/2}$Bohr) validate the connection of a transition state to its appropriate reactant and product. All reactant and products are also subjected to

frequency calculations to verify that no imaginary frequencies exist and that the configuration lies at an energy minimum.

The rate-determining step of the S_{N1} reaction does not depend on the concentration nor nature of the nucleophile, consequently, the indole is only present in steps occurring after the carbocation is generated. It should also be mentioned here that protonation of the hydroxy leaving group results in a molecule of water; in all subsequent steps the water molecule remains with the system at a non-bonding distance. Starting configurations are obtained based on experimentally reported structures and used for geometry optimizations. All calculations are performed using the Gaussian09 *ab initio* software package[18] at the DFT level of theory[19] in conjunction with the B3LYP functional and the 6-31+(d) basis set. Furthermore, each calculation was performed using a polarizable continuum model (PCM) to mimic a toluene solvent (ε=2.3741). Due to the nature of the charge containing system, Grimme's dispersion correction method[20] was implemented.

4.3 Results and Discussion

The starting material is composed of either a methoxy or alkylsilyl substituted ketone containing a hydroxy group that is protonated by the pyridinium triflate. Before complete protonation of the leaving group the system passes through a transition state verified through the presence of one imaginary frequency at 106.08 cm^{-1} and 127.49 cm^{-1} for the methoxy and silyl containing systems, respectively. The activation energy of this reaction is calculated as 20.26 kcal mol^{-1}

and 18.49 kcal mol^{-1} for the methoxy and silyl groups, respectively (Figures 4.5, 4.6). Movement downhill in energy converts the transition states into their respective carbocation intermediates and deprotonated pyridinium triflate molecule. The products of this reaction are located uphill from the starting reactants due to the unfavorable energy associated with the proton transfer from the weak acid to the poor leaving group.

The next state of the system involves the carbocation intermediate, with water and indole as starting materials. The system proceeds through a transition state corresponding to the nucleophilic attack of the oxyallyl cation at either α position. While this subset of reactions is dependent on the behavior of the nucleophile, various orientations of the indole were probed; only the lowest energy configurations are adopted throughout. NBO analysis of each carbocation shows the positive charge delocalized unevenly across three carbons. The largest concentration of positive charge is located at the α position of the oxyallyl carbocation validating the existence of the more stable tertiary carbocation.

4.3.1. Methoxy-Oxyallyl Cation. The indole configuration of both methoxy moieties adopts what is referred to as the ring up orientation where the nitrogen is pointing towards the top of the carbocation (Figure 4.7). The transition state energy is 3.64 and 3.05 kcal mol^{-1} for the nucleophilic attack at the α and α' sites of the methoxy-oxyallyl cation, respectively. The transition states were located by sole imaginary frequencies at 226.29 cm^{-1} for indole addition at the α site and 246.94 cm^{-1} at the α' site. Unlike the slower, rate determining step of the S_{N1} reaction, this step occurs faster and sees a smaller energetic barrier. The final

Table 4.1. Rxn1 shows the formation of the methoxy-oxyallyl carbocation in kcal mol^{-1}

	Methoxy Group
SM	0
TS	20.26
Prdt 1	17.49

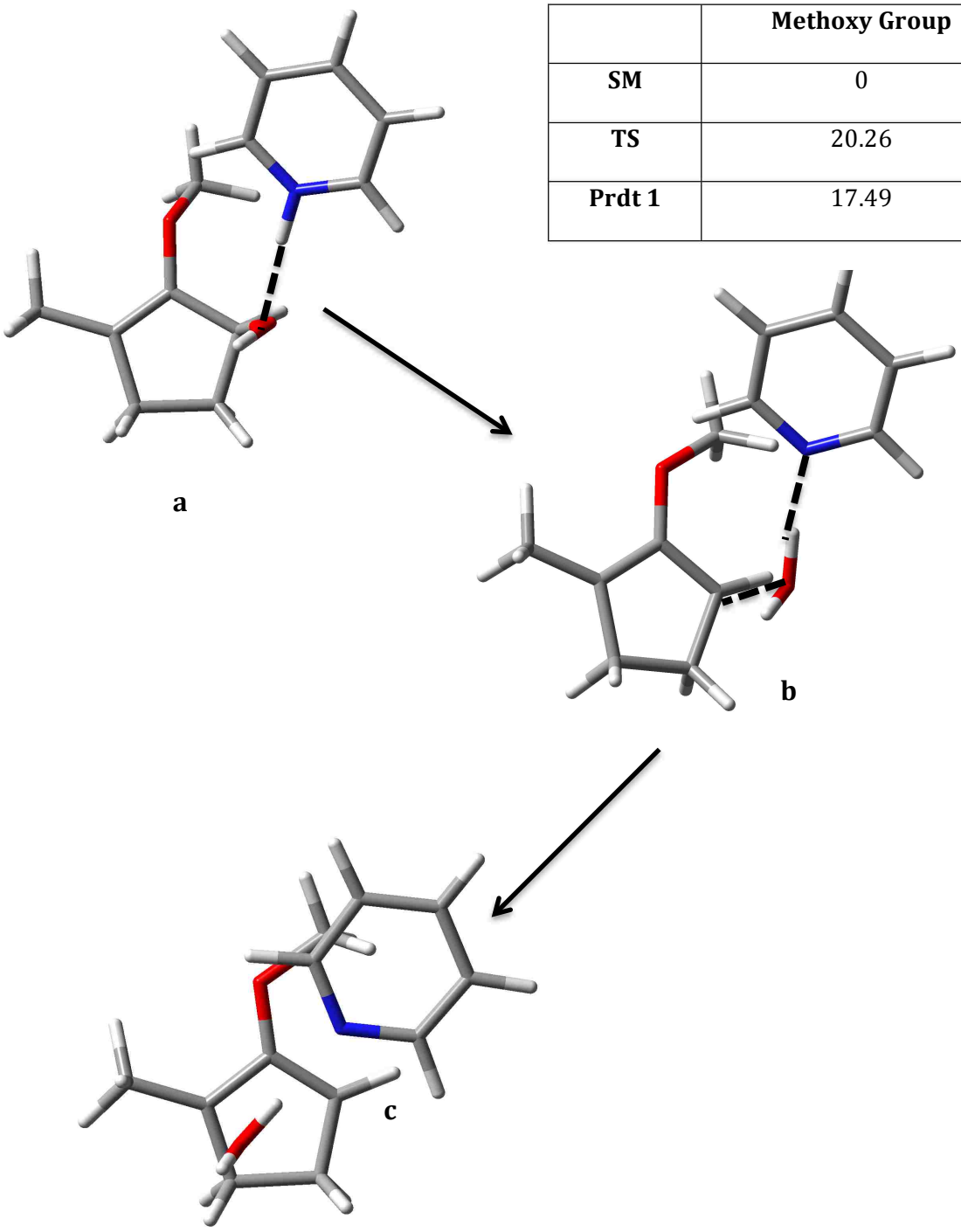

Figure 4.5. shows the protonation of the leaving group with the pyridinium triflate catalyst to generate a carbocation intermediate. (a) starting material (b) transition state (c) methoxy-oxyallyl carbocation. Energies reported in kcal mol^{-1}

Table 4.2. Rxn1 shows the formation of the silyl-oxyallyl carbocation

	Silyl Group
SM	0
TS	18.49
Prdt 1	15.72

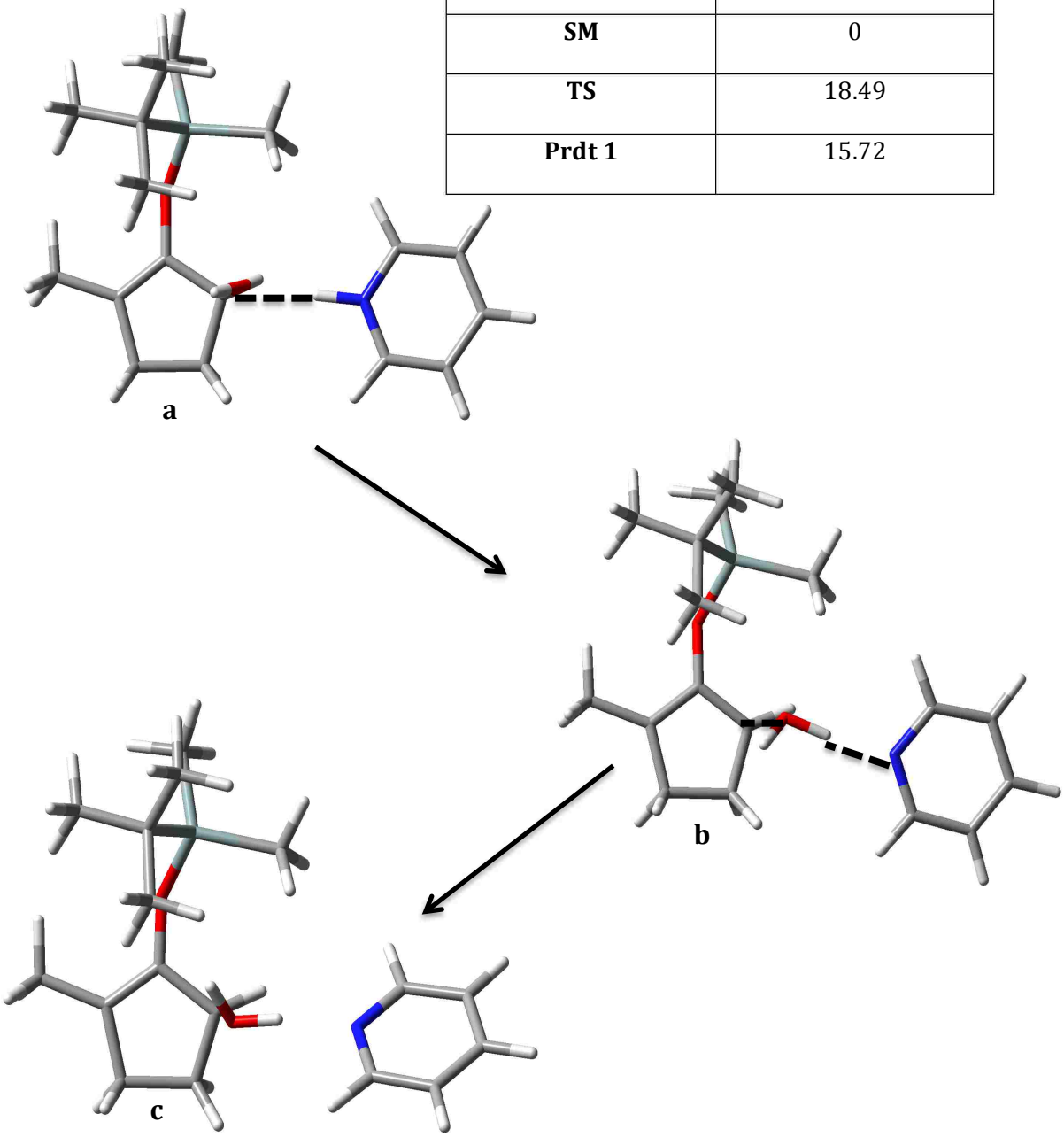

Figure 4.6. shows the protonation of the leaving group with the pyridinium triflate catalyst to generate a carbocation intermediate. (a) starting material (b) transition state (c) silyloxyallyl carbocation. Energies reported in kcal mol^{-1}

products of this reaction are calculated as -5.00 and -5.70 kcal mol^{-1} for the α and α' positions, respectively, showing that the energies of these reactions are relatively close to one another (Figures 4.8, 4.9).

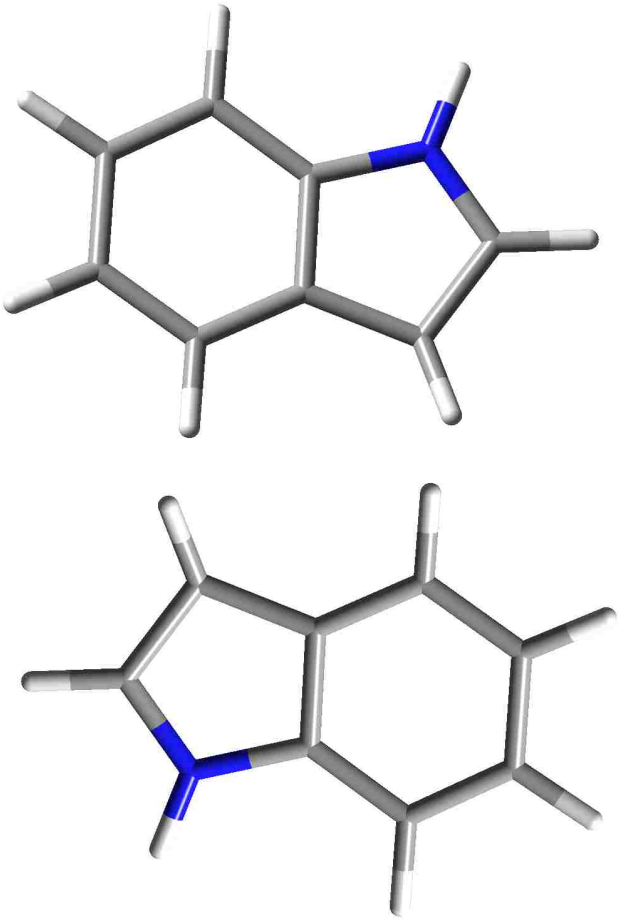

Figure 4.7. The indole can take on many configurations. The ring up orientation (top) has the nitrogen atom point up as opposed to the (bottom) ring down configuration.

4.3.2. Silyloxyallyl Cation.

Unlike the nature of the methoxy containing enol ether molecules, the indole orientation changes to a ring down and ring up position for the α and α' positions of the silyloxyallyl intermediate, respectively (Figure 4.7). Indole addition at the α position shows that both the ring up and ring down products differ by less than one kcal mol^{-1} but both configurations pass through relatively high transition states of 41 and 43.88 kcal mol^{-1}, respectively. The product energy was calculated as -6.02 kcal mol^{-1} (Figure 4.10). In contrast, nucleophilic addition at the α' position shows a difference of approximately 4kcal mol^{-1} between the ring up and ring down configurations. Electronic structure calculations show the ring up configuration as the most favorable at the α' site; this is also observed with the methoxy species. Further

Table 4.3. Rxn2 shows the formation of the ∝-methoxy-oxyallyl carbocation

∝-Carbon	**Methoxy Group**
Prdt1	0
TS2	3.64
Prdt 2	-5.00

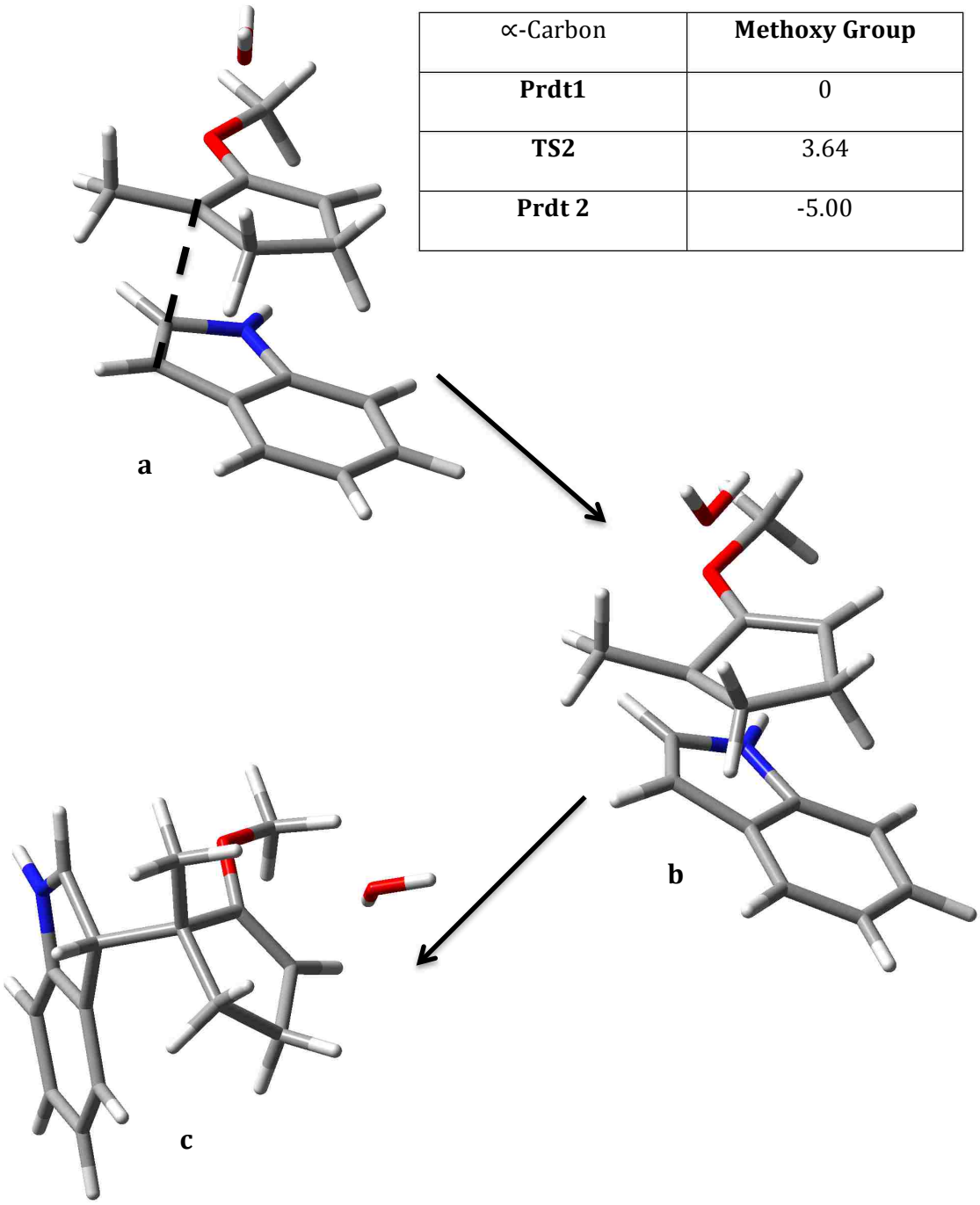

Figure 4.8. shows the protonation of the leaving group with the pyridinium triflate catalyst to generate a carbocation intermediate. (a) carbocation product 1 with indole (b) transition state 2 (c) ∝-functionalized silylenol ether. Energies reported in kcal mol^{-1}

Table 4.4. Rxn2 shows the formation of the ∝ ′-methoxy-oxyallyl carbocation

∝ ′-Carbon	**Methoxy Group**
Prdt1	0
TS2	3.05
Prdt 2	-5.70

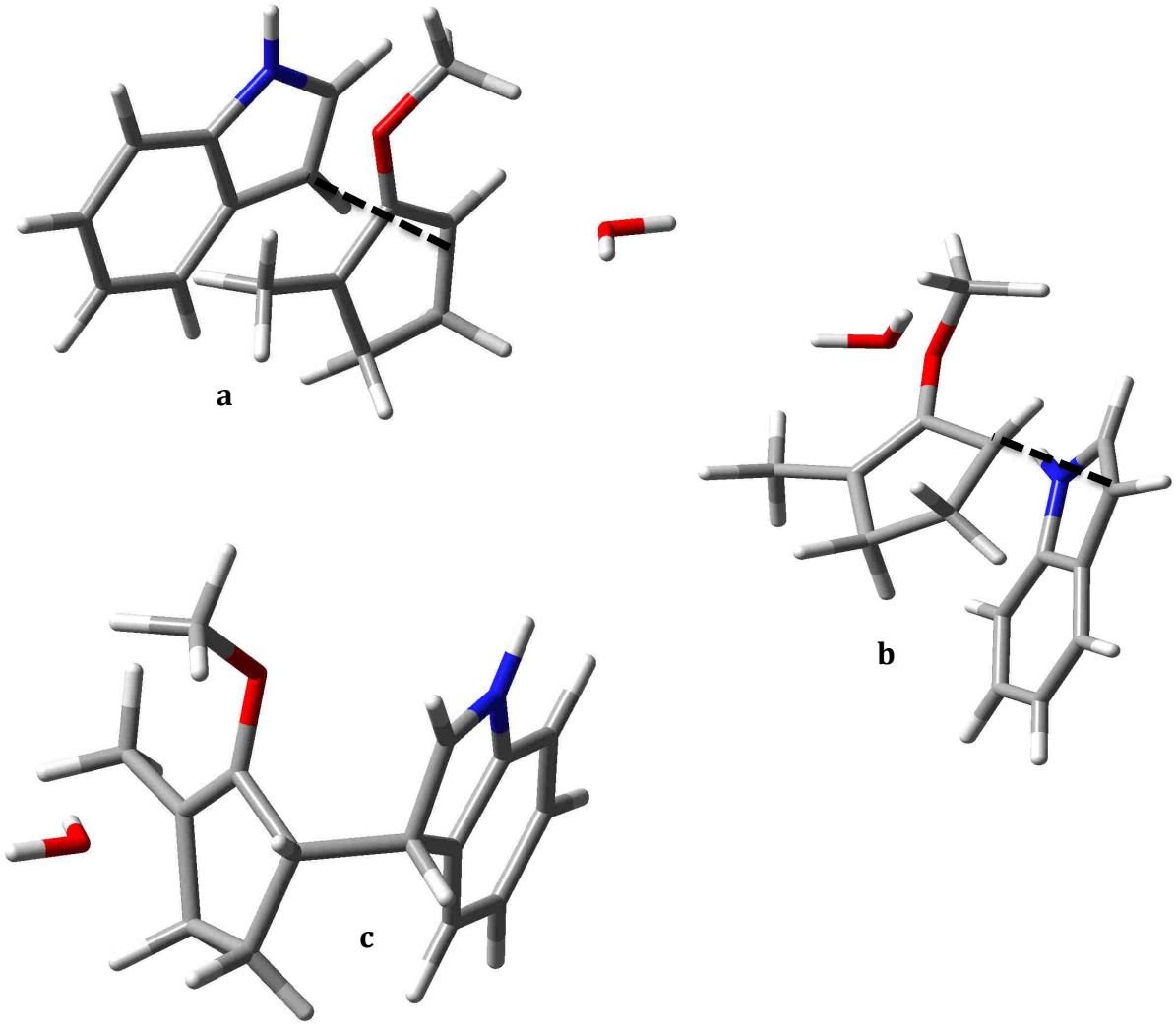

Figure 4.9. shows the protonation of the leaving group with the pyridinium triflate catalyst to generate a carbocation intermediate. (a) carbocation product 1 with indole (b) transition state 2 (c) ∝ ′-functionalized silylenol ether. Energies reported in kcal mol^{-1}

Table 4.5. Rxn2 shows the formation of the ∝-silyloxyallyl carbocation

∝-Carbon	**Silyl Group**
Prdt1	0
TS2	43.88
Prdt 2	-6.02

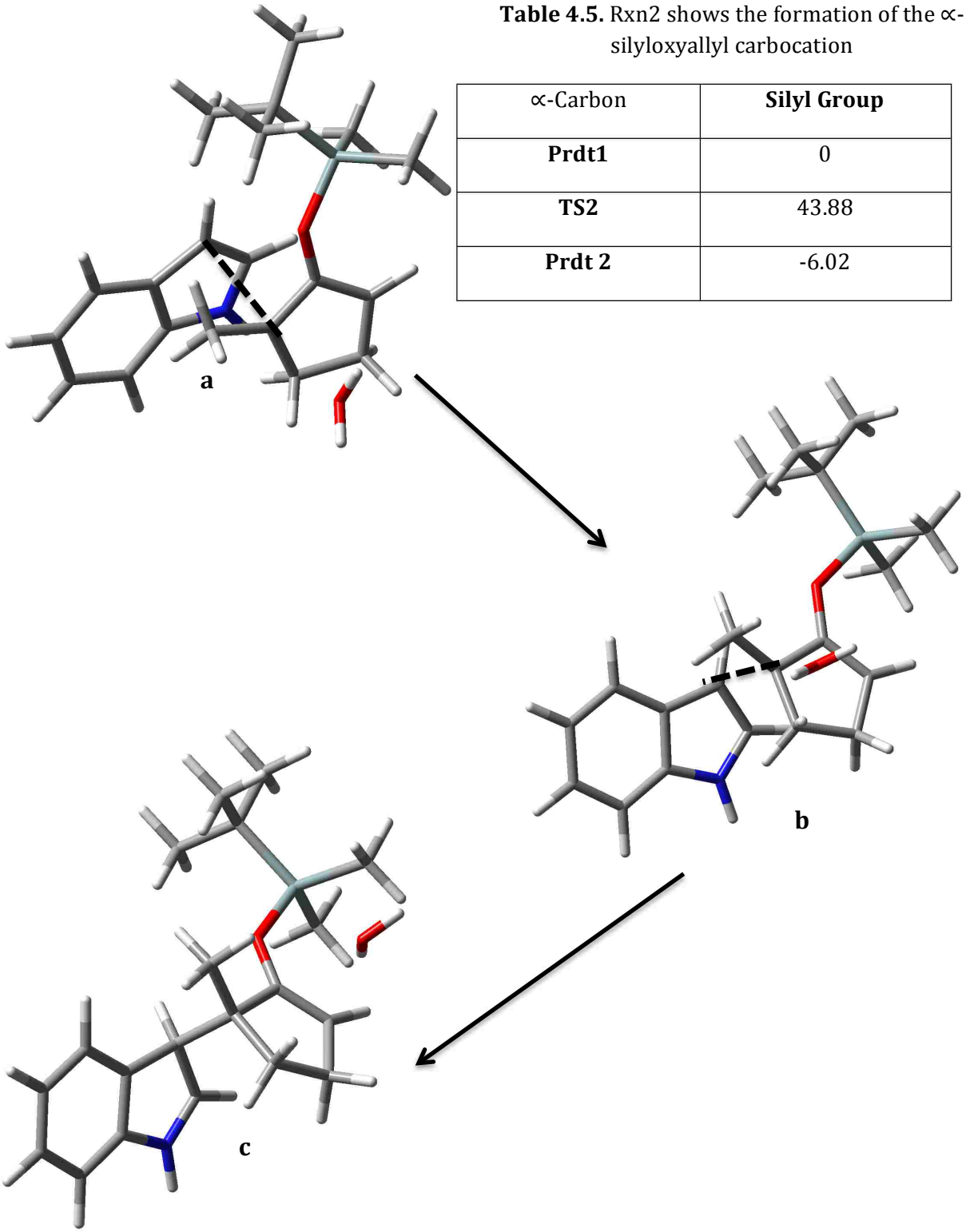

Figure 4.10. shows the protonation of the leaving group with the pyridinium triflate catalyst to generate a carbocation intermediate. (a) carbocation product 1 with indole (b) transition state 2 (c) ∝-functionalized silylenol ether. Energies reported in kcal mol^{-1}

probing of the system reveals the transition state is nearly barrier-less and also results in a product energy of -8.96 kcal mol^{-1} (Figure 4.11). Electronic structure calculations show that indole addition at the α' position is favored both kinetically and thermodynamically. It is a reasonable presumption that increases in temperature could be used to overcome the energetic barrier of addition at the less favorable α position, unfortunately, the delicacy of this system results in a decomposition of the starting materials upon heating.

Although thermodynamic properties of the system can be employed to validate experimental findings, a thorough explanation is needed to understand the root cause of energy differences in each system. When taking into account the energy difference of 0.70 and 3.00 kcal mol^{-1} for the methoxy-oxyallyl and silyloxyallyl cations, respectively, it is apparent that the energy difference is more than four times higher for silyl containing systems. Scrutiny of the optimized geometries provides insight into the driving forces of regioselectivity for this system. Analysis of the transition state configuration shows immediate differences in structure for silylenol ether formation that is absent in the case of methoxyenol ethers.

The orientation of the oxyallyl cations and indole are visually analyzed for each transition state. When compared to the carbocation, the indole is located out of plane for each system (Figures 4.12, 4.13) except at the favorable α' location of the silyl group (Figure 4.14). The in plane orientation of the indole may stabilize the energy of this transition state by maximizing the overlap between orbitals that are pointed directly at one another, allowing this favorable product to be formed more easily. The out of plane indole configuration for silylenol ether formation at the unfavorable α site appears to suffer from decreased overlap as the ring appears to be pushed out of the plane as seen in figure 10 to compensate for steric congestion. Furthermore, the C1-O-Si bond lies within the plane for

Table 4.6. Rxn2 shows the formation of the ∝'-silyloxyallyl carbocation

∝'-Carbon	**Silyl Group**
Prdt1	0
TS2	0.438
Prdt 2	-8.96

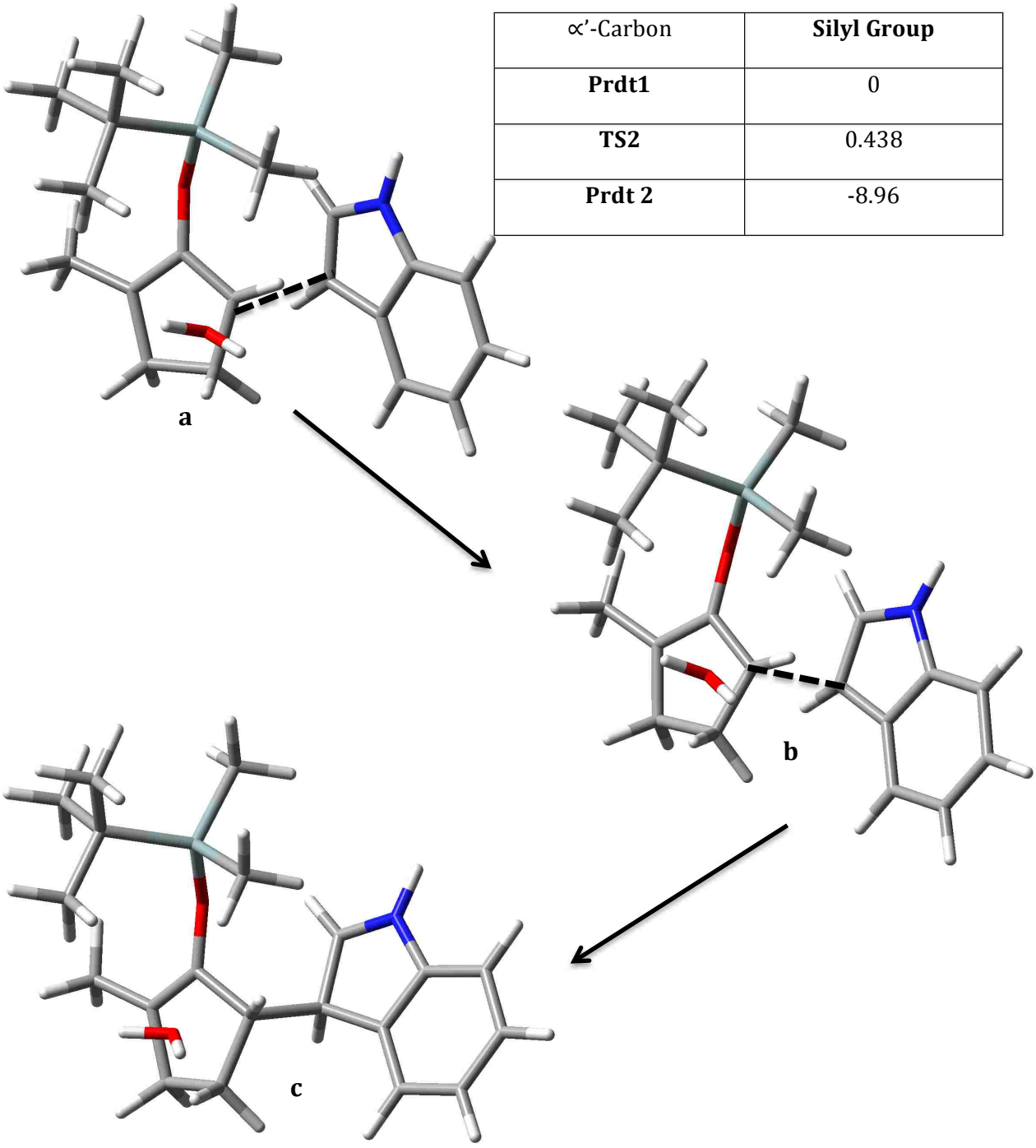

Figure 4.11 shows the protonation of the leaving group with the pyridinium triflate catalyst to generate a carbocation intermediate. (a) carbocation product 1 with indole (b) transition state 2 (c) ∝ ′-functionalized silylenol ether. Energies reported in kcal mol^{-1}

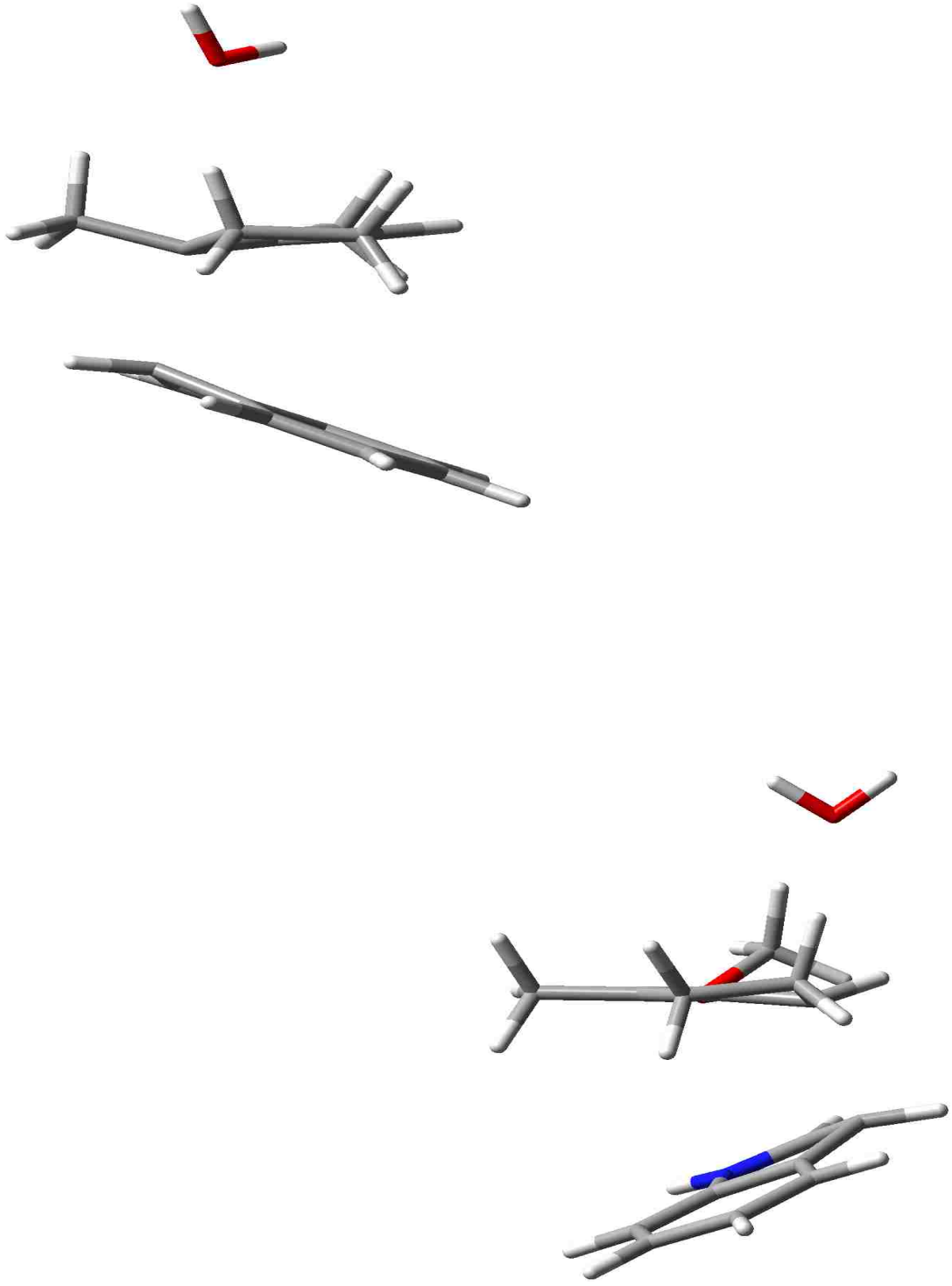

Figure 4.12. The methoxy-oxyallyl cation transition states for indole addition at the (top left) α and (bottom right) α' carbons shows the nucleophile is out of plane.

the silyloxyallyl cation at this α site, a likely result of significant delocalization. Although the delocalization experienced in this system should cause minimization of the system energy, the effects of sterics dominate and prohibit further minimization of the energy to yield a favorable product.

To better understand the electron distribution of these molecules NBO analysis was performed. Results of the NBO analysis show the presence of double bond character between C7 and its neighboring nitrogen in the methyl containing carbocation systems and the unfavorable silyloxyallyl carbocation (Figure 4.15). In contrast, the α' (silyl group)

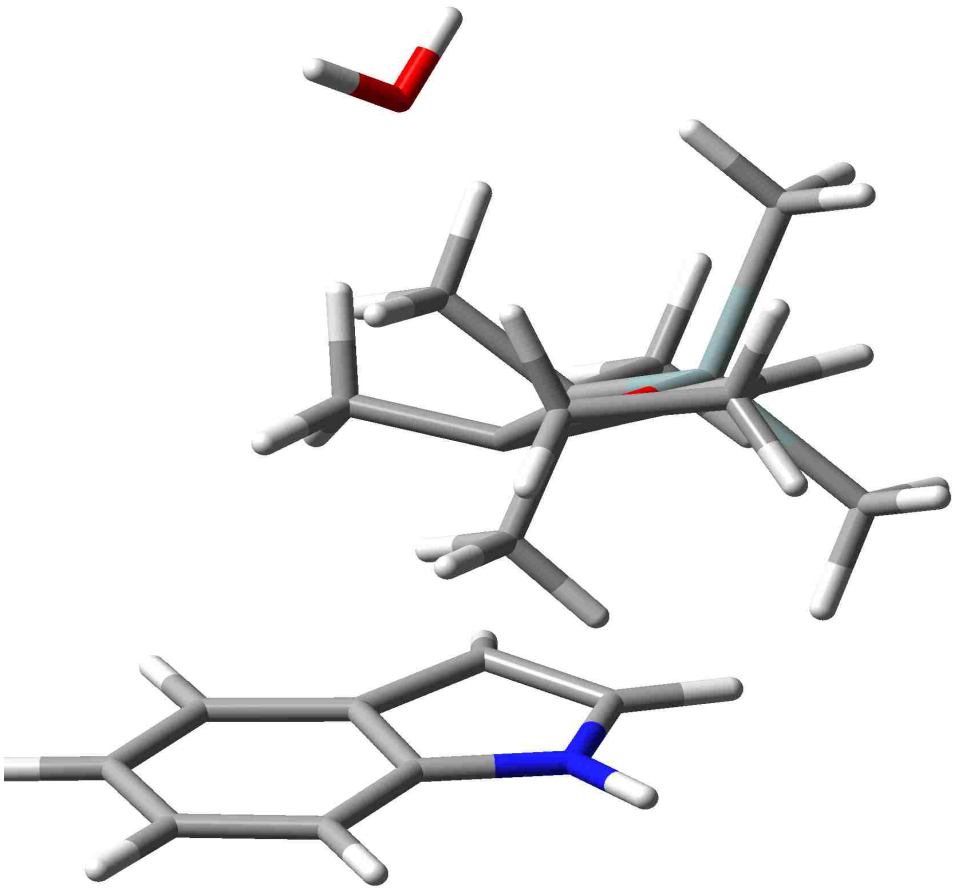

Figure 4.13. The transition state for indole addition at the α site of the silyloxyallyl cation shows that the indole ring is oriented out of the plane. The overlap of these orbitals may be poor due to the their orientation.

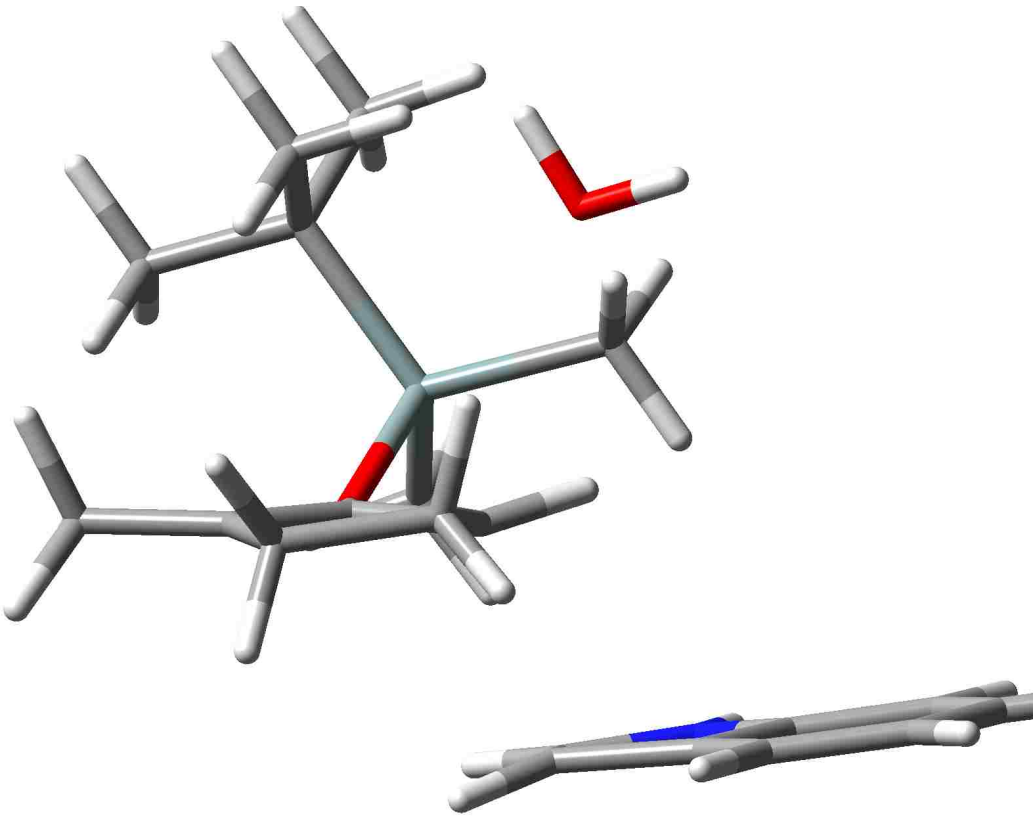

Figure 4.14. The transition state corresponding to the indole addition at the α' carbon of the silyloxyallyl carbocation is within the plane. The in-plane orientation of the indole ring suggests that maximum overlap between the p-orbitals of the carbocation and indole can occur, potentially stabilizing the transition state energy.

transition state exhibits no double bond between carbon and nitrogen atoms; intriguingly, a double bond is observed between C7-C8 as labeled in Figure 4.15.

The computational work herein has provided invaluable insight into the origins of regioselectivity for the direct nucleophilic addition to silyloxyallyl cation intermediates. Through use of electronic structure calculations it is suggested that the generation of an exclusive regioisomer is due in part to the thermodynamic properties of the system resulting from multiple factors including orbital overlap and steric contributions stemming from molecular orientation. The interesting chemistries set forth by the Kartika group

portrays unprecedented synthetic methods capable of producing structurally complex organic molecules inspired by natural products.

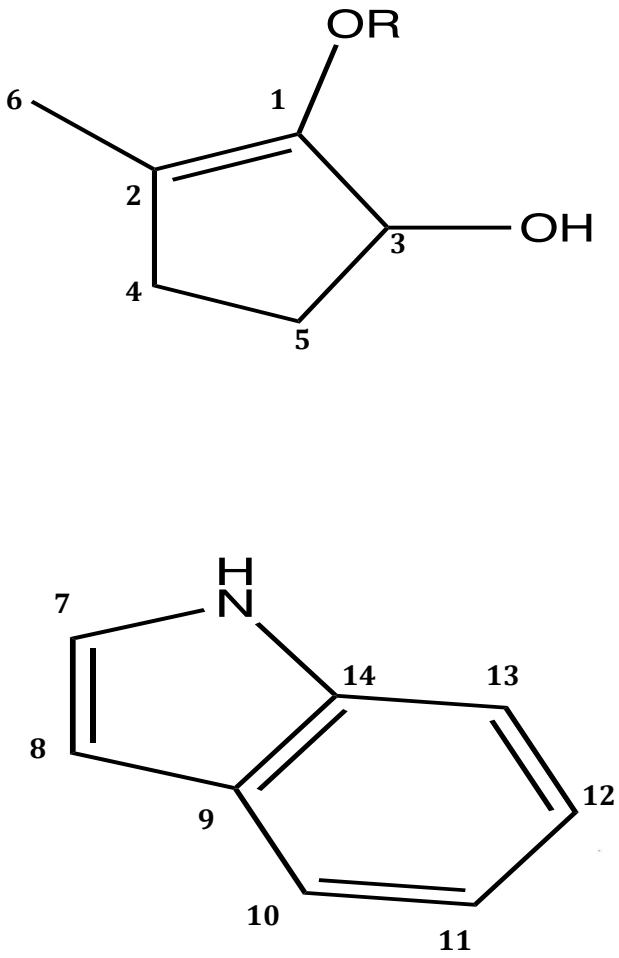

Figure 4.15. The carbon atoms of the (top) oxyallyl cation and (bottom) indole are labeled for reference.

4.4 References

(1) Balandrin, M. F.; Kinghorn, A. D.; Farnsworth, N. R.: Plant-Derived Natural Products in Drug Discovery and Development. In *Human Medicinal Agents from Plants*; ACS Symposium Series 534; American Chemical Society, 1993; Vol. 534; pp 2-12.

(2) Gunatilaka, A. A. L. Natural Products from Plant-Associated Microorganisms: Distribution, Structural Diversity, Bioactivity, and Implications of Their Occurrence. *Journal of Natural Products* **2006**, *69*, 509-526.

(3) Dias, D. A.; Urban, S.; Roessner, U. A Historical Overview of Natural Products in Drug Discovery. *Metabolites* **2012**, *2*, 303.

(4) Newman, D. J.; Cragg, G. M. Natural Products as Sources of New Drugs over the Last 25 Years. *Journal of Natural Products* **2007**, *70*, 461-477.

(5) Croteau, R.; Kutchan, T. M.; Lewis, N. G. Natural products (secondary metabolites). *Biochemistry and molecular biology of plants* **2000**, *24*, 1250-1319.

(6) Hayat, S.; Ali, B.; Ahmad, A.: Salicylic Acid: Biosynthesis, Metabolism and Physiological Role in Plants. In *Salicylic Acid: A Plant Hormone*; Hayat, S., Ahmad, A., Eds.; Springer Netherlands: Dordrecht, 2007; pp 1-14.

(7) Butler, M. S. The Role of Natural Product Chemistry in Drug Discovery. *Journal of Natural Products* **2004**, *67*, 2141-2153.

(8) Butler, M. S.; Buss, A. D. Natural products — The future scaffolds for novel antibiotics? *Biochemical Pharmacology* **2006**, *71*, 919-929.

(9) Cragg, G. M.; Newman, D. J.; Snader, K. M. Natural Products in Drug Discovery and Development. *Journal of Natural Products* **1997**, *60*, 52-60.

(10) Kozlovskii, A. G.; Zhelifonova, V. P.; Antipova, T. V. Fungi of the genus Penicillium as producers of physiologically active compounds (Review). *Applied Biochemistry and Microbiology* **2013**, *49*, 1-10.

(11) Silva, L. N.; Zimmer, K. R.; Macedo, A. J.; Trentin, D. S. Plant Natural Products Targeting Bacterial Virulence Factors. *Chemical Reviews* **2016**, *116*, 9162-9236.

(12) Silva Jr, L. F. Construction of cyclopentyl units by ring contraction reactions. *Tetrahedron* **2002**, *58*, 9137-9161.

(13) Vander Wal, M. N.; Dilger, A. K.; MacMillan, D. W. C. Development of a generic activation mode: nucleophilic [small alpha]-substitution of ketones via oxy-allyl cations. *Chemical Science* **2013**, *4*, 3075-3079.

(14) Li, H.; Wu, J. (3+2)-Cycloaddition Reactions of Oxyallyl Cations. *Synthesis* **2015**, *47*, 22-33.

(15) Ayala, C. E.; Dange, N. S.; Fronczek, F. R.; Kartika, R. Brønsted Acid Catalyzed α′-Functionalization of Silylenol Ethers with Indoles. *Angewandte Chemie* **2015**, *127*, 4724-4728.

(16) Liu, C.; Oblak, E. Z.; Vander Wal, M. N.; Dilger, A. K.; Almstead, D. K.; MacMillan, D. W. C. Oxy-Allyl Cation Catalysis: An Enantioselective Electrophilic Activation Mode. *Journal of the American Chemical Society* **2016**, *138*, 2134-2137.

(17) Peng, C.; Bernhard Schlegel, H. Combining Synchronous Transit and Quasi-Newton Methods to Find Transition States. *Israel Journal of Chemistry* **1993**, *33*, 449-454.

(18) Frisch, M. J.; Trucks, G. W.; Schlegel, H. B.; Scuseria, G. E.; Robb, M. A.; Cheeseman, J. R.; Scalmani, G.; Barone, V.; Mennucci, B.; Petersson, G. A.; Nakatsuji, H.; Caricato, M.; Li, X.; Hratchian, H. P.; Izmaylov, A. F.; Bloino, J.; Zheng, G.; Sonnenberg, J. L.; Hada, M.; Ehara, M.; Toyota, K.; Fukuda, R.; Hasegawa, J.; Ishida, M.; Nakajima, T.; Honda, Y.; Kitao, O.; Nakai, H.; Vreven, T.; Montgomery Jr., J. A.; Peralta, J. E.; Ogliaro, F.; Bearpark, M. J.; Heyd, J.; Brothers, E. N.; Kudin, K. N.; Staroverov, V. N.; Kobayashi, R.; Normand, J.; Raghavachari, K.; Rendell, A. P.; Burant, J. C.; Iyengar, S. S.; Tomasi, J.; Cossi, M.; Rega, N.; Millam, N. J.; Klene, M.; Knox, J. E.; Cross, J. B.; Bakken, V.; Adamo, C.; Jaramillo, J.; Gomperts, R.; Stratmann, R. E.; Yazyev, O.; Austin, A. J.; Cammi, R.; Pomelli, C.; Ochterski, J. W.; Martin, R. L.; Morokuma, K.; Zakrzewski, V. G.; Voth, G. A.; Salvador, P.; Dannenberg, J. J.; Dapprich, S.; Daniels, A. D.; Farkas, Ö.; Foresman, J. B.; Ortiz, J. V.; Cioslowski, J.; Fox, D. J.: Gaussian 09. Gaussian, Inc.: Wallingford, CT, USA, 2009.

(19) Becke, A. D. Density-functional thermochemistry. III. The role of exact exchange. *The Journal of Chemical Physics* **1993**, *98*, 5648-5652.

(20) Grimme, S.; Antony, J.; Ehrlich, S.; Krieg, H. A consistent and accurate ab initio parametrization of density functional dispersion correction (DFT-D) for the 94 elements H-Pu. *The Journal of Chemical Physics* **2010**, *132*, 154104.

CHAPTER 5. CONCLUSIONS AND OUTLOOK

5.1. Metal Organic Frameworks

The focus of this investigation was to reveal the chemical processes associated with the catalytic release of nitric oxide from its RSNO precursors in the presence of the complex MOF environment. As described in Chapter 2, *ab initio* calculations were performed to elucidate the role of the thiol as it has been implicated in the reduction of Cu(II) to the catalytically active Cu(I) species.[1,2] Optimization of the simplified RSNO, CH_3SNO shows that the coordinate-like bond between Cu(I) and sulfur results in an elongation of the sulfur-nitrogen bond and a simultaneous decrease in the bond distance of nitrogen-oxygen as reported by Wu and Meyerhoff.[3] These results indicate the imminent cleavage of the sulfur-nitrogen bond to generate nitric oxide. Consequently, the Cu(I)-S bond distance is taken to be the reaction coordinate of this work.

Classical MD simulations provided insight into how the environment around the catalytic center affects the approach of various RSNO species. In order to probe this system, an in-house force field was derived (Chapter 2) by fitting model energies to interaction energies obtained through electronic structure calculations on representative clusters. Although previous work suggested that changes in the R-group and pore diameter were capable of predicting the barriers associated with the approach of an RSNO to the Cu(I) site,[4] currently unpublished work by Edinbyrd, Li and Kumar indicated that these factors alone are insufficient for predicting these

outcomes. Four RSNOs (CH_3SNO, CysNO, SNAP and GSNO) were investigated in the presence of HKUST-1 and MOF-143 where the free energy is compared to the free copper ion/ethanol solution.

Although the 1RSNO cases depict little to no barrier for CH_3SNO, CysNO and SNAP within HKUST-1, the incorporation of an additional RSNO results in large free energy barriers. In contrast, 1GSNO within HKUST-1 produces large barriers similar to 2RSNO that support the lack of nitric oxide production reported by Hardin et al.[5] The desire to study GSNO in the presence of a complex MOF environment necessitates a MOF with a larger pore diameter like that of MOF-143. Despite CysNO and SNAP following the free energy trends of CH_3SNO in MOF-143, the approach of a second GSNO is dissimilar. 2GSNO immediately pushes away the initial GSNO resulting in a low barrier nearly identical to the 1GSNO case. In contrast, the approach of a second GSNO2 to the adjacent copper shows a significant barrier akin to the barriers seen in the 2RSNO cases of CH_3SNO, CysNO and SNAP.

Multiple reaction rates are suggested as a result of the various free energy barriers encountered, corresponding to the many ways in which RSNO can approach the catalytic centers, namely at the Cu1 and adjacent Cu2 sites. Regardless of whether changes in R-group and pore diameters can accurately predict free energy barriers and their trends, previous and current work suggests that the release rates of RSNO can be modulated through these factors. Information obtained from this work can be utilized to optimize nitric oxide releasing nanomaterials for the purpose of fabricating drug delivery vehicles with targeted release rates.

Although complete quantum mechanical treatment of this system is ideal, it is intractable for a system of this size to be studied along the relevant time scales needed. Beyond the scope of this work is the implementation of reactive force fields capable of depicting the breaking and forming of bonds needed to observe the release of nitric oxide from its RSNO precursor. While this study has focused on RSNO approach, the first step in the catalytic process that releases nitric oxide, further insight into the processes that occur during nitric oxide release are of interest.

5.2. Oxyallyl Cations

Understanding the origins of regioselectivity in the nucleophilic attack of a silyloxyallyl cation was the main goal of this work. The addition of an indole to the oxyallyl carbocation is the result of an S_{N1} reaction mechanism that commences with the protonation of a hydroxy group by pyridinium triflate, a weak Bronsted acid.[6] Through electronic structure calculations, critical thermodynamic information of this system was obtained and compared to the case of a methoxy-oxyallyl cation that displays effectively no regioselectivity. From the work described in Chapter 4, it is suggested that the isolation of a single regioisomer is the result of energy barriers over 87 times that of k_BT upon the approach of an indole to the α position of a silyloxyallyl cation as opposed to a nearly barrierless approach to the α' position. Furthermore, the relative energy obtained for the exclusive regioisomer is 3 kcal

mol^{-1} more favorable, thus making this single isomer the kinetic and thermodynamic product of this reaction.

To further comprehend the highly selective nature of this reaction, NBO analysis was performed on the transition state corresponding to both α sites of the silyl and methoxy containing carbocations. It was determined that the indole ring contains double bond character between the nitrogen atom and the carbon responsible for forming the linkage to the oxyallyl carbocation in all cases except for the barrier less transition state for indole addition at the α' site of the silyloxyallyl cation. Although the significance of this revelation has yet to be determined, visual analysis of these transition states provides further justification for the calculated energies and experimentally observed regioselectivity.

Comparison of indole addition at the α and α' sites of the silyloxyallyl cation shows differences in the orientation adopted by the indole ring. The unfavorable product experiences delocalization that should in theory greatly stabilize the energy of this molecule; instead, the out of plane orientation of the indole provides poor overlap of the p-orbitals and thus less interaction between both molecules. A likely cause for this poor overlap is the steric congestion as the indole approaches the carbocation center causing sterics to dominate this reaction over the stabilization effect of delocalization. Further scrutiny reveals that nucleophilic attack at the α' position of the silyloxyallyl cation experiences little steric congestion and thus maximized overlap, the assumed root cause of the relatively low energy of this transition state.

The ability to control the chemistries of this work has great implications in the development of natural product inspired molecules as these small organic molecules are commonly used as pharmaceuticals.[7] The expansion of this work has proved difficult when applied to larger cyclic structures. Malone et al. have attempted the synthesis of six membered unsymmetrical silylenol ethers through oxyallyl cation intermediates.[8] Unlike the high yields obtained for the five membered rings reported in Chapter 4, trace amounts of the regioselective six membered rings were initially isolated due to challenges with the generation of the corresponding oxyallyl cation. The importance of expanding regioselective work of five membered rings lies in the utility of biologically active natural product structures containing six membered rings like that of hapalindole-type alkaloids.[9]

5.3. References

(1) Gorren, A. C. F.; Schrammel, A.; Schmidt, K.; Mayer, B. Decomposition ofS-Nitrosoglutathione in the Presence of Copper Ions and Glutathione. *Archives of Biochemistry and Biophysics* **1996**, *330*, 219-228.

(2) Hwang, S.; Meyerhoff, M. E. Polyurethane with Tethered Copper(II)-Cyclen Complex: Preparation, Characterization and Catalytic Generation of Nitric Oxide from S-Nitrosothiols. *Biomaterials* **2008**, *29*, 2443-2452.

(3) Wu, Y.; Meyerhoff, M. E. Nitric Oxide-Releasing/Generating Polymers for the Development of Implantable Chemical Sensors with Enhanced Biocompatibility. *Talanta* **2008**, *75*, 642-650.

(4) Li, T.; Taylor-Edinbyrd, K.; Kumar, R. A computational study of the effect of the metal organic framework environment on the release of chemically stored nitric oxide. *Physical Chemistry Chemical Physics* **2015**, *17*, 23403-23412.

(5) Harding, J. L.; Reynolds, M. M. Metal Organic Frameworks as Nitric Oxide Catalysts. *Journal of the American Chemical Society* **2012**, *134*, 3330-3333.

(6) Ayala, C. E.; Dange, N. S.; Fronczek, F. R.; Kartika, R. Brønsted Acid Catalyzed α′‐Functionalization of Silylenol Ethers with Indoles. *Angewandte Chemie* **2015**, *127*, 4724-4728.

(7) Melander, R. J.; Minvielle, M. J.; Melander, C. Controlling bacterial behavior with indole-containing natural products and derivatives. *Tetrahedron* **2014**, *70*, 6363-6372.

(8) Malone, J. A.; Cleveland, A. H.; Fronczek, F. R.; Kartika, R. Effects of Solvent and Residual Water on Enhancing the Reactivity of Six-Membered Silyloxyallyl Cations toward Nucleophilic Addition. *Organic Letters* **2016**, *18*, 4408-4411.

(9) Walton, K.; Berry, J. P. Indole Alkaloids of the Stigonematales (Cyanophyta): Chemical Diversity, Biosynthesis and Biological Activity. *Marine Drugs* **2016**, *14*, 73.

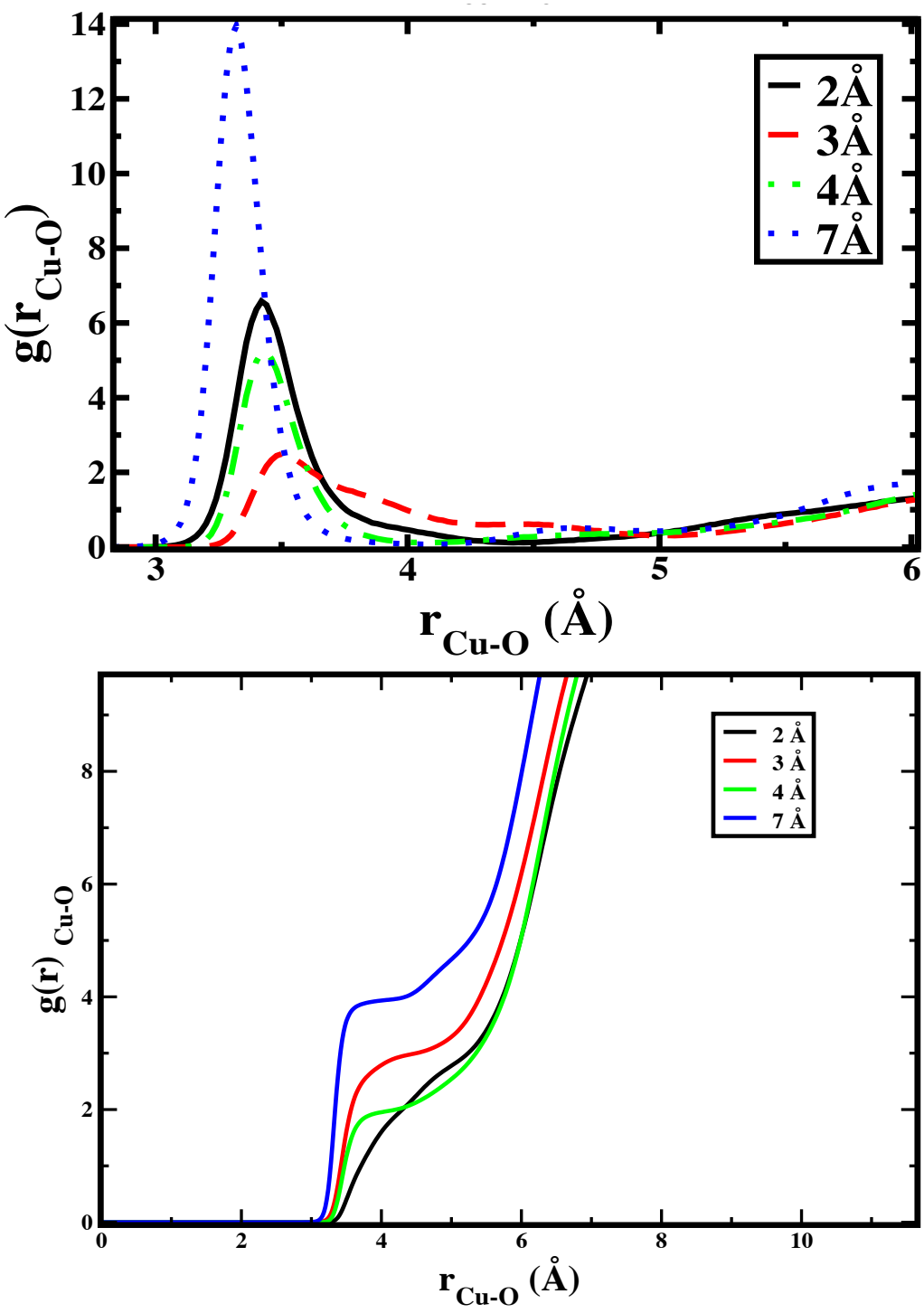

CPG-2RSNO (top) Radial Distribution Function (bottom) Integrated coordination numbers at various US-MD windows where r_{Cu-S} is constrained.

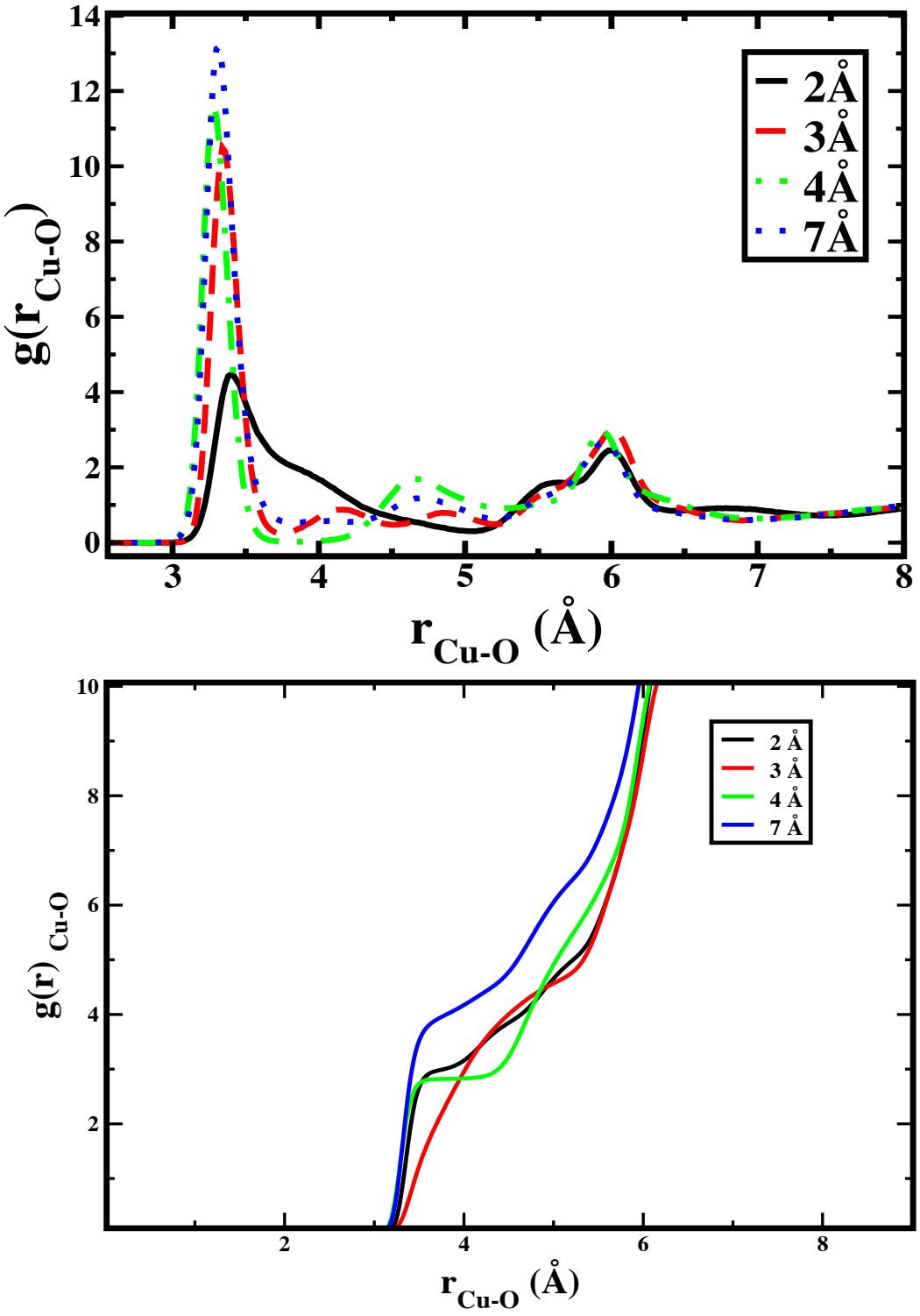

CPG-RSNO2. (top) Radial Distribution Function (bottom) Integrated coordination numbers at various US-MD windows where r_{Cu-S} is constrained.

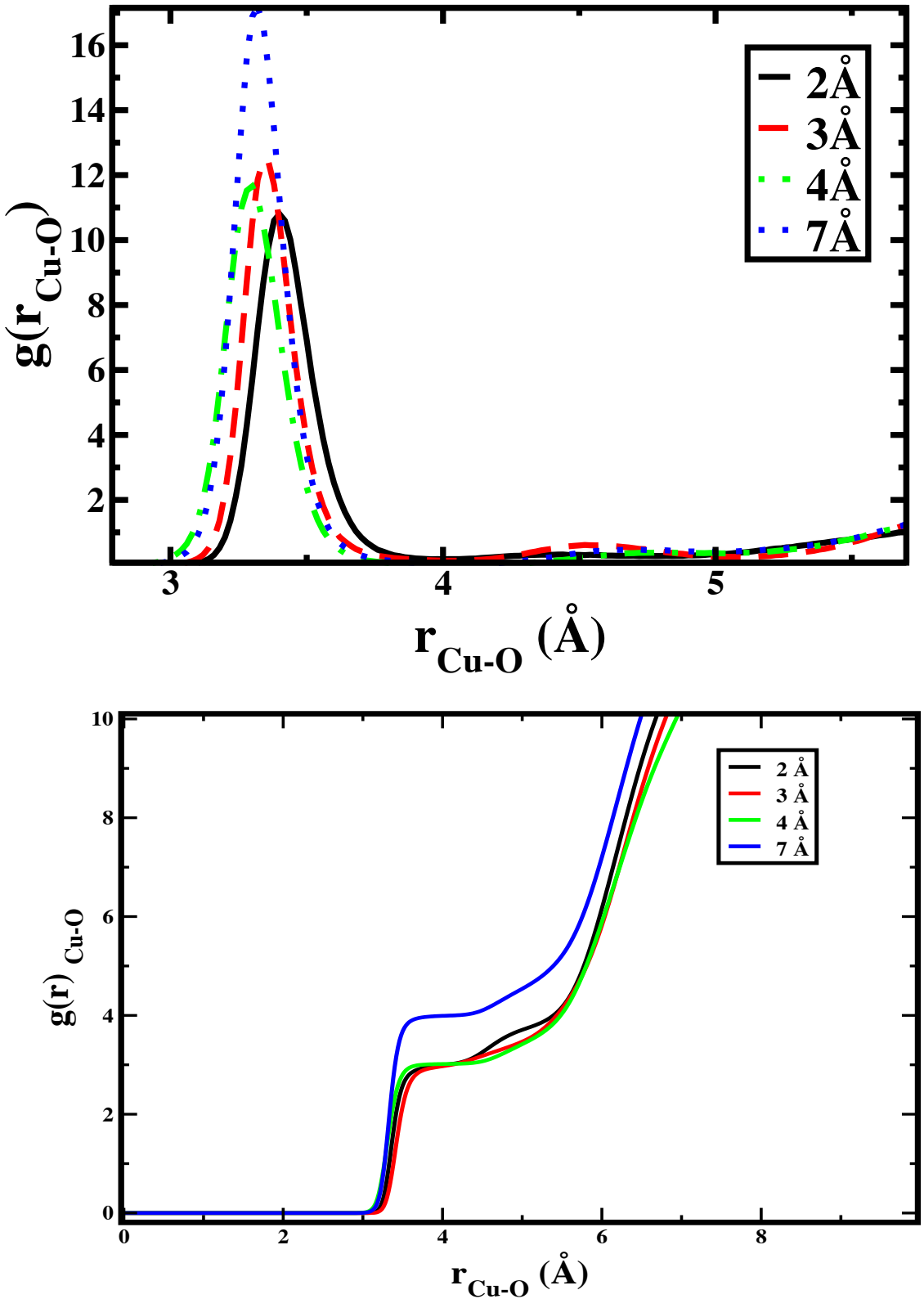

GPC-2RSNO. (top) Radial Distribution Function (bottom) Integrated coordination numbers at various US-MD windows where r_{Cu-S} is constrained.

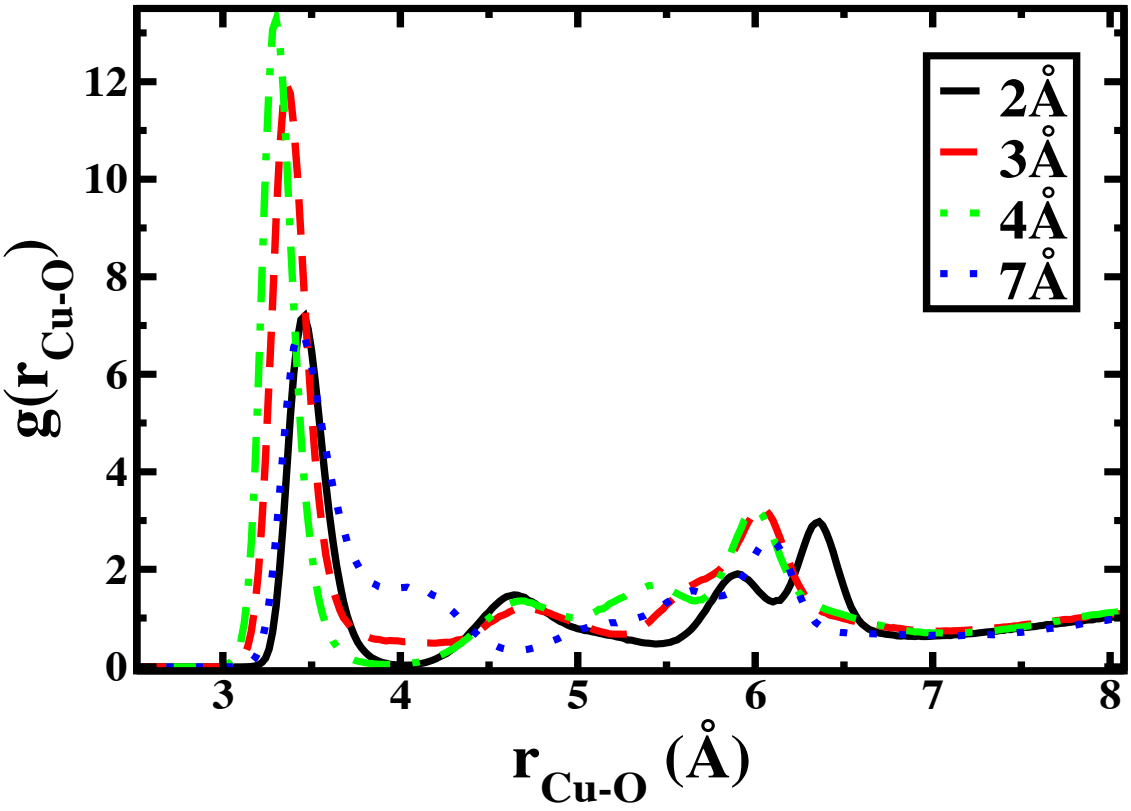

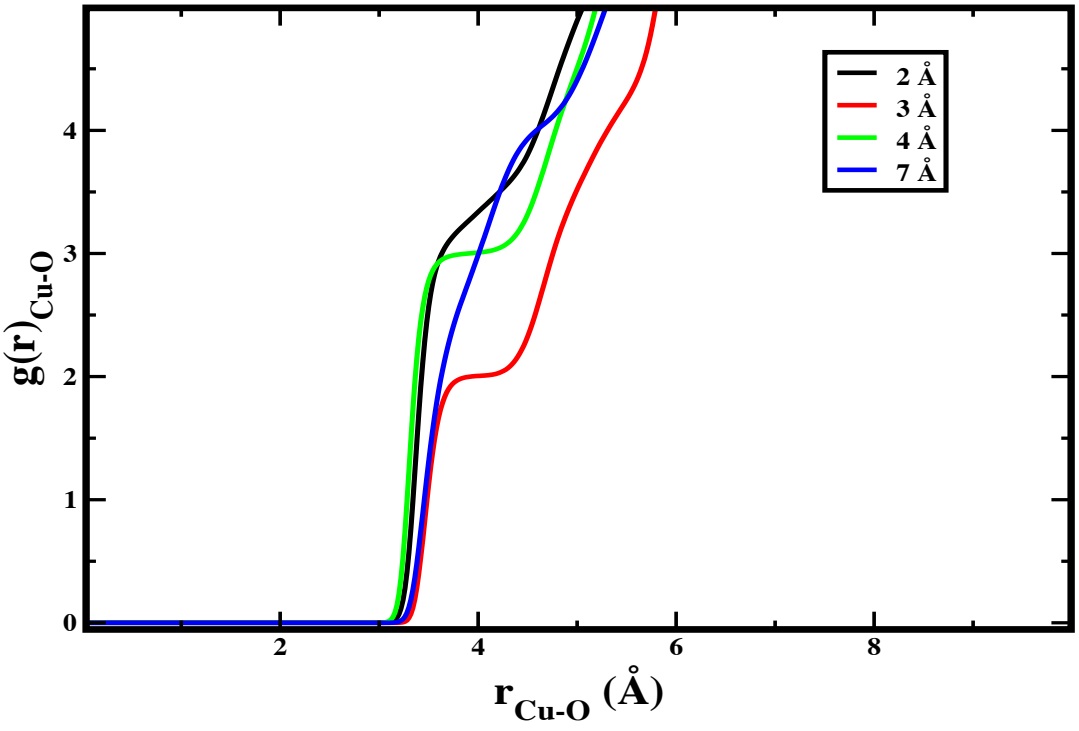

GPC-RSNO2. (top) Radial Distribution Function (bottom) Integrated coordination numbers at various US-MD windows where r_{Cu-S} is constrained.

VITA

Kiara Angelique Taylor-Edinbyrd, a native of Tulsa, Oklahoma, was born March 17th, 1989. She received her Bachelor's Degree in Chemistry from Texas Southern University (TSU). She had the pleasure of teaching high school level chemistry and physics at Arlington Heights High School in Fort Worth, TX prior to attending graduate school. Kiara was accepted into Louisiana State University (LSU) majoring in Physical Chemistry under research advisor Dr. Revati Kumar. During her studentship at LSU, Kiara was supported under two fellowships from the National Science Foundation including the Bridge to the Doctorate Program as well as the Louisiana Alliance for Simulation-Guided Materials Applications (LA-SIGMA). She anticipates graduating with her Ph.D. degree in December 2016.